# Cardiac T-Tubule Membranes

# Nanostructure and Remodeling Mechanisms in Disease

**Dissertation**

zur Erlangung des mathematisch-naturwissenschaftlichen Doktorgrades

"Doctor rerum naturalium"

der Georg-August-Universität Göttingen

im Promotionsprogramm Biologie

der Georg-August University School of Science (GAUSS)

vorgelegt von

**Eva Wagner**

aus Eschwege

Göttingen, 2012

*Für meine Eltern*

**Table of contents**

## Non-standard abbreviations

| | | |
|---|---|---|
| 4pMI | 4 weeks after (post-) MI | (see also "MI") |
| 4pTAC | 4 weeks after (post-) TAC | (see also "TAC") |
| 8pMI | 8 weeks after (post-) MI | (see also "MI") |
| 8pTAC | 8 weeks after (post-) TAC | (see also "TAC") |
| AP | action potential | |
| BCS | bovine calf serum | |
| $Ca_V1.2$ | voltage gated L-type $Ca^{2+}$ channel (also known as dihydropyridine receptor) | |
| Cav3 | caveolin-3 | |
| CICR | calcium induced calcium release | |
| E-C | excitation-contraction | |
| EF | ejection fraction | |
| EM | electron microscopy | |
| FWHM | full width at half maximum | |
| GAPDH | glyceraldehyde-3-phosphate dehydrogenase | |
| HF | heart failure | |
| HW/BW | heart weight to body weight ratio | |
| JPH2 | junctophilin-2 | |
| LAD | left anterior descending | |
| LSM | laser scanning microscope | |
| LVID,d | left ventricular inner diameter in diastole | |
| MI | myocardial infarction | |
| NA | numerical aperture | |
| NCX | sodium calcium exchanger | |
| PSF | point spread function | |
| PWTh,d | posterior wall thickness in diastole | |
| ROI | region of interest | |
| RyR2 | ryanodine receptor type 2 (cardiac isoform) | |
| SERCA | sarco/endoplasmic reticulum calcium ATPase | |
| SR | sarcoplasmic reticulum | |
| STED | stimulated emission depletion | |
| TAC | transverse aortic constriction | |
| TT | transverse tubule, T-tubule | |
| $Vol_d$ | heart volume in diastole | |
| $Vol_s$ | heart volume in systole | |

## Abstract

Transverse tubules (T-tubules, TTs) are continuous invaginations of the plasma membrane which form a complex network of excitable membranes inside mammalian ventricular cardiomyocytes. The TT network couples electrical with chemical signals in the relatively large cardiomyocytes and enables the synchronous rise of intracellular $Ca^{2+}$ concentrations in response to membrane depolarization during systole. It is assumed that the functional coupling of voltage-dependent $Ca^{2+}$ channels in the TT membranes and ryanodine receptor $Ca^{2+}$ release channels in the junctional sarcoplasmic reticulum is essential to assure $Ca^{2+}$ induced $Ca^{2+}$ release. Previous studies reported changes of the TT structure in cardiomyocytes from diseased hearts. However, the methods used to visualize TTs were either diffraction limited (confocal microscopy) or restricted to fixed samples (electron microscopy).

In this thesis, *Stimulated Emission Depletion* (STED) microscopy, a super-resolution technique, was used to quantitatively characterize TT membrane structures in living cardiomyocytes. Applying different image analysis strategies, the properties of individual TTs and the TT network in living healthy and diseased cardiomyocytes were quantified. Pathological TT changes were analyzed in two different mouse disease models, which were induced either by myocardial infarction (MI) or by transverse aortic constriction (TAC). Imaging and analysis of the TT nanostructure were complemented by functional measurements of intracellular $Ca^{2+}$ transients and by the analysis of proteins which might play a role in TT remodeling.

During heart failure (HF) development after MI, a progressive and heterogeneous enlargement of individual TT cross-sections was observed. In addition, length and complexity of the TT network progressively increased after MI. A significant increase of longitudinal TT elements was identified 4 weeks after MI representing an early time point of disease development. The observed TT remodeling was accompanied by differential expression changes of caveolin-3 and junctophilin-2. Furthermore, the differential spatial reorganization of TT elements correlated with a loss of intracellular $Ca^{2+}$ release synchrony. Increased TT dimensions and proliferative TT network remodeling were also observed during HF development in the TAC model. These data suggest that TT remodeling after TAC may occur over a shorter period of time than TT remodeling after MI.

This thesis introduces STED microscopy for imaging of intact TT membranes in living cardiomyocytes. Importantly, relatively early during HF development, individual TT elements and the cell-wide network properties are significantly altered through proliferative mechanisms. The data obtained here further suggest that TT remodeling during HF development might lead to excitation-contraction uncoupling, which can directly contribute to electrical and contractile dysfunction of diseased hearts.

# 1 Introduction

## 1.1 The mammalian heart

Every cell in the mammalian organism is supplied with oxygen and nutrients due to the specific pump function of the heart.

The mammalian heart is comprised of four chambers, two atria which collect blood and two ventricles which accelerate the blood into the pulmonary and the systemic circulation. Deoxygenated blood is collected by the right atrium. The right ventricle pumps it into the lungs, where it is oxygenated. Oxygenated blood from the lungs is then collected in the left atrium. From the left ventricle, oxygenated blood is pumped into the systemic circulation in order to meet the metabolic needs of all organs and their cell components.

Contractile heart muscle cells, termed cardiomyocytes, are essential to guarantee the blood flow and thereby continuous oxygen and nutrient supply throughout an organism's lifespan. In particular, ventricular cardiomyocytes ensure rapid and synchronous contraction of the ventricles. This is facilitated by their specialized membrane structure.

## 1.2 Transverse Tubules

The plasma membrane of mammalian ventricular cardiomyocytes (sarcolemma) is comprised of the surface sarcolemma and of continuous invaginations into the cell interior. These invaginations were named transverse tubules (TTs, T-tubules) because TTs were initially observed as transverse membrane elements occurring in regular intervals along the long cell axis [2-5]. In mammalian ventricular cardiomyocytes, TTs have first been described in 1957 by Lindner who applied electron microscopy (EM) [6]. Subsequent EM studies confirmed that TTs are indeed invaginations of the cardiomyocyte sarcolemma [7, 8]. Also in skeletal muscle cells, TTs were characterized as invaginations of the sarcolemma by EM. The continuity of the skeletal TT system with the extracellular space has been demonstrated by a ferritin diffusion method [9]. Numerous early EM studies of skeletal TTs from different species have been performed by Franzini-Armstrong and colleagues [10-15]. Subsequent EM studies showed that TTs form a complex membrane network inside cardiomyocytes [16].

The complex three-dimensional morphology of the TT system in living rat ventricular cardiomyocytes was revealed by Soeller and Cannell applying an extracellular dye solution together with two-photon microscopy [1]. They described the TT system as a "sarcolemmal Z rete", a network with regularly

spaced transverse elements connected through longitudinal elements. Figure 1.1 shows a three-dimensional TT network reconstruction from a z-stack of two-photon images. The average TT diameter in rat cardiomyocytes was determined as 255 nm based on deconvolved two-photon images [1].
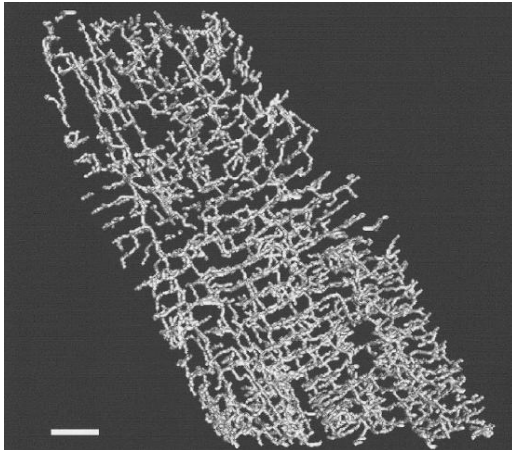


**Figure 1.1 Three-dimensional TT network in a rat ventricular cardiomyocyte.** Reconstruction of a z-stack imaged with a two-photon microscope. The TT system was visualized by extracellular application of a dextran-linked fluorescein solution. Scale bar: 5 μm. From Soeller and Cannell (1999) [1].

TTs provide a close proximity between the electrically excitable cell membrane and specialized terminals of the sarcoplasmic reticulum (SR), the main intracellular $Ca^{2+}$ store. TTs rapidly propagate depolarizing action potentials (APs) inside cardiomyocytes [17, 18] and thereby facilitate a synchronous contraction of the cell through a process known as excitation-contraction (E-C) coupling (see 1.3).

TTs contain all major membrane ion transport proteins in the heart (reviewed in [19]). Particularly the key proteins involved in E-C coupling occur predominantly at TTs. The density of voltage-gated L-type $Ca^{2+}$ channels ($Ca_V1.2s$, also known as dihydropyridine receptors), which enable $Ca^{2+}$ influx into the cell, is actually higher in TTs than in the surface sarcolemma [20, 21]. The $Na^{2+}/Ca^{2+}$ exchanger (NCX), which facilitates relaxation through extrusion of $Ca^{2+}$ to the extracellular site, is also more abundant in TTs than in the surface sarcolemma [22].

The regular distance between the transverse TT elements in muscle cells is specified by their sarcomeric structure. Early EM studies of cardiac muscle showed that TTs are found at the Z-line, the end of each sarcomere and therefore, they occur at intervals of approximately 2 μm along the longitudinal axis of a ventricular myocyte [7, 23].

## 1.3 The role of TTs in excitation-contraction coupling

Every heartbeat is initiated by tissue wide AP propagation. APs are conducted from the sinoatrial node over the atrioventricular node to the ventricular myocardium where contraction of the ventricles is triggered [24]. The physiological process of converting an electrical stimulus to a chemical signal and ultimately to a mechanical response has been defined as excitation-contraction (E-C) coupling [25].

Figure 1.2 shows a simplified scheme of cardiac E-C coupling. During an incoming cardiac AP, $Ca^{2+}$ enters the cell through the depolarization-activated L-type $Ca^{2+}$ channels $Ca_V1.2$. $Ca_V1.2$ is located in the sarcolemma, primarily at junctions between sarcolemma and SR. On the SR-side of these junctions, SR $Ca^{2+}$ release channels (ryanodine receptors type 2, RyR2s) are found [26, 27]. Upon entry of $Ca^{2+}$ through $Ca_V1.2$, RyR2s open and release $Ca^{2+}$ from the SR into the cytosol. This process is known as "$Ca^{2+}$ induced $Ca^{2+}$ release" (CICR) [28, 29]. The rise of intracellular $Ca^{2+}$, the systolic $Ca^{2+}$ transient, then activates the contractile proteins [30]. Cardiac troponin C acts as the sensor which confers $Ca^{2+}$ sensitivity to muscle contraction [31, 32]. Relaxation in diastole is caused by removal of $Ca^{2+}$ from the cytosol. The two main ion transporters that remove $Ca^{2+}$ from the cytosol are the SR $Ca^{2+}$ ATPase (SERCA) and the $Na^{2+}/Ca^{2+}$ exchanger (NCX) [30]. While SERCA pumps $Ca^{2+}$ back into the SR, NCX is predominantly located in the TT membrane and exchanges intracellular $Ca^{2+}$ against extracellular $Na^{2+}$ in its "forward" mode (3 $Na^+$ in, 1 $Ca^{2+}$ out) [33].
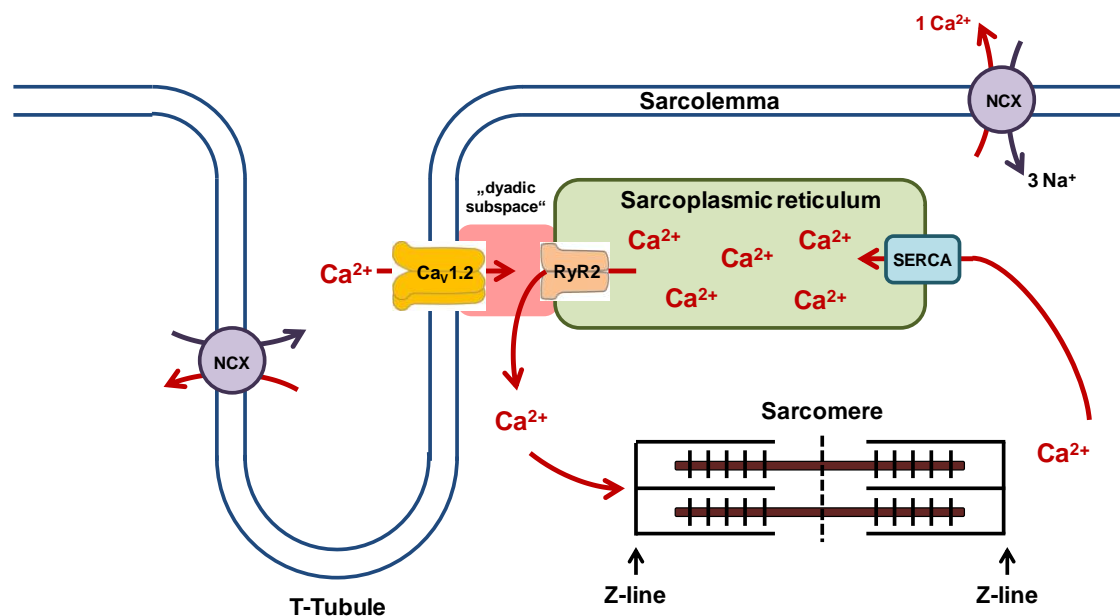


**Figure 1.2 Cardiac E-C coupling.** Upon depolarization of the membrane due to an incoming action potential (AP), $Ca^{2+}$ enters the cell through voltage-dependent L-type $Ca^{2+}$ channels ($Ca_V1.2$). $Ca^{2+}$ influx leads to the opening of ryanodine receptors type 2 (RyR2s) which release a large amount of $Ca^{2+}$ from the sarcoplasmic reticulum, a mechanism called "calcium induced calcium release" (CICR). Intracellular $Ca^{2+}$ binds to the myofilaments through troponin C, which activates contraction during systole. In diastole $Ca^{2+}$ is removed from the cytosol mainly by the SR $Ca^{2+}$ ATPase (SERCA) and the $Na^{2+}/Ca^{2+}$ exchanger (NCX) in its "forward" mode.

The regular TT spacing is thought to permit the large mammalian ventricular cardiomyocytes to nearly synchronously trigger the release of $Ca^{2+}$ from the SR in response to depolarization [19]. Accordingly, TTs are an important determinant of cardiac cell function, especially as the main site of E-C coupling, ensuring spatially and temporally synchronous $Ca^{2+}$ release throughout the cell [20]. In addition, the rapid and synchronous extrusion of $Ca^{2+}$ through NCX might be facilitated by TTs, which exhibit an approximately threefold higher NCX density than the surface sarcolemma [22].

## 1.4 Nanodomains in the heart: Couplons and calcium release units

### 1.4.1 Composition of couplons and calcium release units

E-C coupling in mammalian ventricular cardiomyocytes depends on the local subcellular signaling between $Ca_V1.2$ and RyR2 [19]. The functional grouping of RyR2 and $Ca_V1.2$ (and other junctional SR proteins) which may act in concert during E-C coupling is referred to as "couplon" [34]. The ratio of $Ca_V1.2s$ to RyR2s in a couplon is species dependent. For the cardiac dyad in rat for example, it is approximately one $Ca_V1.2$ per seven RyR2s [35].

The junctional gap between the SR and the plasma membrane in a couplon, termed subspace (the dyadic subspace is illustrated in Figure 1.2), measures approximately 12 nm, which classifies the couplon as a $Ca^{2+}$ nanodomain [36, 37]. Peter Jonas defines $Ca^{2+}$ nanodomains as domains of elevated $Ca^{2+}$ concentration that extend over less than 100 nm [38].

A calcium release unit (CRU) refers to a cluster of $Ca^{2+}$ release channels such as RyR2s [39]. Functionally, a CRU includes the $Ca^{2+}$ release channels, the SR cistern on which the channels reside and associated regulatory proteins [36].

It is known that cardiac myocytes contain three categories of CRUs, all bearing clusters of RyR2, the cardiac RyR isoform. These CRUs form either (1) peripheral couplings which are constituted of an association of the junctional SR (jSR) with the surface sarcolemma, (2) dyads, which are associations between the jSR and TT membranes or (3) they are located at internal extended junctional SR (EjSR, also termed corbular SR), which is not associated with the surface sarcolemma or with TTs [36, 40].

### 1.4.2 $Ca^{2+}$ sparks

The local event of $Ca^{2+}$ release from a single CRU is termed "$Ca^{2+}$ spark" [39, 41]. $Ca^{2+}$ sparks can be visualized by confocal microscopy applying fluorescent $Ca^{2+}$ indicators [42]. In confocal images,

typical $Ca^{2+}$ sparks result in a bright and short fluorescent signal corresponding to a transient (~30 ms) and local (~2 μm) elevation of $Ca^{2+}$ that reflects the activation of an estimated group of 10 or more RyR2s [41, 43]. $Ca^{2+}$ sparks constitute the elementary events of $Ca^{2+}$ release which control cardiac E-C coupling. Stochastic summation of $Ca^{2+}$ sparks produces a whole cell $Ca^{2+}$ transient, the global intracellular rise of the $Ca^{2+}$ concentration [39, 44, 45].

In summary, efficient coupling of membrane depolarization to SR $Ca^{2+}$ release requires precise spatial arrangements of RyR2s and $Ca_V1.2s$ and associated proteins. Therefore, disruption of CRUs, for example through reorganization of TT membranes, might lead to a loss of E-C coupling gain, which is defined as the efficacy of the $Ca^{2+}$ influx to activate SR $Ca^{2+}$ release [46].

## 1.5 TTs in atrial cardiomyocytes

It is well accepted that the TT system in ventricular cardiomyocytes ensures a spatially and temporally homogenous $Ca^{2+}$ release throughout the large cell volume. In contrast, atrial cardiomyocytes exhibit a different, less pronounced TT system [47, 48]. Thus, coupling between $Ca_V1.2$ and RyR2 occurs mainly at the cell periphery through peripheral couplings. Nevertheless, similar to ventricular cardiomyocytes, RyR2s in atrial cardiomyocytes are uniformly distributed along Z-lines [27, 49]. Accordingly, atrial cardiomyocytes exhibit a different, less homogenous form of $Ca^{2+}$ release than ventricular cardiomyocytes. During electrical stimulation, $Ca^{2+}$ release starts at focal regions at the cell periphery and spreads towards the center of the cell [49, 50]. This atrial $Ca^{2+}$ signaling occurs through propagated CICR due to $Ca^{2+}$ diffusion between adjacent RyR2 clusters [51].

It has been shown that a high proportion of adult mammalian atrial cardiomyocytes (> 50 % in rat [52]) possess a rudimentary TT system. In particular, atrial cardiomyocytes with large diameters and cells from the left atria, which generate higher pressures, exhibited TTs. These atrial TTs seem to influence $Ca^{2+}$ transients and their presence might also lead to a more rapid and coordinated contraction [52, 53]. Although TTs may have an effect on $Ca^{2+}$ transient generation in atrial cardiomyocytes, detubulation does not affect $Ca^{2+}$ signaling as dramatically as detubulation in ventricular cardiomyocytes [24].

In summary, TTs are present but less abundant in atrial cardiomyocytes than in the larger ventricular cardiomyocytes. TTs might play a role in atrial $Ca^{2+}$ transient generation, but their role is currently little understood.

**1.6 Cardiomyocytes without TTs**

TTs are present in ventricular cardiomyocytes of all mammalian species so far investigated [20]. Other species like birds [54], reptiles [55], amphibians [55] and fish [56] [57] [58] lack TTs, indicating that the presence of TTs in ventricles first appeared in mammals.

Furthermore, there is evidence that TT density is related to cell size. Additionally, there seems to be a correlation with species. The mouse heart for example with a heart rate of 600 – 800 beats/min has a higher TT density than the pig heart, which beats less than 100 times per minute [59, 60]. These correlations suggest that TTs are more abundant in hearts which depend on faster $Ca^{2+}$ cycling rates.

A current study extended the investigation of CRUs in birds (finch and chicken) and reptiles (lizard) [61]. This study confirmed that ventricular cardiomyocytes in the three investigated species do not contain TTs. While CRUs in the form of peripheral couplings were present in all species, only bird cardiomyocytes also exhibited corbular SR, which contains a large number of RyR2s which are not associated with the sarcolemma. Lizard compensates for the lack of TTs and internal CRUs by small diameters of its ventricular cardiomyocytes. In chicken and finch cardiomyocytes, the distance between internal CRUs seems to correlate with cell size and heart rate. The structure of the relatively large and rapidly beating finch cardiomyocytes (500 beats/min, diameter 6.9 µm; lizard: 140 beats/min, diameter 2.7 µm; chicken: 275 beats/min, diameter 4.6 µm) seems to be optimized to ensure an effective spread of $Ca^{2+}$ throughout the cell. Peripheral couplings that are responsible for the initial $Ca^{2+}$ release are strictly positioned at Z-lines. Corbular SR elements are also exclusively distributed along Z-lines with close proximity to allow an effective activation through propagated CICR. Less sophisticated conditions are found in the smaller and less rapidly beating chicken cardiomyocytes. Corbular SR elements are more widely spaced which reduces the probability of an effective $Ca^{2+}$ signal transmission [62] and peripheral couplings are not closely aligned with the corbular SR [61].

From this it follows that there are ventricular cardiomyocytes without TTs which ensure contraction through propagated CICR. Nevertheless, TTs seem to be essential to enable synchronous $Ca^{2+}$ release and rapid contraction in the large mammalian ventricular cardiomyocytes, particularly in species which depend on fast $Ca^{2+}$ cycling rates.

**1.7 TT biogenesis**

In the majority of mammalian species, TTs are absent in the embryonic and to some degree also in the early neonatal heart where they mature progressively after birth [63, 64]. The exact mechanism

of TT biogenesis is still unknown. However, it has been shown that TT formation occurs inward driven through invaginations of the surface sarcolemma and by intracellular addition of membrane lipids and specific proteins [65].

Several proteins have been associated with TT biogenesis. Among these, amphiphysin-2, caveolin-3 (Cav3) and junctophilin-2 (JPH2) seem to play a fundamental role in cardiac TT formation and organization [59, 66].

Amphiphysin-2 has primarily been investigated in skeletal muscle. There it is specifically localized to TTs [67, 68]. It has been shown that amphiphysin-2 knockout in drosophila leads to a severely disorganized TT system [68]. Misregulated alternative splicing of BIN1, the gene encoding amphiphysin-2, also leads to TT alterations in skeletal muscle and to muscle weakness in humans and mice [69]. Additionally it has been shown that expression of amphiphysin-2 in non-muscle cells, such as Chinese hamster ovary (CHO) cells, leads to TT formation [66]. Muller *et al.* defined BIN1 to play a critical role in cardiac muscle development. While targeted disruption of BIN1 in mice resulted in perinatal lethality, severe cardiomyopathies (markedly increased ventricular wall thickness resulting in occlusion of both ventricles) were observed in BIN1$^{-/-}$ embryos [70].

In 1968 is has been suggested for the first time that TTs might be generated through repeated caveolae formation [71]. Caveolae are flask-shaped invaginations of the plasma membrane with dimensions of 50 to 100 nm [72]. They are classified as lipid rafts, structures enriched in a variety of signaling molecules, which serve as platforms to organize signal transduction [73]. Caveolin proteins are the structural components of caveolae and moreover serve as scaffolding proteins. Cav3 is the muscle specific caveolin isoform [74]. Cav3 associates with developing TTs during differentiation of primary cultured muscle (C2C12) cells and of mouse skeletal muscle in vivo and is therefore thought to play a role in the early development of the TT system in skeletal muscle [75]. In skeletal muscle, knockout of Cav3 leads to disruption of the TT system, characterized by abnormally dilated and longitudinally oriented TTs [76].

Junctophilin proteins are membrane binding proteins which are believed to bridge the physical gap between the plasma membrane and the terminal SR. JPH2 is the major junctophilin isoform in the heart [77], where it promotes the formation of local junctions between SR and TTs [78]. While TTs are absent in neonatal cardiomyocytes, RyR2s are already positioned along the Z-line very early in development [64, 79]. Ziman *et al.* showed that during development, JPH2 colocalizes with Cav3 at the developing TTs. Not until JPH2 also colocalized with RyR2s, E-C coupling efficiency increased dramatically [64]. This finding provided further evidence for the involvement of JPH2 in the functional maturation of couplons. Moreover, it has been shown that cardiac-specific JPH2

knockdown in adult mice leads to a reduced number of junctional membrane complexes and an increased variability in the plasma membrane-SR distance, which results in a loss of the physiological E-C coupling gain [80] (for the definition of E-C coupling gain please refer to chapter 1.4.2).

## 1.8 Heart Failure

In 2010, cardiovascular diseases were the most frequent cause of death in Germany (353,000, Statistisches Bundesamt, https://www.destatis.de/). According to the International Statistical Classification of Diseases and Related Health Problems (10$^{th}$ revision, ICD-10), the most frequent total causes of death in 2010 were chronic ischaemic heart disease (8.5 %), followed by acute myocardial infarction (6.5 %) and heart failure (5.6 %).

Heart failure (HF) is a progressive and chronic disease, which is characterized by the inability of the diseased heart to meet the metabolic demands of organs and cells throughout the organism [81]. HF is the final common pathway of a variety of initial diseases including acute myocardial infarction (MI) or ischaemic heart disease. Hypertension is another very common risk factor for HF [82].

Depressed cardiac contractility is at least in part due to defective cardiomyocyte $Ca^{2+}$ handling [81, 83]. In failing cardiomyocytes, systolic SR $Ca^{2+}$ release is decreased due to a lower SR $Ca^{2+}$ content [84]. Additionally, the ability to trigger CICR, the E-C coupling gain, is reduced in failing cardiomyocytes, which could be explained by a change in the relation between RyR2s and $Ca_V1.2s$ [85]. An increasing number of studies indicate that impaired $Ca^{2+}$ signaling might at least in part result from alterations of the TT system.

## 1.9 TTs in heart failure

TT changes have been demonstrated both in samples from failing human hearts and in animal models of HF. But so far, depending on the model and the method used, the results are very divergent. The two main concepts for TT changes described in HF are (1) a reduced TT density ("loss of TTs") and (2) a disorganization of the TT network.

### 1.9.1 Reduced TT density in failing cardiomyocytes

Applying confocal microscopy, initial studies found a reduced density of TTs in failing cardiomyocytes that had been stained with the membrane dye di-8-ANEPPS [86, 87]. Subsequently, Heinzel *et al.*

investigated a post-MI pig model and suggested that the observed reduced TT density was associated with a reduced synchrony of $Ca^{2+}$ release and less efficient E-C coupling [88]. Indeed, studies in failing mouse and human cardiomyocytes by Louch *et al.* supported the observation that delayed $Ca^{2+}$ release occurs close to regions with disrupted TT structures [89, 90].

Lyon *et al.* (2009) confirmed a "loss of TTs" in failing human and rat cardiomyocytes [91]. Confocal microscopy of stained TT membranes was complemented by scanning ion conductance microscopy (SICM), a method that produces a topographic representation of the cell surface. SICM revealed a loss of TT openings at the surface in addition to the decreased TT density inside failing ventricular cardiomyocytes [91].

Again, Kemi *et al.* (2011) found a significantly decreased TT density in rats with mild cardiac pathological remodeling which were artificially selected and bred for low fitness as well as in a model of severe cardiac remodeling after MI. Interestingly, exercise induced physiologic cardiac hypertrophy in healthy rats did not lead to detectable changes in TT density [92]. As for the previously described studies, TT density was determined in confocal images of di-8-ANEPPS stained cardiomyocytes.

A possible causal role of TT loss in reduced E-C coupling gain and reduced contractility in HF is supported by experiments where TTs were artificially disrupted. Detubulation, either by prolonged cell culture or osmotic shock, led to qualitative changes in $Ca^{2+}$ handling which to some degree resemble the changes observed in HF [93, 94].

**1.9.2 Disorganization of the TT network in failing cardiomyocytes**

Applying confocal microscopy to fixed heart tissue sections from patients with tachycardia induced HF, Cannell *et al.* observed a deranged TT network structure [95]. In a non-quantitative approach, they compared failing with healthy control samples. Based on selected images, Cannell *et al.* described that TTs in failing cardiomyocytes were preferentially oriented in the longitudinal direction. Additionally, they observed dilated and bifurcated TT elements in failing cardiomyocytes. Using a computational model of $Ca_V1.2$ gating (Monte-Carlo model with a Markov gating scheme, for detailed description refer to [95]), Cannell *et al.* showed that alterations of the TT system leading to a small increase in the mean $Ca_V1.2$-RyR2 distance might already result in a marked decrease of E-C coupling gain [95].

Song *et al.* described a disorganization of the TT network in 19 week old spontaneously hypertensive rats (SHRs) that had developed HF [96]. Confocal images of failing cardiomyocytes exhibited a high

degree of spatially dispersed TTs which were not well aligned with Z-lines. The spatially remodeled TTs left behind RyR2 channels which were functionally less coupled to $Ca_V1.2$s and were therefore termed "orphaned RyRs". Song *et al.* concluded that increased spatial dispersion of TTs and orphaned RyR2s might lead to a HF-associated loss of local E-C coupling control and intracellular $Ca^{2+}$ instability at CRUs [96].

Wei *et al.* investigated TT network remodeling in a rat model of increased pressure overload due to transverse aortic constriction (TAC). To analyze the regular alignment of TTs with Z-line striations, Wei *et al.* used the so called TT power which is determined by Fourier transformation of confocal images and analysis of the resulting power spectra as described previously [96]. Disease groups were classified based on heart function (ejection fraction). The TT power was decreased in the disease groups and correlated with disease severity. The decrease of TT power was accompanied by a reduction of JPH2 expression [97].

## 1.10 Limitations of previous TT studies

As mentioned in section 1.2, Soeller and Cannell provided early insight into the network morphology of TTs in living rat cardiomyocytes [1]. Using two-photon microscopy and image reconstruction, they visualized the three-dimensional organization of the TT membrane system. The great advantage of two-photon or confocal microscopy is that light microscopy allows the investigation of structures in living cells. Even thick samples can be imaged non-invasively and in three dimensions.

However, the resolution of light microscopes is significantly limited due to the diffraction of light (for detailed explanation see 1.11). For the imaging of di-8-ANEPPS stained membranes (using a 1.4 NA objective), a light microscope provides a resolution not better than approximately 230 nm. Therefore, structures which are smaller than 230 nm will necessarily appear blurred both in confocal and two-photon images. Soeller and Cannell calculated the average diameter of TTs in rat ventricular cardiomyocytes as 255 nm based on deconvolved images obtained with a two-photon microscope that yielded a lateral resolution of 400 nm [1]. Depending on the species and the method used for TT quantification, estimated average TT diameters vary between 100 and 300 nm [17]. This implies that conventional light microscopy is not suitable to investigate morphological details of TTs since in most cases they are smaller than the attainable resolution. Furthermore, associated nanodomains like caveolae or small changes that might occur during HF development are most likely not visualized if conventional light microscopy is applied for quantitative evaluation.

In comparison to conventional light microscopy, electron microscopy (EM) yields nanometric resolution. Particularly, the EM studies of Franzini-Armstrong and colleagues resulted in detailed descriptions of CRUs and couplons in cardiac as well as in skeletal muscle [36, 98]. But in contrast to light microscopy techniques, EM cannot be applied to living samples and is typically restricted to single imaging planes. Moreover, sample preparation for EM requires invasive histochemical protocols including fixation, staining and dehydration as discussed by Soeller and Cannell [1]. Furthermore, slicing of delicate samples might lead to problems like knife artifacts, uneven thickness or folded sections [99].

Alternatively, scanning ion conductance microscopy (SICM), as already mentioned in 1.9.1, is a non-optical method that produces a topographic representation of the cell surface. While detailed imaging of the cardiomyocyte surface reveals features like TT openings, SICM is clearly limited and cannot be used to characterize TTs inside cardiomyocytes [91, 100].

Still light microscopy is the only method that allows the non-invasive imaging of µm-thick samples under physiological conditions and in three dimensions. In order to investigate TTs and potential morphological changes in living cardiomyocytes, it would be eligible to combine the advantages of light microscopy with nanometric resolution. This strategic combination has been accomplished with the development and application of STED microscopy.

## 1.11 STED microscopy

In microscopic studies, the resolution of the microscope directly determines how detailed the resulting images are and hence, how much information can be gained about the structure of interest.

Resolution has been defined as the minimal distance between two objects which a microscope can discriminate [101, 102]. The resolution of conventional light microscopes is limited due to the diffraction of light. According to Abbe (1873, [101]), the minimal resolvable distance between two objects is given by $d_{min} = \frac{\Lambda}{2\,n\,\sin\alpha}$ with $\Lambda$ denoting the wavelength of the emitted light, n the refractive index and $\alpha$ half the aperture angle of the objective lens ($n \cdot \sin\alpha$ denotes the numerical aperture, NA). In practical terms this means that confocal imaging of any membrane structure stained with di-8-ANEPPS (the dye used in this study with an emission maximum at 635 nm) using a 1.4 NA objective cannot be expected to provide a lateral resolution better than 230 nm.

In a conventional laser scanning confocal microscope, the sample is scanned point wise. Light is focused onto the sample and fluorescence is detected from the same spot. Due to diffraction,

focusing of light always results in a blurred spot. Accordingly, the lateral full width at half maximum (FWHM) of this focal spot is given by $\frac{\Lambda}{2\,n\,\sin\alpha}$ [103].

Not until the early 1990s, new concepts now referred to as *reversible saturable optical fluorescence transitions* (RESOLFT) were developed, which aimed to break the diffraction barrier. These concepts take advantage of the fact that certain fluorescent molecules can be reversibly switched between two optically distinguishable states. These can for example be the fluorescent ($S_1$) and the non-fluorescent ground-state ($S_0$) [102, 104].

One of the developed concepts is *Stimulated emission depletion* (STED) microscopy, first described in 1994 [105, 106]. The basic idea behind STED microscopy is to minimize the lateral size of the focal spot in a point-scanning system by switching off fluorescent molecules in its periphery. Switching off, which in physical terms corresponds to the transition from the fluorescent $S_1$ to the ground state $S_0$, is accomplished by stimulated emission. Stimulated emission has first been mentioned by Albert Einstein in 1917 [107]. It describes the phenomenon that an excited molecule can be forced back to its ground state through interaction with a photon, thereby emitting an additional photon of the same phase and frequency. In contrast to spontaneous emission, stimulated emission does not result in visible fluorescence. Figure 1.3 illustrates the different energy levels of a fluorophore and the different types of transitions involved in STED microscopy.
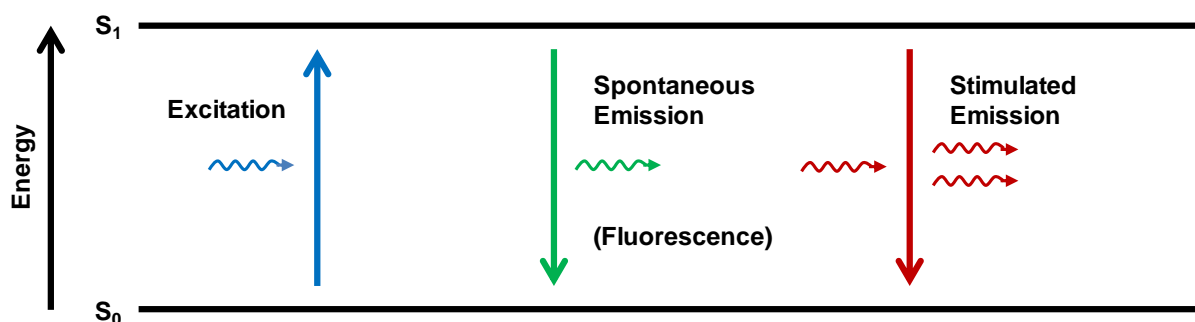


**Figure 1.3 Jablonski diagram representing the different energy levels and transitions involved in STED microscopy.** Fluorophores can be excited from their ground state $S_0$ to their fluorescent state $S_1$. Molecules can return to $S_0$ by spontaneous emission, thereby emitting visible fluorescence (green). Return to $S_0$ may also be enforced through stimulated emission. Stimulated emission does not result in visible fluorescence (red).

Spontaneous emission can be suppressed via stimulated emission by optically forcing the molecule to its ground state $S_0$ directly after excitation. To increase resolution in a STED microscope, the excitation focus is overlaid with a de-exciting (STED) laser beam of toroidal ("donut") shape. So the fluorophores in the periphery of the excitation focus are switched off by stimulated emission and

only molecules in the center stay fluorescent. With increasing intensity of the de-excitation beam, it becomes more likely that the excited $S_1$ state is depleted by stimulated emission. Saturated depletion by the de-exciting (STED) laser beam leads to an effective fluorescent spot with subdiffraction dimensions as illustrated in Figure 1.4 [105, 108, 109]. To stimulate emission, typically red light is used [110, 111]. Due to the high wavelength of red light, the STED laser does not excite the fluorophores and allows the spectral separation of spontaneous and stimulated emission.
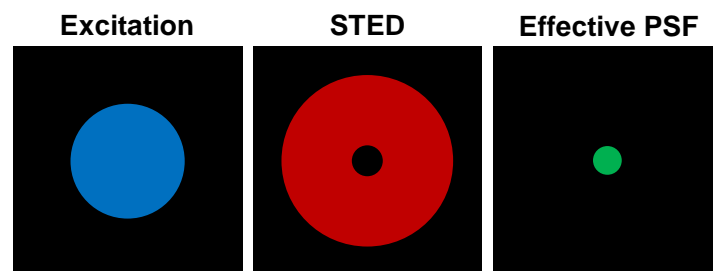


**Figure 1.4 Configuration of foci in a STED microscope.** Figure modified from Lauterbach, 2009 [112]. The excitation focus is overlayed with a de-excitation (STED) laser beam of toroidal shape. De-excitation probability increases with increasing power of the STED laser. This results in the small effective point spread function (PSF) of a STED microscope.

De-excitation of the fluorophores in the periphery of the excitation focus by stimulated emission in a STED microscope leads to increased resolution, which can be described by:

$$d = \frac{\Lambda}{2\,NA\,\sqrt{(1 + \frac{ISTED}{Isat})}}$$

With $\Lambda$ denoting the wavelength of the emitted light, NA the numerical aperture of the objective, $I_{STED}$ the intensity of the STED laser beam and $I_{sat}$ the saturation intensity at which half of the fluorophores are forced to their ground state [113].

In summary, STED microscopy combines a theoretically unlimited resolution with the advantages of conventional light microscopy. This allows the non-invasive imaging of living samples under physiological conditions and can be conducted in three dimensions even deep inside a specimen.

**1.12 Aim of this thesis**

The overall aim of this thesis was to quantitatively analyze the nanostructure of intact TT membranes in living healthy and diseased cardiomyocytes. The expectation was that a super-resolution technique like STED microscopy could reveal new insight about potential mechanisms during TT remodeling in disease. For this purpose, I established protocols for STED imaging of TTs in living cardiomyocytes and developed new strategies for quantitative image analysis to proof superiority to conventional imaging methods like confocal microscopy. These strategies were initially applied to determine the morphology of TTs in healthy cardiomyocytes. In order to quantitatively analyze TT changes particularly during the development of HF, two different disease models were investigated (myocardial infarction and transverse aortic constriction). To correlate the observed TT changes with $Ca^{2+}$ signaling, a combination of TT and $Ca^{2+}$ imaging was used. In addition, proteins that are potentially involved in TT biogenesis or directly associated with TTs were analyzed in diseased and healthy cardiomyocytes. Protein localization and expression levels were analyzed by immunofluorescence and Western blot respectively. Finally, TT membrane imaging by STED was extended towards three dimensions in order to gain further insight into the morphology, spatial distribution and reorganization of TTs in healthy and diseased cardiomyocytes.

## 2 Methods

Chemicals, drugs, dyes, antibodies as well as consumables, general equipment and the respective manufacturers are listed in the supplement (6.1 – 6.8). The software used for data acquisition, image analysis and processing with the according providers is also listed in the supplement (6.9).

### 2.1 Mouse disease models

All animal procedures were reviewed and approved by the institutional animal care and use committee at University Medical Center Göttingen and by the veterinarian state authority LAVES (Niedersächsisches Landesamt für Verbraucherschutz und Lebensmittelsicherheit) in compliance with the human care and use of laboratory animals.

In this study, two different mouse disease models were investigated. To examine the consequences of myocardial infarction (MI), the left anterior descending (LAD) coronary artery was proximally ligated. To generate pressure overload, transverse aortic constriction (TAC) was performed. For both interventions, 9 week old female C57Bl/6N mice (Charles River, Sulzfeld, Germany) were used. Pain management involved a predefined protocol including treatment with 1.33 mg/ml metamizol in the drinking water starting 3 days before the intervention. Before the surgical intervention and as needed, additionally buprenorphin (0.12 µg/mg body weight) was applied by subcutaneous injection.

### 2.1.1 Proximal LAD ligation to induce large myocardial infarction (MI)

A proximal LAD ligation was performed to induce a large MI following previously described protocols [114, 115]. Control mice underwent a Sham operation. During surgery, mice were anesthetized with 2 % isoflurane in $O_2$ ventilated with a tidal volume of 0.15 ml and a frequency of 150 strokes per min using a custom-made mouse tubus and a mouse respirator. A left lateral thoracotomy was performed. For MI, the LAD coronary artery was proximally ligated with a permanent 9-0 polyamide suture. The MI was directly confirmed by permanent distal tissue blanching and the approximate infarct size was estimated as percentage of the left ventricle. Infarct sizes averaged approximately 35 % of the left ventricle as previously confirmed by histology. For Sham operations, mice underwent the same procedure except that the LAD coronary artery was not ligated. Subsequently, the chest was closed with a 6-0 suture, the lungs were inflated and mice were closely monitored until spontaneous, regular breathing occurred. After surgery, the metamizol pain medication was

continued for 7 days or longer if necessary. During postoperative recovery, the health status and body weight of the operated mice were checked at least daily.

4 or 8 weeks after the MI operation, the hearts were used for isolation of ventricular cardiomyocytes. Before cardiomyocyte isolation, mice were phenotyped by echocardiography (see 2.1.3). To exclude variability in the mouse age, the Sham data presented here were all generated 8 weeks after the intervention.

### 2.1.2 Transverse aortic constriction (TAC) to generate pressure overload

To increase afterload, the transverse aorta was constricted by a minimally invasive surgery approach as described previously [116]. During surgery, mice were anesthetized with 1.5 % isoflurane in $O_2$. A horizontal incision at the jugulum was used to display the transverse aorta. A 27 gauge needle was tied against the aorta using a 5-0 non-absorbable suture. After removal of the 27 gauge needle, the skin was closed with a 6-0 suture and the mice were monitored until full recovery from anesthesia. Sham animals underwent the same procedure except for constriction of the transverse aorta. After surgery, the metamizol pain medication was continued for 7 days or longer if necessary. During postoperative recovery, the health status and body weight of the operated mice were checked at least daily.

4 or 8 weeks after the TAC operation, the hearts were used for isolation of ventricular cardiomyocytes. Before cardiomyocyte isolation, mice were phenotyped by echocardiography (see 2.1.3). To exclude variability in the mouse age, the Sham data presented here were all generated 8 weeks after the intervention.

### 2.1.3 Echocardiography of mouse hearts

Either 4 or 8 weeks after MI, TAC or the according Sham operations, mice were characterized by rodent echocardiography (Vevo 2100, VisualSonics) using a 30 Hz transducer (MS400 MicroScan™ transducer). For echocardiography, mice were anesthetized with 1.5 % isoflurane in $O_2$. Body temperature was kept at 37°C. Left ventricular dimensions and wall thicknesses were determined by parasternal long and short axis views. Ejection fraction (EF, in %) was calculated as $EF = (Vol_d - Vol_s) / Vol_d \cdot 100$ with $Vol_d$ = heart volume in diastole and $Vol_s$ = heart volume in systole. Heart volumes were calculated as $Vol_d = \frac{5}{6} \cdot Area_d \cdot L_d$ and $Vol_s = \frac{5}{6} \cdot Area_s \cdot L_s$ with Area denoting the area of the endocardium and L denoting the long heart axis in diastole and systole respectively.

The pressure gradient in TAC and the according Sham mice was measured by pulsed wave Doppler ultrasound of the transverse aorta at the site of constriction using a 20 Hz transducer (MS250 MicroScan™ transducer). Initially, the maximal blood flow velocity (in m/s) was determined as average of three independent values per mouse. The maximal velocity was then converted into the pressure gradient (in mmHg) by applying the "simplified Bernoulli equation" [117, 118]:

$$\text{gradient (mmHg)} = (\text{maximal velocity (m/s)})^2 \cdot 4$$

## 2.2 Isolation of ventricular cardiomyocytes

The protocol for isolation of adult ventricular cardiomyocytes was modified from O'Connell *et al.* [119]. Adult female C57Bl/6N mice (Charles River, Sulzfeld, Germany) were anesthetized with 3 % isoflurane in $O_2$ and sacrificed by cervical dislocation. Hearts were quickly extracted and the proximal aorta was immediately connected to a 21 gauge cannula. Using a modified Langendorff system [120] at a flow rate of 4 ml/min, hearts were perfused with $Ca^{2+}$ free perfusion buffer (formulation below) for 4 min at 37°C. Following confirmation of relaxation, perfusion was switched to digestion buffer containing 2 mg/ml collagenase type II (~300 units/mg) and 40 µM $CaCl_2$ for another 9 min at 37°C. Following perfusion, ventricles were manually dissected in digestion buffer. Scar tissue from post-MI hearts was carefully excised and discarded. Collagenase II digestion was stopped with perfusion buffer containing 10 % bovine calf serum (BCS) and 12.5 µM $CaCl_2$. Isolated ventricular cardiomyocytes were washed two times with the stopping buffer containing 10 % BCS and 12.5 µM $CaCl_2$. In order to wash the isolated cells, they were sedimented by gravity for 8 min at room temperature. The supernatant was discarded and the sedimented cells were again resuspended in stopping buffer. All experiments were conducted within 6 h after cardiomyocyte isolation and following quality assessment of the isolated cardiomyocytes (no membrane blebs, no aberrant contractions, regular striations).

**Perfusion buffer**

|                              | MW (g/mol) | Final concentration (mM) |
| ---------------------------- | ---------- | ------------------------ |
| NaCl                         | 58.44      | 120.4                    |
| KCl                          | 74.56      | 14.7                     |
| $KH_2PO_4$                   | 136.09     | 0.6                      |
| $Na_2HPO_4 \cdot 2\,H_2O$    | 177.99     | 0.6                      |
| $MgSO_4 \cdot 7\,H_2O$       | 246.48     | 1.2                      |
| HEPES                        | 238.31     | 10                       |
| $NaHCO_3$                    | 84.01      | 4.6                      |
| Taurin                       | 125.2      | 30                       |
| 2,3-Butanedione monoxime     | 101.1      | 10                       |
| Glucose                      | 180.16     | 5.5                      |
| pH 7.4 at 37°C               |            |                          |

## 2.3 Preparation of living cardiomyocytes for imaging

### 2.3.1 Membrane staining with di-8-ANEPPS

The plasma membrane (surface sarcolemma + TTs) of living isolated cardiomyocytes was stained with the styryl dye di-8-ANEPPS. Before staining of isolated cardiomyocytes, glass cover slips (Ø 42 mm) were placed into an imaging chamber and coated with laminin (2 mg/ml) diluted 1:10 in perfusion buffer. Freshly isolated ventricular cardiomyocytes were resuspended in $Ca^{2+}$ free perfusion buffer and sedimented for 8 min by gravity. The supernatant was discarded and the cells were resuspended in perfusion buffer containing 50 µM di-8-ANEPPS. In the dye-containing buffer, cardiomyocytes were plated on the laminin coated cover slips. After 10 min incubation in the dark at room temperature, cells were washed two times with perfusion buffer in order to remove unbound dye molecules. For microscopy, the imaging chamber was filled with freshly prepared perfusion buffer.

### 2.3.2 Preparation of cardiomyocytes for combined TT and $Ca^{2+}$ imaging

For combined imaging of TTs and $Ca^{2+}$ transients, the plasma membrane was stained with di-8-ANEPPS and cells were additionally loaded with the $Ca^{2+}$ indicator fluo-4/AM. Before staining, custom-made imaging chambers were coated with laminin (2 mg/ml) diluted 1:10 in physiological buffer (formulation below).

Since $Ca^{2+}$ imaging requires a physiological $Ca^{2+}$ containing buffer and cardiomyocytes are isolated under conditions with artificially low $Ca^{2+}$ concentrations, cell isolation was followed by a stepwise $Ca^{2+}$ introduction. For this purpose, cells were resuspended in perfusion buffer containing 10 % BCS and 100 µM $CaCl_2$ after the first washing step. Cells were sedimented by gravity for 8 min at room temperature, the supernatant was discarded and cells were resuspended in perfusion buffer containing 10 % BCS and 400 µM $CaCl_2$. After further 8 min, cells were washed in the last $Ca^{2+}$ introducing buffer containing 900 µM $CaCl_2$. Finally, cardiomyocytes were transferred into physiological buffer (formulation below) and again sedimented for 8 min by gravity before use.

In order to stain TTs and load isolated cardiomyocytes with the $Ca^{2+}$ indicator fluo-4/AM, the supernatant was discarded and cells were resuspended in physiological buffer containing 10 µM di-8-ANEPPS and 10 µM fluo-4/AM. In the dye-containing buffer, cells were plated on the laminin coated imaging chambers. After 15 min incubation in the dark at room temperature, the dye solution was replaced by physiological buffer containing only 10 µM fluo-4/AM. After further 15 min in the dark, cells were washed once with physiological buffer. For microscopy, the imaging chambers were filled with fresh physiological buffer.

**Physiological buffer for combined TT and $Ca^{2+}$ imaging**

|                              | MW (g/mol) | Final concentration (mM) |
|------------------------------|------------|--------------------------|
| NaCl                         | 58.44      | 140                      |
| KCl                          | 74.56      | 5.4                      |
| $Na_2HPO_4 \cdot 2\,H_2O$    | 177.99     | 0.33                     |
| $MgCl_2 \cdot 6\,H_2O$       | 203.3      | 1.2                      |
| HEPES                        | 238.31     | 10                       |
| Glucose                      | 180.16     | 10                       |
| $CaCl_2$                     | 110.98     | 1                        |
| pH 7.4 at 37°C               |            |                          |

**2.4 Preparation of fixed cardiomyocytes for imaging**

**2.4.1 Immunostains**

For immunofluorescence imaging, a fraction of cardiomyocytes was immediately fixed after isolation. For this purpose, glass coverslips (Ø 18 mm) were coated with laminin (2 mg/ml) diluted 1:10 in perfusion buffer (for formulation see 2.2). In perfusion buffer, cells were plated on the laminin coated coverslips for 30 min at room temperature. Afterwards, cardiomyocytes were fixed with 4 % paraformaldehyde (PFA) in phosphate buffered saline (PBS, pH 7.4, without $Ca^{2+}$ and $Mg^{2+}$) for 5 min at room temperature. After two PBS washing steps, cells were permeabilized with 0.2 % Triton X-100 and blocked with 10 % BCS in PBS. Overnight, cells were incubated with primary antibodies diluted in the permeabilizing and blocking buffer at 4°C (primary antibodies and dilutions used for immunostains are listed in Table 6.8.1, Supplement).

The next day, the cardiomyocytes were washed three times with the permeabilizing and blocking buffer and incubated for 90 min with the secondary antibodies diluted in the same buffer at room temperature and in the dark (secondary antibodies and dilutions used for immunostains are listed in Table 6.8.1, Supplement).

After three PBS washing steps, cells were embedded in mounting medium, cured overnight and imaged the next day.

**2.4.2 Preparation of cardiomyocytes for size determination**

For determination of cell sizes, a fraction of cardiomyocytes was immediately fixed after isolation. For this purpose, glass coverslips (Ø 18 mm) were coated with laminin (2 mg/ml) diluted 1:10 in perfusion buffer. In perfusion buffer, cells were plated for 30 min at room temperature. Afterwards, cardiomyocytes were fixed with 4 % PFA in PBS (pH 7.4, without $Ca^{2+}$ and $Mg^{2+}$) for 5 min at room temperature. After two PBS washing steps, the fixed cardiomyocytes were embedded in mounting medium, cured overnight and imaged the next day.

**2.5 Preparation of isolated cardiomyocytes for protein analysis**

To prepare freshly isolated ventricular cardiomyocytes for Western blot analysis, cells were resuspended in perfusion buffer and sedimented by gravity for 8 min at room temperature directly

after isolation. The supernatant was discarded, cells were immediately snap-frozen in liquid $N_2$ and stored at -80°C until further used for analysis.

## 2.6 Confocal microscopy

Confocal microscopy was used to image double stained cell samples[1]. Imaging of co-immunostains as well as combined TT and $Ca^{2+}$ imaging were performed with a LSM 710 confocal laser scanning microscope (Carl Zeiss, Jena, Germany) using a 63x 1.4 NA oil objective. The transmitted light mode of the LSM 710 was used to obtain images for the determination of cell sizes. Images were recorded with the appropriate software provided by the manufacturer (ZEN 2009) and saved as ".lsm" files. For further analysis ".lsm" images were converted into ".tif" images using ImageJ.

### 2.6.1 Confocal imaging of immunostains

AlexaFluor®514 was excited at 514 nm (2 % laser power) and detected at $520-620$ nm. Pinhole opening of 1 Airy unit resulted in an optical slice thickness of 800 nm.

AlexaFluor®633 was excited at 633 nm (2 % laser power) and detected at $640-740$ nm. Pinhole opening of 1 Airy unit resulted in an optical slice thickness of 1 µm.

The pixel size for imaging of (co-)immunostains was 80 nm x 80 nm.

### 2.6.2 Transmitted light imaging for determination of cell sizes

For determination of their size, cardiomyocytes were prepared as described in 2.4.2. Fixed cardiomyocytes were imaged by the transmitted light mode of the LSM 710 with a pixel size of 0.38 µm x 0.38 µm. Using ImageJ, the border of the isolated ventricular cardiomyocytes was marked manually in the transmitted light images. Area, length and width were then determined automatically by the program using the "*ROI manager*".

---

[1] At the time of this study, the STED setup used here was limited to single color imaging.

### 2.6.3 Combined confocal TT and Ca$^{2+}$ imaging

The imaging protocol for combined imaging of TTs and Ca$^{2+}$ transients was modified from Louch *et al.* [89]. Initially, a di-8-ANEPPS image was recorded with a pixel size of 80 nm x 80 nm. Subsequently, either a longitudinal line crossing transverse TT elements, or a transverse line crossing longitudinal elements was selected. Lines for either direction measured 20 µm (100 pixels, pixel size 0.2 µm). To record Ca$^{2+}$ transients along the selected lines, cells were field stimulated at 0.5 Hz (23 V, 3 ms duration) using a platinum electrode. Lines were imaged with the settings for fluo-4/AM every 1.53 ms (total: 6000 cycles). Afterwards, the same lines were imaged with the settings for di-8-ANEPPS in order to correlate TT signals with the previously recorded Ca$^{2+}$ signals during offline analysis.

Di-8-ANEPPS was excited at 458 nm (5 % laser power) and detected at 550 – 740 nm. Pinhole opening of 1 Airy unit resulted in an optical slice thickness of 900 nm.

Fluo-4/AM was excited at 488 nm (2 % laser power) and detected at 490 – 540 nm. Pinhole opening of 1 Airy unit resulted in an optical slice thickness of 700 nm.

### 2.7 STED microscopy

STED microscopy was used to examine the nanostructure of TTs in living cardiomyocytes.

The custom STED setup used here was built around an inverted microscope (Leica, Heidelberg, Germany). Excitation and de-excitation were performed with synchronized pulsed lasers, using the STED pulses to trigger the excitation laser. Di-8-ANEPPS stained cardiomyocytes were excited with a pulsed diode laser at a wavelength of 490 nm (3 µW for confocal images, 10 µW for STED images). De-excitation pulses at 750 nm (~180 mW) were delivered by a Ti:Sapphire laser operating at 80 MHz. Both laser beams were spatially filtered with separate single-mode fibers (SMF). A dichroic mirror (DM2) combined the excitation and de-excitation beams which were then focused through a 100x 1.4 NA oil objective. To generate the toroidal focus ("donut shape"), the de-excitation (STED) laser was passed through a vortex phase plate.

In the detection path, two dichroic mirrors (DM1, DM2) separated the fluorescence signal from the incoming laser beams. Fluorescence was then filtered by a 675 ± 30 nm bandpass and detected by an avalanche photodiode.

The images were recorded by resonant mirror scanning (16 kHz) along the first lateral axis and by piezo stage scanning along the second lateral axis. The pixel size was 20 nm x 20 nm and pixel dwell time was 20 µs.

A schematic of the STED setup is shown in Figure 2.1. The individual parts of the STED setup and the respective manufacturers are separately listed in Table 6.7 (Supplement).
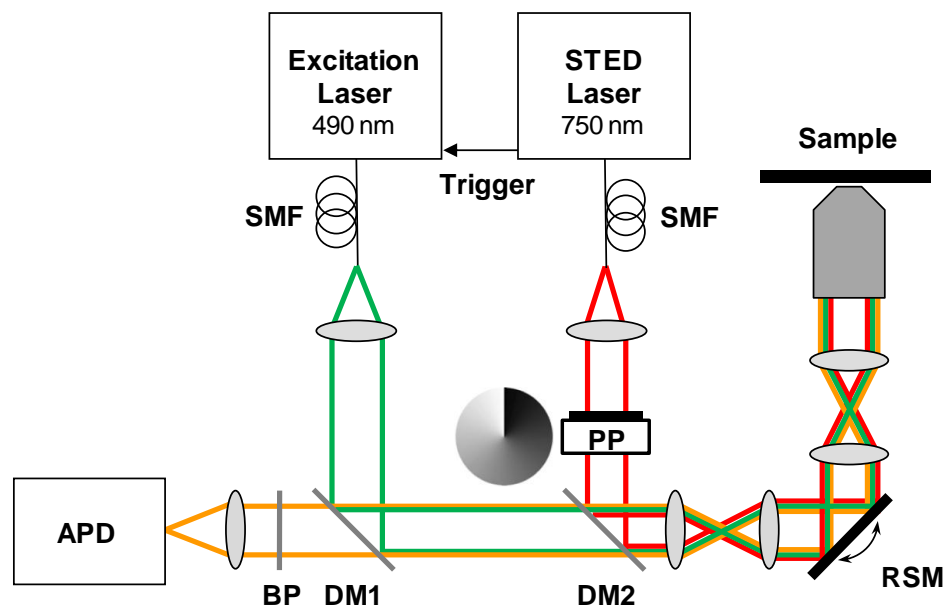


**Figure 2.1 The experimental STED microscopy setup.** Di-8-ANEPPS stained cardiomyocytes were excited at 490 nm. De-excitation (STED) was performed at 750 nm. For confocal imaging, only the excitation laser was used. For STED imaging, the excitation laser was triggered by the STED pulses. Green: excitation laser beam. Red: STED laser beam. Orange: resulting fluorescence signal. SMF: single-mode fiber, APD: avalanche photo diode, BP: band pass, DM: dichroic mirror, PP: phase plate, RSM: resonant scanning mirror

In order to document the resolution of the STED and the confocal mode and to exclude day-to-day variability, custom-made fluorescent 20 nm sized beads were imaged before measuring the actual samples. As shown in Figure 2.2, under the given conditions (excitation at 490 nm, STED at 750 nm), STED increased the average lateral resolution nearly fourfold (FWHM x: confocal 191 nm, STED 58 nm; FWHM y: confocal 203 nm, STED 52 nm). As expected, STED did not improve the axial resolution (FWHM z: confocal 455 nm, STED 479 nm).

**A**



**B**



**C**

| Confocal | | |
|---|---|---|
| | **FWHM (nm)** | **n** |
| x | 191 ± 11 | 10 |
| y | 203 ± 21 | 10 |
| z | 455 ± 51 | 10 |

| STED | | |
|---|---|---|
| | **FWHM (nm)** | **n** |
| x | 58 ± 8 | 25 |
| y | 52 ± 8 | 25 |
| z | 479 ± 112 | 20 |
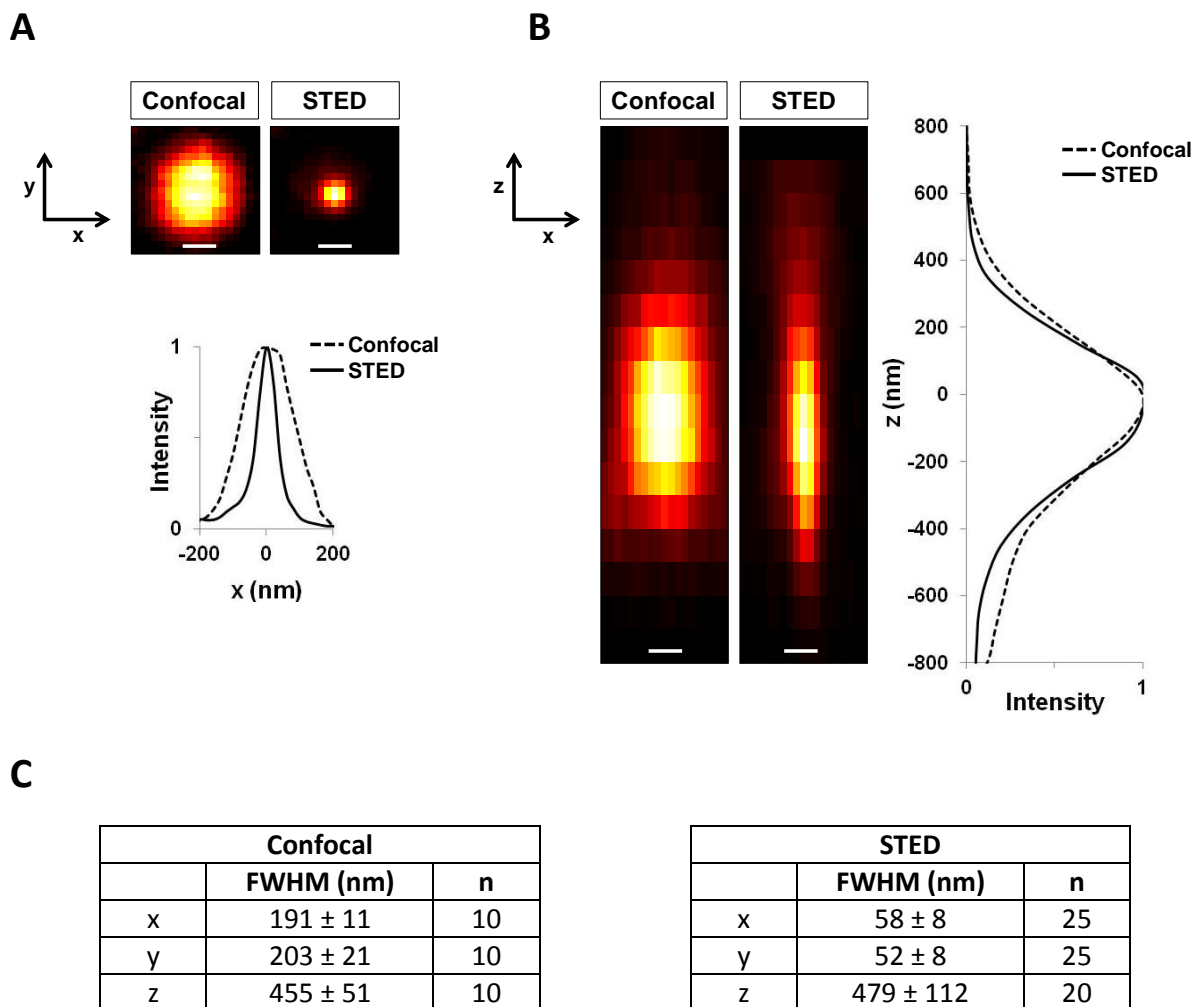
**Figure 2.2 Imaging of fluorescent 20 nm beads to document resolution.** (**A**) Averaged image of n (numbers given by tables in (C)) fluorescent beads imaged in xy and corresponding line profiles along the x axis. (**B**) Averaged image of n (numbers given by tables in (C)) fluorescent beads imaged in xz and corresponding line profiles along the z axis. (**C**) Tables summarize the average full widths at half maximum (FWHM) of fluorescent beads imaged either by the STED or the confocal mode in all three imaging axes. Data are presented as mean ± SD. n = number of measured beads. Scale bars: 100 nm.

## 2.8 Analysis of confocal images

### 2.8.1 Analysis of protein patterns in immunostains

To analyze the striation associated periodicity of Cav3, JPH2 and RyR2 signal patterns, the fast Fourier transformation plugin ("FFT") of ImageJ was used on ROIs measuring 30 μm x 10 μm. This plugin computed the Fourier transform and displayed the power spectrum for each ROI. Analysis of power spectra was modified from Song *et al.* [96] and Wei *et al.* [97]. Power spectra were analyzed by line profiles with a width of 100 pixels. Line profiles of all power spectra in one group were averaged and displayed as a function of spatial frequency.

In this analysis, the dominant frequency at ~0.5 µm$^{-1}$ resulted in the first peak corresponding to a spatial distance of 2 µm, the average Z-line spacing of cardiomyocytes. The amplitude of this first peak was measured independently for each power spectrum as the difference between the highest value of the peak and the smallest value directly before the peak. Peak amplitudes were then averaged per group and displayed as bar graphs.

### 2.8.2 Analysis of Ca$^{2+}$ transients

Using ImageJ, the variability of Ca$^{2+}$ transients was analyzed according to Louch *et al.*, 2006 [89]. Initially, fluo-4/AM line scan images (recorded as described in 2.6.3) were smoothed applying the *"Smooth"* function. The half-maximal fluorescence (F$_{50}$) of the spatially averaged line scan was then used as the threshold level. The leading edge of the thresholded image was outlined to create a profile of the earliest time at which F$_{50}$ was reached. The standard deviation of these values was defined as the dyssynchrony index. Images were only analyzed, when F$_{50}$ was reached along the entire length of the line scan (20 µm).

### 2.9 Analysis of STED images

Before quantitative analysis, all images were linearly deconvolved (Wiener filter) using a two-dimensional Lorentz function (Kernel: corresponding FWHM as determined in Figure 2.2, MATLAB R2009b) [121].

### 2.9.1 Quantitative analysis of the TT network

### 2.9.1.1 Skeleton analysis of the TT network

Skeletons of the TT network were extracted from STED images using the image processing program Fiji [122]. At first, ROIs that enclosed the TT network, but not the surface sarcolemma were defined in intracellular STED images. These ROIs were processed with the following plugins:

*1. ("Enhance Local Contrast (CLAHE)", "blocksize=29 histogram=256 maximum=5 mask=\*None\*")*

*2. ("Smooth")*

*3. ("Statistical Region Merging", "Q=15 showaverages")*

*4. ("Median…", "radius=3")*

*5. ("Robust Automatic Threshold Selection", "noise=25 lambda=3 min=50")*

Binary images of the processed ROIs were then skeletonized using the plugin *"Skeletonize"*. Exemplary skeletons that have been extracted from STED images are shown in Figure 3.14. Quantitative skeleton properties like length and the number of junctions were automatically analyzed with the plugin *"Analyze Skeleton (2D/3D)"*.

*(For detailed description of Fiji plugins please refer to [http://fiji.sc/wiki/index.php/Category:Plugins](http://fiji.sc/wiki/index.php/Category:Plugins).)*

### 2.9.1.2 Orientation analysis of the TT network

To analyze the orientation of individual TT elements, the Fiji plugin *"Directionality"* *("method=[Fourier Components] nbins=180 histogram=0 display_table")* was applied on the skeletonized image data. This plugin computed a histogram for each image indicating the frequency of structures oriented in a given direction with a bin size of 1°. The histogram data of all images per treatment group were averaged and presented as the relative amount of TT elements oriented in a specific angle in relation to the longitudinal cell axis. Accordingly, longitudinal TT elements had an angle of 0°. Transverse TT elements corresponded to the 90° bin. Due to symmetry, the histograms only included values from 0° to 179° (orientations of 0° and 180° were considered to be equal as well as 90° and 270° and so on). In order to illustrate the two-peak behavior, orientation histograms are displayed ranging from -45° to 135° with -45° — -1° corresponding to 135° — 179°.

To additionally obtain the absolute amount of TT elements oriented in a certain direction, the relative histogram data described above were related to the total skeleton length within each ROI (obtained as readout of the *"Analyze Skeleton (2D/3D)"* plugin). The absolute amount of longitudinal TT elements within one image was calculated as the total skeleton length in that image multiplied by the percentage of longitudinal elements in the orientation histogram. Only for this purpose, the percentage of longitudinal elements was defined as the sum of 0° ± 3°. For the absolute amount of transverse TT elements, the same calculation strategy was used, but with the percentage of transverse elements being defined as the sum of 90° ± 3°. Finally, a third group of TT elements with neither longitudinal nor transverse orientation was defined as oblique elements. The percentage of oblique TT elements was calculated as the sum of 45° ± 3° and -45° ± 3°.

**2.9.2 Quantitative analysis of TT cross-sections**

**2.9.2.1 Determination of TT dimensions by 2D Gauss fitting**

Using MATLAB (R2009b) a 2D Gauss function was fitted to the fluorescence signal of individual TT cross-sections both in the STED and in the corresponding confocal image. The orientation of one fit-axis was fixed and aligned with the longitudinal cell axis (X). Accordingly, the second fit-axis was perpendicular to the longitudinal cell axis (Y). Full widths at half maximum (FWHM) of the fitted data were determined along both axes. The TT cross-section area was determined by $A = \prod \cdot (½ X) \cdot (½ Y)$ (ellipse formula).

**2.9.2.2 Contour analysis**

Contour lines of individual TT cross-sections were computed using the MATLAB (R2011b) command "*contourc*" applying a threshold of half the maximal fluorescence intensity per image. All contour lines had a resolution of 120 points. The circumference of each individual TT cross-section was directly computed by this analysis.

To allow comparison of TT contours from different cells and experimental groups, all contours were equally aligned by rotation around their center of mass. After rotation, for each contour the X axis corresponded to the longitudinal cell axis (X).

For comparison of different TT populations (e.g. from different treatment groups), all contour lines from one treatment group were superimposed in space at their center of mass. The results were displayed as color coded 2D probability histograms (see figure 3.6 for example) with a pixel size of 8.3 nm x 8.3 nm.

The radius of individual TT cross-sections was determined as the mean of the 120 radii on its contour line.

**2.9.3 Presentation of z-stacks and 3D reconstruction**

Before reconstruction, all z-stacks were linearly deconvolved using a 3D Wiener filter and the appropriate FWHM as determined in Figure 2.2 as kernel (MATLAB R2009b).

Applying the "3D Viewer" plugin of Fiji [122], z-stacks were presented with the appropriate z-distance either as "volume" (single imaging planes remain distinguishable) or as "surface" (only the surface of the object is reconstructed).

## 2.10 Determination of protein levels by Western blot analysis

Using a micropestle attached to a drill, ventricular cardiomyocytes (prepared as described in 2.5) were homogenized in homogenization buffer (formulation below). Following 30 min incubation at 4°C for solubilization, lysates were centrifuged at 8,000 g for 15 min at 4°C. The supernatant was aliquoted (30 µg of protein each) and immediately snap-frozen in liquid $N_2$

Protein concentrations were determined with a commercial protein detection kit (BCA protein assay kit) according to the manufacturer's instructions.

Proteins were separated on 4 − 12 % gradient gels (NuPAGE®) using 1x MOPS running buffer as recommended by the manufacturer. A prestained protein molecular weight marker was used as size standard. Electrophoresis was performed at 150 V until the first marker band reached the lower end of the gel.

In a wet blotting apparatus, proteins were transferred to nitrocellulose membranes. The blotting module containing (from bottom to top) 2 layers of filter paper, nitrocellulose membrane, the protein gel and 2 layers of filter paper, was incubated in transfer buffer (formulation below) for 30 min. Blotting was performed in transfer buffer at 100 V for 1 h. Uniform protein transfer was confirmed by Ponceau stain of the membrane.

To block unspecific binding, membranes were incubated in TBST (Tris-buffered saline and Tween 20, formulation below) containing 5 % milk powder for 1 h at room temperature.

Primary antibodies were diluted in TBST containing 5 % milk powder (all primary antibodies and dilutions used for Western blots are listed in Table 6.8.1, Supplement). Membranes were incubated with the diluted primary antibodies over night at 4°C. The next day, membranes were washed three times for 10 min with TBST and were then incubated for 1 h with the secondary antibodies diluted in TBST containing 5 % milk powder at room temperature (secondary antibodies and dilutions used for Western blots are listed in Table 6.8.1, Supplement).

After four 10 min washing steps with TBST, proteins were detected by chemiluminescence using the Immobilon™ Western horse raddish peroxidase substrate. Chemiluminescence was recorded and

analyzed by an image station with the appropriate imaging software (Image Station 4000R PRO, Carestream).

**Homogenization buffer**

|                                       | MW (g/mol) | Final concentration |
| ------------------------------------- | ---------- | ------------------- |
| HEPES                                 | 238.31     | 10 mM               |
| Sucrose                               | 342.30     | 300 mM              |
| NaCl                                  | 58.44      | 150 mM              |
| Triton X-100                          | -          | 0.5 %               |
| EGTA                                  | 380.35     | 1 mM                |
| CaCl$_2$                              | 110.98     | 2 mM                |
| PhosSTOP (phosphatase inhibitor cocktail) | -      | 1 tablet / 10 ml    |
| cOmplete (protease inhibitor cocktail)    | -      | 1 tablet / 10 ml    |

**Transfer buffer**

|          | MW (g/mol) | Final concentration |
| -------- | ---------- | ------------------- |
| Tris     | 121.14     | 65 mM               |
| Glycine  | 75.07      | 380 mM              |
| Methanol | 32.04      | 20 %                |

**TBST (Tris-buffered saline and Tween 20)**

|          | MW (g/mol) | Final concentration |
| -------- | ---------- | ------------------- |
| Tris     | 121.14     | 10 mM               |
| NaCl     | 58.44      | 170 mM              |
| Tween 20 | -          | 0.05 %              |
| pH 7.5   |            |                     |

**2.11 Statistics**

Data are presented as mean ± standard error of the mean (SEM) unless indicated differently. Differences between groups were tested for statistical significance using an unpaired 2-tailed T-test (Microsoft Office Excel 2007). In cases a paired T-test was used, this is indicated. Only P values < 0.05 were considered significant.

## 3 Results

### 3.1 STED imaging of TTs in healthy cardiomyocytes

To establish STED imaging of TT membranes in living cardiomyocytes, five different dyes were initially tested. The fluorescently labeled phosphoglycerolipids Atto647N-PE and Atto647N-PE1 as well as the labeled sphingolipid Atto647N-SM had previously been described as suitable dyes for STED imaging of membranes in living PtK2 cells [123]. However, the staining protocols for all three dyes require relatively long incubation (30 min) on ice, followed by imaging at room temperature or even at 37°C. This staining procedure significantly affected living isolated cardiomyocytes as documented by (1) formation of membrane blebs, (2) aberrant contractions and (3) cell death. Alternatively, di-4-ANEPPS is a well established membrane dye, which is often used for voltage imaging in excitable cells. However, Loew, who developed the ANEP dyes, stated that in some cell types di-4-ANEPPS becomes rapidly internalized [124]. Dye internalization was also observed in di-4-ANEPPS stained isolated cardiomyocytes. The resulting unspecific signal did not allow the visualization of the TT system. Exemplary confocal and STED images of a cardiomyocyte stained with di-4-ANEPPS are shown in Figure 3.1. Due to internalization and the failing TT stain, di-4-ANEPPS was not used for further studies.
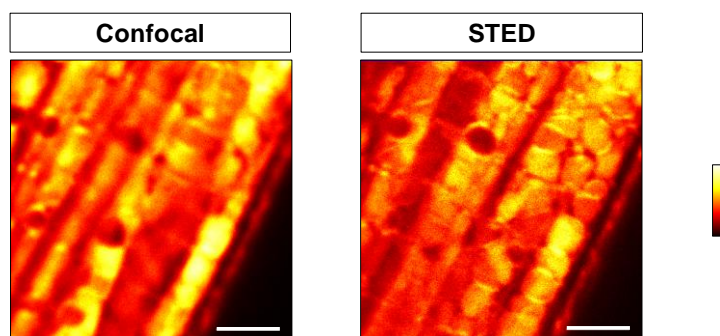


**Figure 3.1 Di-4-ANEPPS internalizes in living cardiomyocytes.** Exemplary confocal and STED images of the same ROI in a di-4-ANEPPS stained cardiomyocyte (20 µM, 10 min, room temperature). During staining, the dye already internalized. The TT system was not specifically stained. Color bar on the right illustrates the look-up table of fluorescence intensity. Scale bars: 2 µm.

In contrast, staining with di-8-ANEPPS (Methods 2.3.1) did not affect freshly isolated ventricular cardiomyocytes. The majority of stained cells exhibited regular sarcomeric striations, no membrane blebs and did not contract. The fluorescence signals were considered sufficiently bright and STED successfully resulted in images with better resolution. Therefore, all subsequent TT imaging studies were performed using di-8-ANEPPS. The right side of Figure 3.2 shows a successfully di-8-ANEPPS

stained cardiomyocyte. Compared to the di-4-ANEPPS example in Figure 3.1, the TT system is clearly visualized.

The region of interest (ROI, 9 µm x 18 µm) for TT imaging was routinely selected in quiescent cells exhibiting regular striations and no membrane blebs. Using the bright field mode of the STED microscope, the status of cardiomyocytes used for TT imaging was documented. The selected ROI was sequentially imaged by the STED and by the confocal mode. Imaging depth was documented for every image as the distance between cell surface and actual imaging plane. Subsequently, I will discriminate between intracellular images that have been taken more than 3 µm inside the cell and submembrane images that have been taken less than 3 µm inside the cell.
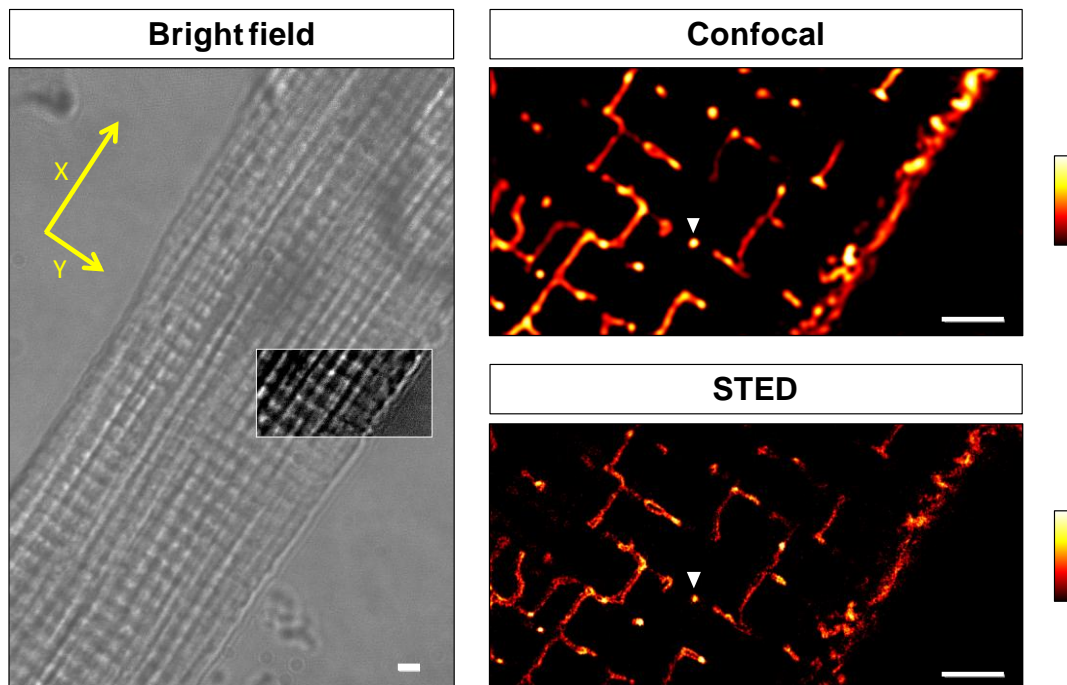


**Figure 3.2 Confocal and STED images of the same ROI in a living di-8-ANEPPS stained cardiomyocyte.** *Left:* Bright field image showing a regular striated living ventricular cardiomyocyte and the ROI that was imaged by the confocal and the STED mode (white box, increased contrast). Yellow arrows indicate orientations of the longitudinal (X) and the transverse (Y) cell axis. *Right:* Intracellular confocal and STED images of the ROI indicated in the bright field image. White triangles highlight an exemplary TT cross-section. Color bars on the right illustrate the look-up table of fluorescence intensity. Scale bars: 2 µm.

The left side of Figure 3.2 shows a bright field image of the central part of a cardiomyocyte and the appropriate ROI. Orientations of the longitudinal (X) and transverse (Y) cell axes are indicated by yellow arrows. The right side shows a confocal and a STED image of the ROI. The fluorescence images show typical intracellular TT network structures inside a healthy cardiomyocyte. Besides the surface sarcolemma, there are TT elements in parallel to the major (longitudinal) cell axis. These are termed

"**longitudinal TT elements**". TT elements which are perpendicular to the major cell axis are termed "**transverse TT elements**". Optical sections of TTs running perpendicular to the imaging plane are referred to as "**cross-sections**". One cross-section is highlighted by a white triangle each in the confocal and in the STED image in Figure 3.2.

### 3.1.1 STED resolves individual TT elements

Sequential imaging of the same ROI by the STED and by the confocal mode allows for direct, quantitative comparison of the same structures imaged by the two different modes. Figure 3.2 already showed that the STED mode provides sharper images with increased detail information compared to the confocal mode. This observation is further illustrated in Figure 3.3, which shows examples of three different types of TT elements. The TT cross-section that has already been highlighted in Figure 3.2 appears clearly smaller in the STED image. Furthermore, images of the transverse and longitudinal TT elements show the underlying hollow membrane structure, the "tubule", which is only resolved by the STED mode.
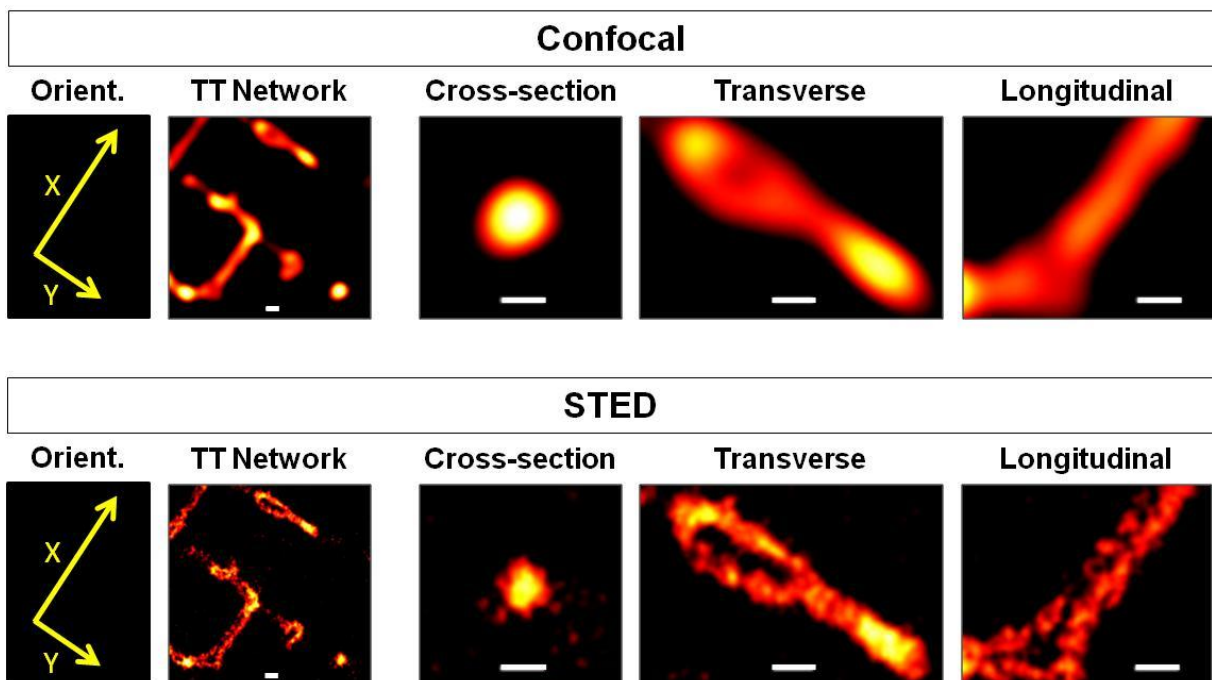


**Figure 3.3 STED images show details of different TT elements.** *Left:* Magnified detail of figure 3.2. Yellow arrows indicate orientations of the longitudinal (X) and the transverse (Y) cell axes. *Right:* "Cross-section" denotes the optical profile of a TT that runs perpendicular to the imaging plan. A transverse TT element runs perpendicular to the major (longitudinal) cell axis and a longitudinal TT element is in parallel to the major cell axis. Scale bars: 200 nm.

**3.1.2 Quantitative analysis of TT cross-sections by 2D Gauss fitting**

Since an improvement of resolution in the STED mode was already apparent by direct comparison with confocal images (Figures 3.2 and 3.3), the next goal was to quantitatively analyze the differences between TT structures in STED and confocal images. For that purpose, initially dimensions of TT cross-sections were determined by 2D Gauss fitting (Methods 2.9.2).

The same set of TT cross-sections was analyzed in STED and confocal images of healthy di-8-ANEPPS stained cardiomyocytes. Intracellular and submembrane images were analyzed separately.
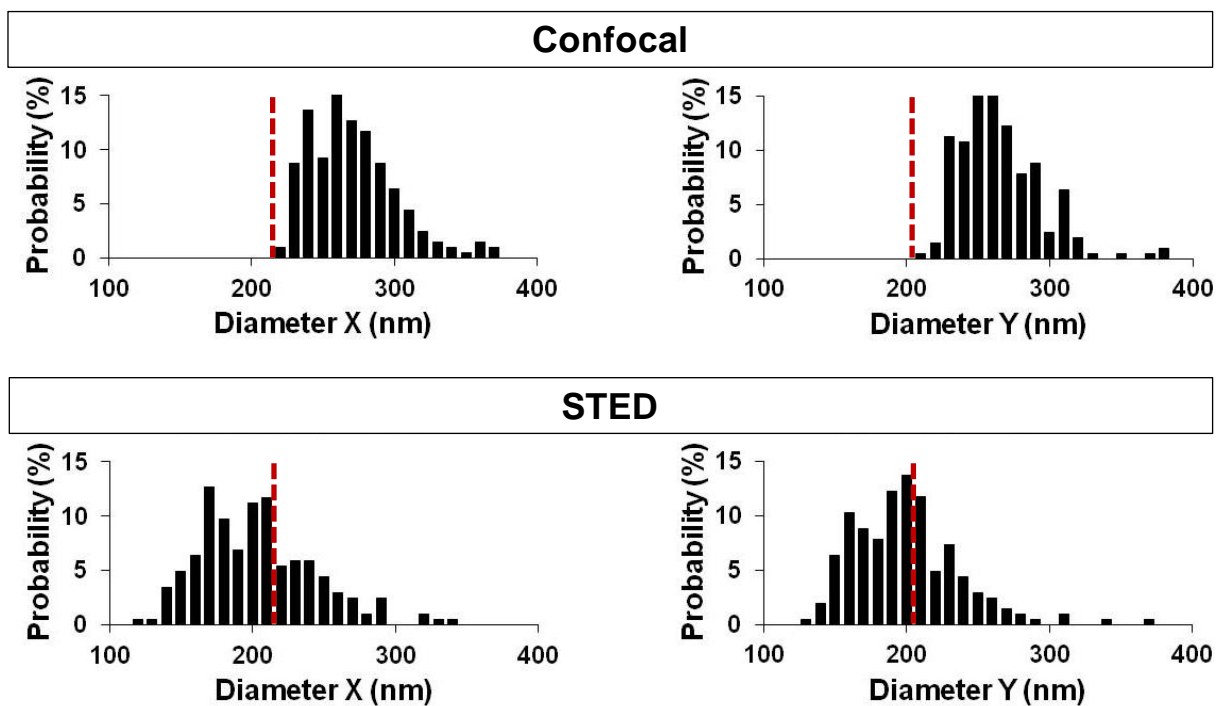


**Figure 3.4 Distribution of intracellular TT diameters determined by 2D Gauss fitting.** Histograms for diameters of 205 TT cross-sections (43 cells, 3 mice) determined in intracellular images. The same set of TT cross-sections was analyzed in STED and confocal images. Diameters were determined as FWHM by 2D Gauss fitting in parallel to the longitudinal cell axis (X) and perpendicular to the longitudinal cell axis (Y). Red dashed lines mark the confocal resolution limit.

In the intracellular group, dimensions of 205 TTs (in 43 cells from 3 different mice) were determined. Figure 3.4 shows the distribution of TT diameters determined in parallel to the longitudinal cell axis (X) and perpendicular to it (Y) in intracellular confocal and STED images. For X and Y the confocal histograms abruptly end at 220 nm and 210 nm respectively. These values approximately represent the confocal resolution limit (red dashed line). The STED histograms are not restricted to that limit. For X and Y the histograms are broader and contain values down to 120 nm.

Clear shifts towards smaller diameters in STED histograms as well as abruptly ending confocal histograms were also observed for dimensions of TTs in submembrane images. Histograms representing the distribution of TT diameters in submembrane images are shown in Figure 6.1 (Supplement).

Table 3.1 summarizes the mean TT diameters in X and Y as well as the mean TT areas that have been calculated from these diameters by the ellipse formula ($A = \prod \cdot \frac{1}{2}X \cdot \frac{1}{2}Y$). In both groups – intracellular and submembrane –all determined parameters are significantly smaller for TTs analyzed in STED images. The mean TT cross-section area for example appears approximately 44 % smaller in STED images than in confocal images.

**Table 3.1 Dimensions of TT cross-sections in healthy cardiomyocytes.** The same TT cross-sections were analyzed in STED and confocal images. Differences between STED and confocal dimensions were tested for statistical significance by a paired T-test. Mean TT diameters and areas were determined by 2D Gauss fitting. Mean circumferences were determined by contour analysis. Data are presented as mean ± SEM. Intracellular: 205 TTs in 43 cells derived from 3 different mice. Submembrane: 182 TTs in 55 cells derived from 3 different mice. **\***: $p < 0.001$ vs. confocal (paired T-test).

| Imaging mode | Diameter X (nm) | Diameter Y (nm) | Area (nm$^2$) | Circumference (nm) |
|---|---|---|---|---|
| **Intracellular** | | | | |
| Confocal | 265.9 ± 2.1 | 261.1 ± 2.0 | 54,696.8 ± 696.0 | 918.9 ± 5.9 |
| STED | 198.7 ± 2.8 * | 195.2 ± 2.6 * | 30,899.5 ± 740.0 * | 672.9 ± 8.7 * |
| **Submembrane** | | | | |
| Confocal | 273.1 ± 2.7 | 266.1 ± 2.1 | 57,245.9 ± 789.9 | 945.3 ± 6.7 |
| STED | 206.0 ± 3.5 * | 194.6 ± 2.7 * | 31,810.2 ± 769.6 * | 708.6 ± 9.8 * |

TT cross-sections appeared smaller in STED images. Additionally, morphological details were revealed and in some cases even the underlying hollow structure was resolved. Figure 3.5 A shows an exemplary TT cross-section whose hollow structure was only resolved by STED but not by the confocal mode. Assuming that all TT elements are hollow structures, it has to be concluded that only some are resolved under the given conditions.

**3.1.3 Quantitative analysis of TT cross-sections by contour analysis**

To further investigate the morphology of individual TT cross-sections, contours were quantitatively analyzed. Contour lines were computed at half the maximal fluorescence intensity of one TT cross-section (Methods 2.9.2). Figures 3.5 B and D show contours of the cross-sections in 3.5 A and C respectively. For the same TT cross-section contours were extracted from the STED and the confocal image.

**A**



**B**



**C**



**D**
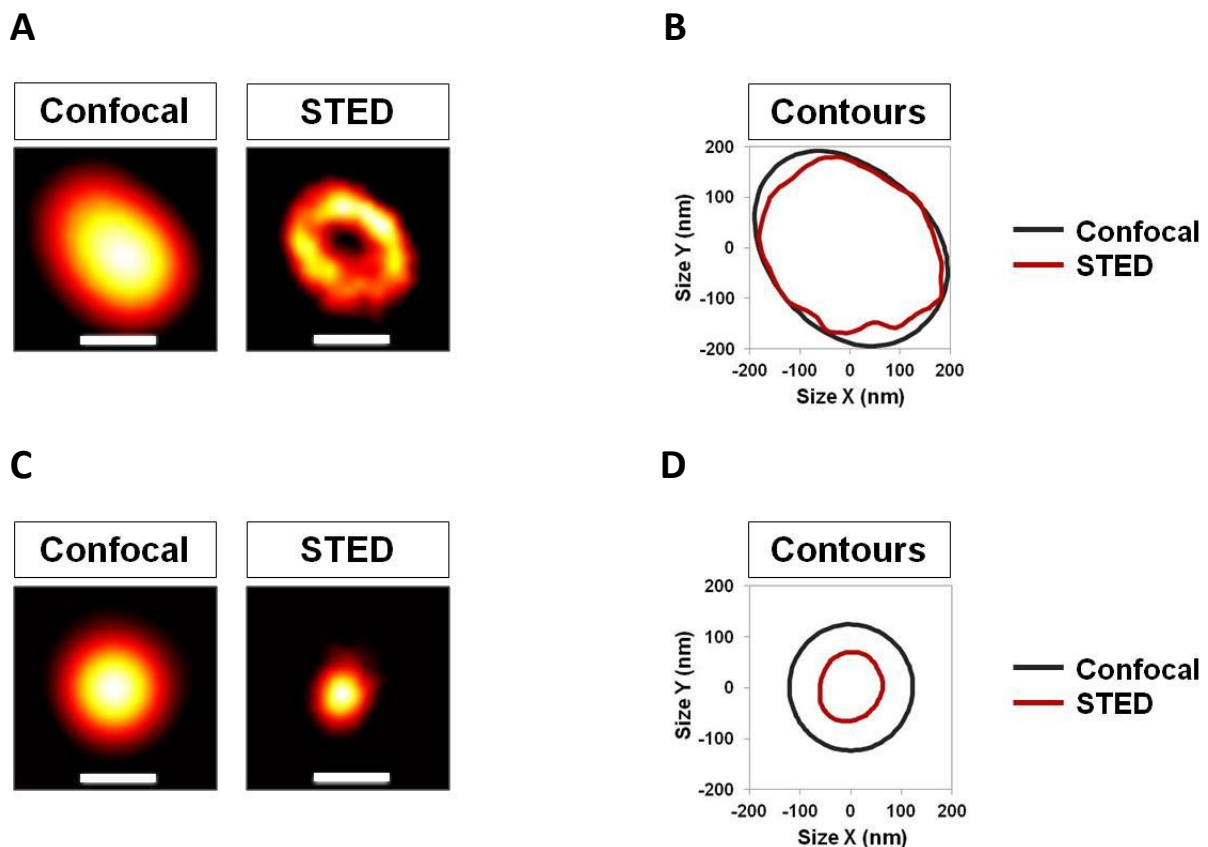


**Figure 3.5 STED and confocal images of individual TT cross-sections and corresponding contours.** (*A*) Confocal and STED image of a hollow TT cross-section imaged 5.9 μm inside the cell. (*B*) Contours of the TT cross-section shown in *A* extracted from the STED (red line) and from the confocal image (black line). (*C*) Confocal and STED image of a TT cross-section imaged 3.9 μm inside the cell. (*D*) Contours of the TT cross-section shown in *C* extracted from the STED (red line) and from the confocal image (black line). Scale bars (200 nm) represent the orientation of the longitudinal cell axis.

Besides being a little smaller, the contour of the hollow TT cross-section extracted from the STED image in Figure 3.5 A showed more details of the TT morphology than the contour extracted from the confocal image. The contours of the TT cross-section in Figure 3.5 C confirmed the observation that it appeared clearly smaller in the STED image.

In order to compare contours from different groups of TT cross-sections, 2D contour histograms were generated (Methods 2.9.2). Contours were extracted from STED and confocal images of the same TT cross-sections. For each group – STED and confocal – 2D histograms were generated by superposition of all corresponding contours. Again, intracellular and submembrane images were analyzed separately. The same sets of TT cross-sections that had been analyzed by 2D Gauss fitting (Results 3.1.2) were additionally used for contour analysis. Figure 3.6 shows the 2D histograms for intracellular TT cross-sections analyzed in confocal and STED images.
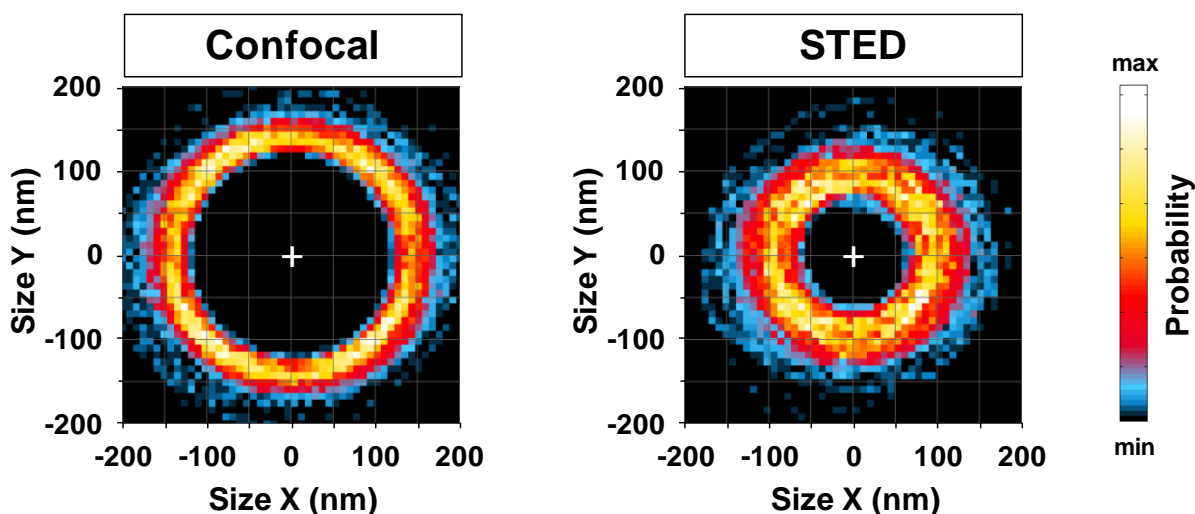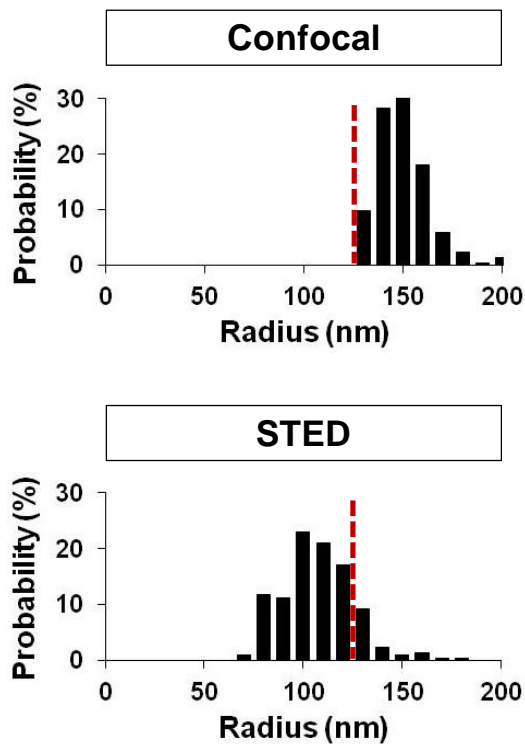


**Figure 3.6 2D contour histograms of intracellular TT cross-sections.** 2D histograms for 205 TT contours extracted from intracellular STED and confocal images. + indicates the point where contours were superimposed (their center of mass). The x-axis corresponds to the orientation of the longitudinal cell axis. The color bar on the right illustrates the probability that a contour hits a pixel: black (min) = low probability, white (max) = high probability.

The STED 2D contour histogram in Figure 3.6 looks significantly different compared to the confocal histograms. While the superposition of contours extracted from confocal images resulted in a narrow circular distribution with an average radius of about 150 nm, the superposition of contours extracted from STED images provided a broader distribution with an average radius of less than 100 nm. A broader distribution composed of contours with smaller radii was also observed when TT cross-sections from submembrane images were analyzed. This is shown in Figure 6.2 (Supplement).

Another parameter resulting from contour analysis was the radius of each TT cross-section calculated as the mean of the 120 radii on its contour line. Radius distributions of the before described sets of TT cross-sections are shown in Figure 3.7. As already observed for TT diameters determined by 2D Gauss fitting (Figure 3.4), distributions of TT radii determined by contour analysis in STED images

were broader and clearly shifted towards smaller values compared to distributions of radii determined in confocal images.

## A Intracellular

## B Submembrane
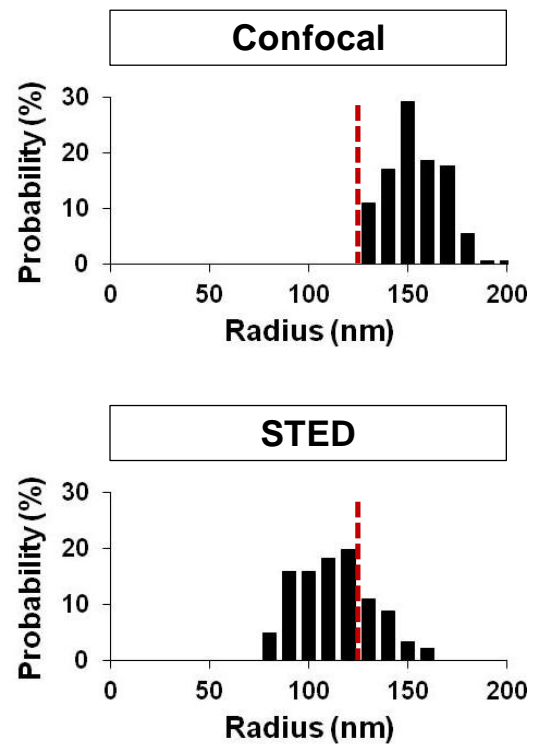


**Figure 3.7 Distributions of radii determined by contour analysis.** The same sets of TT cross-sections were analyzed in STED and confocal images. (**A***)* Histograms for radii of 205 TT cross-sections determined in intracellular images. (**B**) Histograms for radii of 182 TT cross-sections determined in submembrane images. Red dashed lines mark the lower end of the confocal radius distributions.

Mean circumferences determined by contour analysis are summarized in Table 3.1. Like diameters and area determined by 2D Gauss fitting, also the mean circumference of TT cross-sections determined by contour analysis was significantly smaller when analyzed in STED images.

Taken together, imaging of TT structures in healthy living cardiomyocytes showed that STED improves resolution and results in sharper, more detailed images. The morphology of individual TT cross-sections was uncovered by STED and could be quantitatively analyzed by two different and independent methods.

## 3.2 Remodeling of TTs and associated proteins after MI

### 3.2.1 The post-MI mouse model

To investigate TTs during progressive HF in mice, a previously established post-MI mouse model was used [114]. To induce a large MI, the LAD coronary artery was proximally ligated (Methods 2.1.1). Cardiomyocytes were isolated and analyzed 4 weeks after MI (4pMI) or 8 weeks after MI (8pMI). As control, cardiomyocytes from Sham operated mice were isolated, analyzed and compared to 4pMI and 8pMI cells (the Sham operation is also explained in Methods 2.1.1). Mouse operations were performed by Julia H. Steinbrecher (Dept. of Cardiology and Pulmonology, University Medical Center, Göttingen).

The post-MI in vivo phenotype was characterized by echocardiography. Mouse echocardiography was performed by Kirsten Koschel (Dept. of Cardiology and Pulmonology, University Medical Center, Göttingen). Figure 3.8 shows that the left ventricular inner diameter in diastole (LVID,d) was progressively increased post-MI, indicating cardiac dilation (Figure 3.8. A). The posterior wall thickness in diastole (PWTh,d) was also progressively increased, indicating hypertrophy (Figure 3.8. B). A progressive loss of heart function was shown by a decreased ejection fraction (EF) post-MI (Figure 3.8. C). Hypertrophy was further confirmed by determination of the heart weight to body weight ratio (HW/BW) directly before cardiomyocytes were isolated. Figure 3.8 D summarizes HW/BW for all MI and Sham operated mice that have been used for cardiomyocyte isolation and further analysis. HW/BW was progressively increased post-MI.
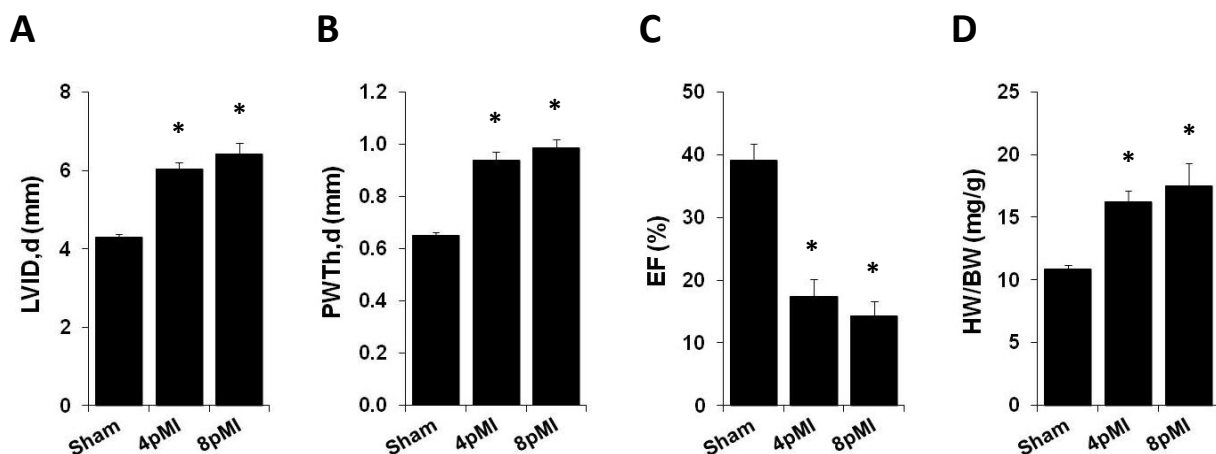


**Figure 3.8 Echocardiographic parameters and HW/BW following MI**. (*A*) Left ventricular inner diameter in diastole (LVID,d) (*B*) Posterior wall thickness in diastole (PWTh,d) (*C*) Ejection fraction (EF). Parameters in (*A*) − (*C*) were determined by echocardiography. (*D*) Heart weight to body weight ratio (HW/BW) determined directly before cardiomyocyte isolation. Data are presented as mean ± SEM from the following number of mice: Sham 9, 4pMI 8, 8pMI 7. **\***: p < 0.001 vs. Sham (unpaired T-test).

A third parameter confirming hypertrophic remodeling post-MI was the size of isolated cardiomyocytes. To determine cell dimensions, fixed cardiomyocytes were used (Methods 2.4.2 and 2.6.2). Figure 3.9 shows that cardiomyocytes became progressively wider and longer post-MI and that consequentially their cross-section area was also increased.
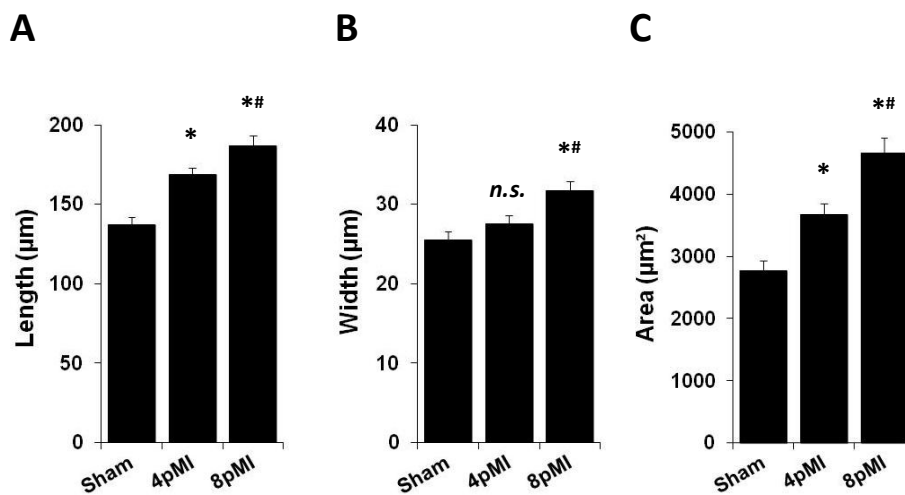


**Figure 3.9 Cardiomyocyte dimensions increase progressively post-MI**. Dimensions were manually determined in fixed isolated ventricular cardiomyocytes. (**A**) Cardiomyocyte length. (**B**) Cardiomyocyte width. (**C**) Cardiomyocyte cross-section area. Data are presented as mean ± SEM from the following number of cells: Sham 36, 4pMI 42, 8pMI 46. *n.s.*: not significant. **\***: p < 0.001 vs. Sham. **#**: p < 0.05 vs. 4pMI (unpaired T-test).

### 3.2.2 TT remodeling after MI

Sham, 4pMI and 8pMI cardiomyocytes were stained with di-8-ANEPPS and a ROI was imaged by the confocal and the STED mode as described in 3.1. Regular striations and the absence of membrane blebs were documented in bright field images. Figure 3.10 A illustrates that STED images of Sham cardiomyocytes showed regularly aligned TTs with rectangular transverse and longitudinal components. 4pMI cardiomyocytes showed enlarged TT structures and minor changes in regularity, whereas the TT network was severely misaligned 8pMI and exhibited strongly enlarged TT structures.

Figures 3.10 B and C illustrate that even strongly enlarged TT structures were only resolved by the STED mode. Confocal imaging resulted in blurred images that did not resolve the underlying TT morphology.

**A**
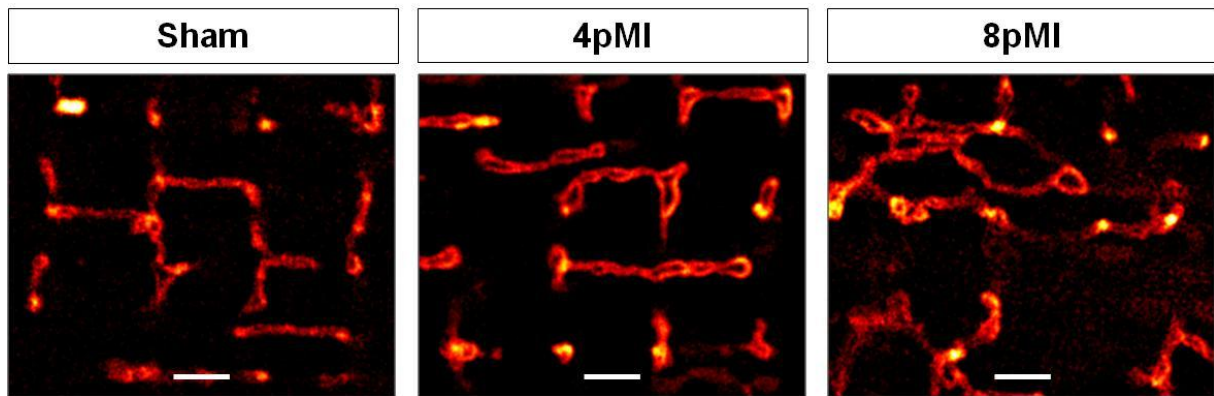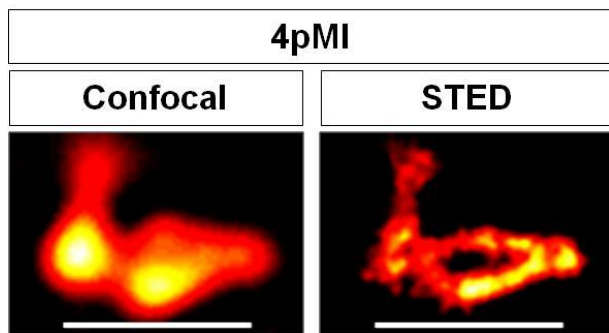


**B**                                                            **C**
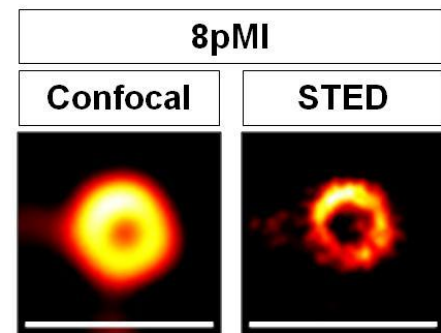


**Figure 3.10 STED shows progressive membrane remodeling post-MI.** (**A**) STED images of intracellular TT structures in Sham, 4pMI and 8pMI cardiomyocytes. (**B**) Confocal and STED image of the same enlarged intracellular 4pMI TT structure. (**C**) Confocal and STED image of the same enlarged intracellular 8pMI TT cross-section. Scale bars (1 µm) represent the orientation of the longitudinal cell axis.

### 3.2.3 MI leads to enlarged TT cross-sections

In order to quantitatively analyze dimensions of TT cross-sections post-MI, the methods described in 3.1.2 and 3.1.3 were applied. Cross-section diameters and area were determined by 2D Gauss fitting. Circumferences were determined by contour analysis. Intracellular and submembrane STED images of Sham, 4pMI and 8pMI cardiomyocytes were analyzed.

Table 3.2 summarizes the dimensions of TT cross sections determined in intracellular STED images. 2D Gauss fitting revealed that 4pMI intracellular cross-sections were enlarged by 12 % and 8pMI even by 22 % (Sham: 30,604 $nm^2$, 4pMI: 34,354 $nm^2$, 8pMI: 37,292 $nm^2$). Contour analysis showed that also the cross-section circumference was increased by 5 % 4pMI and by 14 % 8pMI (Sham: 657 nm, 4pMI: 693 nm, 8pMI: 749 nm).

**Table 3.2 Intracellular TT cross-section dimensions increase progressively post-MI.** Dimensions of TT cross-sections were determined in intracellular STED images of Sham, 4pMI and 8pMI cardiomyocytes. Mean TT diameters and areas were determined by 2D Gauss fitting. Mean circumferences were determined by contour analysis. **\***: p < 0.05 vs. Sham. **#**: p < 0.05 vs. 4pMI (unpaired T-test). Data are presented as mean ± SEM from the following numbers of TT cross-sections (cells) per treatment group: Sham 627 (90), 4pMI 237 (44), 8pMI 290 (46).

| Treatment group | Diameter X (nm) | Diameter Y (nm) | Area (nm$^2$) | Circumference (nm) |
|---|---|---|---|---|
| Sham | 198.4 ± 1.9 | 195.5 ± 1.9 | 30,603.9 ± 439.0 | 656.5 ± 5.6 |
| 4pMI | 205.7 ± 2.9 * | 210.1 ± 3.2 * | 34,353.8 ± 854.8 * | 692.6 ± 9.5 * |
| 8pMI | 213.0 ± 3.4 * | 219.9 ± 3.3 *# | 37,291.9 ± 948.5 *# | 748.9 ± 11.2 *# |

In submembrane STED images, only 8pMI TT cross-sections were enlarged. Dimensions of submembrane TT cross-sections are summarized in Table 3.3. While diameters, area and circumference were not changed 4pMI compared to Sham, 8pMI cross-section area was enlarged by 15 % (Sham: 30,389 nm$^2$, 8pMI: 35,090 nm$^2$) and circumference by 7 % (Sham: 656 nm, 8pMI: 701 nm).

**Table 3.3 Submembrane TT cross-section dimensions increase 8pMI.** Dimensions of TT cross-sections were determined in submembrane images of Sham, 4pMI and 8pMI cardiomyocytes. Mean TT diameters and areas were determined by 2D Gauss fitting. Mean circumferences were determined by contour analysis. *n.s.*: not significant. **\***: p < 0.05 vs. Sham. **#**: p < 0.05 vs. 4pMI. Data are presented as mean ± SEM from the following numbers of TT cross-sections (cells) per treatment group: Sham 683 (92), 4pMI 343 (61), 8pMI 253 (48).

| Treatment group | Diameter X (nm) | Diameter Y (nm) | Area (nm$^2$) | Circumference (nm) |
|---|---|---|---|---|
| Sham | 201.0 ± 2.0 | 190.5 ± 1.8 | 30,388.9 ± 465.5 | 656.0 ± 5.6 |
| 4pMI | 199.5 ± 2.7 *n.s.* | 190.3 ± 2.6 *n.s.* | 29,853.1 ± 567.1 *n.s.* | 649.4 ± 7.5 *n.s.* |
| 8pMI | 214.7 ± 3.3 *# | 205.7 ± 3.3 *# | 35,089.9 ± 884.5 *# | 701.0 ± 10.4 *# |

As described before, TT cross-section contour data were summarized in 2D histograms for each treatment group. 2D contour histograms for intracellular TT cross-sections are shown in Figure 3.11. The 2D histogram for contours extracted from Sham TTs shows a symmetrical, circular distribution

with only little deviation. The distribution of contours extracted from 4pMI intracellular images in already shows alterations in the circular crest and more signals in the periphery representing larger TT cross-sections. Heterogeneity, especially in the periphery, further increased 8pMI. An increasing number of TT cross-sections with large diameters correlates well with the observed progressive increase of mean TT dimensions post-MI (as summarized in Table 3.2).
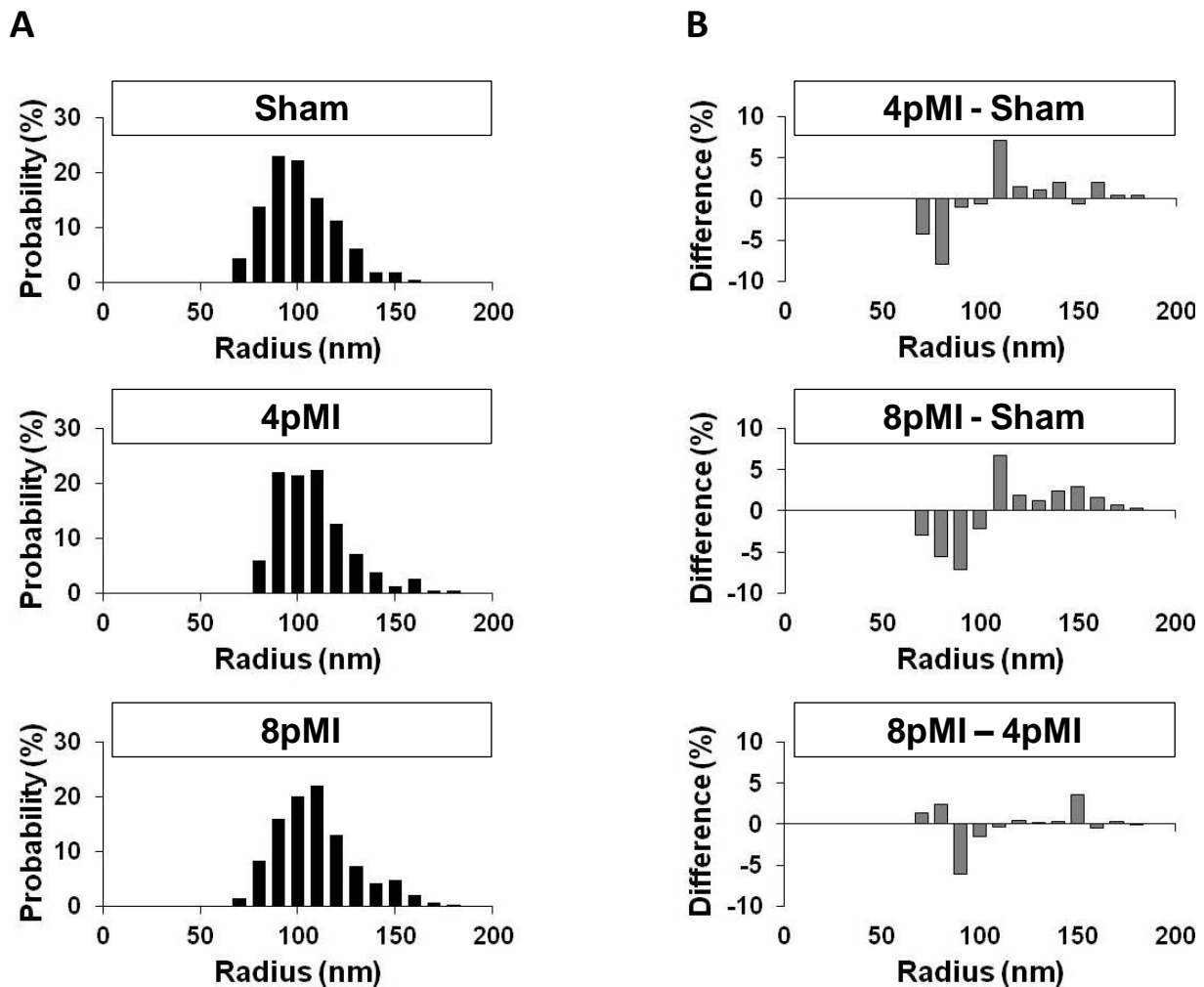
2D contour histograms for TT cross-sections in submembrane images are shown in Figure 6.3 (Supplement). In submembrane 2D histograms, only 8pMI the distribution differed from Sham. It showed a less uniform circular crest and more heterogeneous signals in the periphery. This is again in good correlation with the observation that mean TT dimensions in submembrane images are significantly increased only 8pMI (as summarized in Table 3.3).
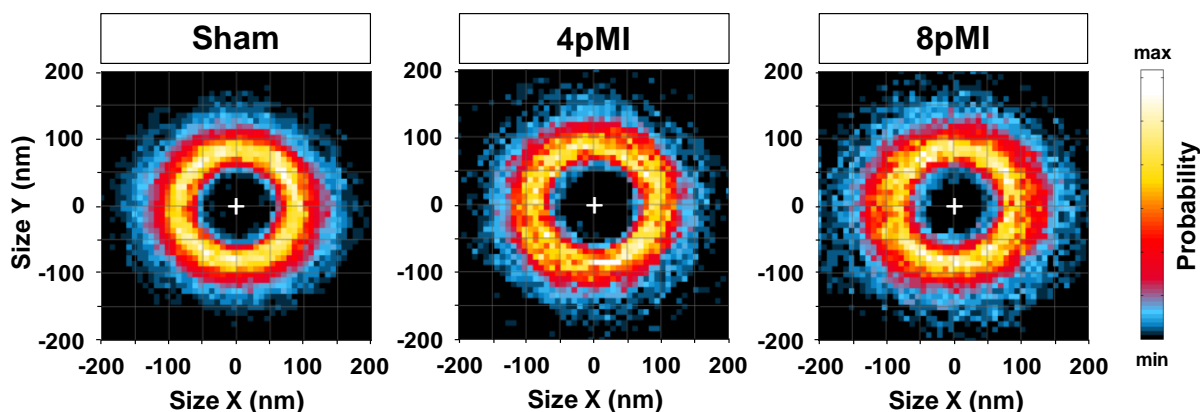


**Figure 3.11 2D contour histograms of intracellular TT cross-sections**. 2D histograms for the following number of TT contours (cells) extracted from intracellular images: Sham 627 (90), 4pMI 237 (44), 8pMI 290 (46). + indicates the point where contours were superimposed (their center of mass). The x-axis corresponds to the orientation of the longitudinal cell axis. The color bar on the right illustrates the probability that a contour hits a pixel: black (min) = low probability, white (max) = high probability.

As another parameter resulting from contour analysis, radii of TT cross-sections were calculated. Radius distributions of intracellular Sham, 4pMI and 8pMI TT cross-sections are shown in Figure 3.12 A. To clarify the difference between distributions of two treatment groups, histograms were subtracted from each other (Figure 3.12 B). Difference histograms show that the 4pMI group contains fewer cross-sections with radii smaller than 100 nm but more cross-sections with radii larger than 100 nm compared to the Sham group. This difference is even more pronounced in the direct comparison of 8pMI with Sham TTs. Accordingly, subtraction of the 4pMI from the 8pMI histogram shows that the 4pMI group contains more cross-sections with radii smaller than 100 nm and less with a radius larger than 100 nm.

**A**                                                                    **B**



**Figure 3.12 Distributions of radii determined by contour analysis in intracellular images.** Radii were determined as the mean of 120 radii in one contour line. (**A**) Histograms for the following number of TT cross-sections (cells) extracted from intracellular images: Sham 627 (90), 4pMI 237 (44), 8pMI 290 (46). (**B**) Differences between the radius distributions were calculated by subtraction of histograms from the indicated treatment groups.

Radius distributions of TT cross-sections in submembrane images are shown in Figure 6.4 (Supplement). As for the previous analyses of TT cross-section dimensions in submembrane images, there was no measureable difference between the distribution of radii from 4pMI and Sham TTs. Changes in the radius distribution of submembrane TTs occurred only 8pMI. The 8pMI histogram contains clearly less TTs with a radius smaller than 100 nm and more with a radius larger than 100 nm compared to the Sham and hence also to the 4pMI group.

In summary, quantitative analysis of TT cross-sections showed a homogenous population of TT cross-sections with a mean diameter of approximately 200 nm in Sham cardiomyocytes. Post-MI this population was replaced by an increasingly heterogeneous population of cross-sections which were in part strongly enlarged. Post-MI changes were more pronounced in intracellular images where they

were already detectable 4pMI. In submembrane images changes were less pronounced and not detectable until 8pMI.

### 3.2.4 STED reveals proliferative TT network remodeling after MI

As further properties of TTs after MI, complexity and composition of the TT network were investigated. To be able to quantify changes in the TT network, skeletons were extracted from STED images of Sham, 4pMI and 8pMI cardiomyocytes (Methods 2.9.1). Figure 3.14 shows exemplary STED images of all groups and the corresponding skeletons that have been extracted from these images. Skeletons were only extracted from intracellular images, because submembrane TT images usually showed a more fractured, punctate pattern without intact networks that could be analyzed. Typical submembrane TT images of a Sham and an 8pMI cardiomyocyte are shown in Figure 3.15.
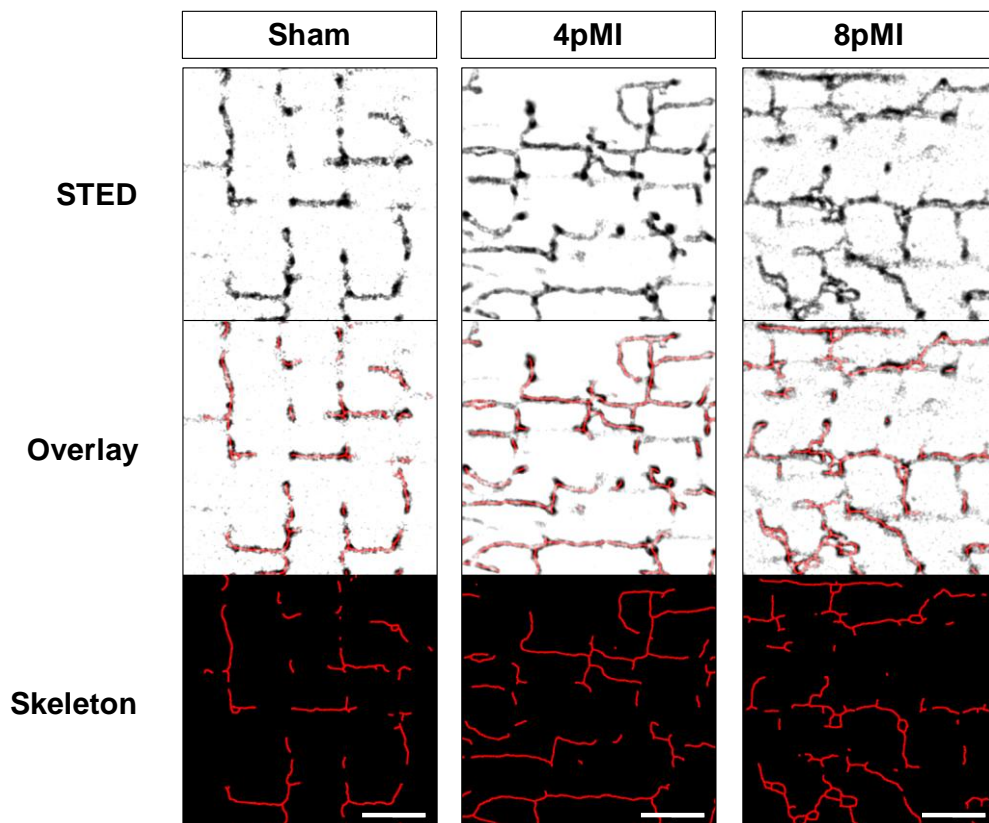


**Figure 3.14 Skeletons reveal progressive TT network remodeling post-MI.** *Upper row:* Representative STED images of TT networks in Sham, 4pMI and 8pMI cardiomyocytes. Grayscale look-up table: white represents pixels without fluorescence and black represents the brightest pixels. *Middle row:* Overlay of STED images with the extracted skeletons. *Lower row:* Skeletons that have been extracted from the STED images in the upper row. Scale bars (2 µm) represent the orientation of the longitudinal cell axis.

**A**                                          **B**
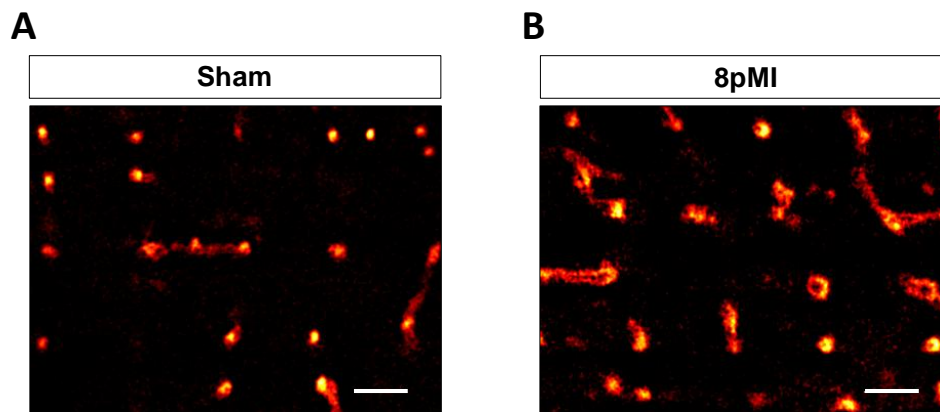


**Figure 3.15 Typical submembrane TT images in Sham and 8pMI cardiomyocytes.** Submembrane images do usually not exhibit an extensive TT network that could be used for extraction of skeletons. (**A**) TTs imaged 2 µm inside a Sham cardiomyocyte. (**B**) TTs imaged 1 µm inside an 8pMI cardiomyocyte. Several TT cross-sections appear clearly enlarged compared to the Sham example. Scale bars (1 µm) represent the orientation of the longitudinal cell axis.

The exemplary STED images of TTs in Sham, 4pMI and 8pMI cardiomyocytes in Figure 3.10 already showed a progressive loss of regularity post-MI accompanied by an increasing number of enlarged structures. This observation is confirmed by the STED images and the extracted skeletons in Figure 3.14. Skeletons illustrate that extremely enlarged TT structures are made up of bifurcating TT elements. In order to characterize complexity of a TT network, the number of triple junctions – or the number of bifurcating TT elements – was counted and normalized to the corresponding area. Another determined parameter was the total length of TT network elements in a defined area.

Both parameters, number of triple junctions and total network length were analyzed in Sham, 4pMI and 8pMI images. The results are summarized in Figure 3.16. Figure 3.16 A shows a significant increase of the total skeleton length post-MI, which is slightly longer 4pMI than 8pMI (Sham: 0.38 µm/µm$^2$, 4pMI: 0.52 µm/µm$^2$, 8pMI: 0.50 µm/µm$^2$). The number of triple junctions (Figure 3.16 B) progressively increased post-MI up to almost twofold 8pMI compared to the Sham group (Sham: 0.20/µm$^2$, 4pMI: 0.33/µm$^2$, 8pMI: 0.38/µm$^2$).
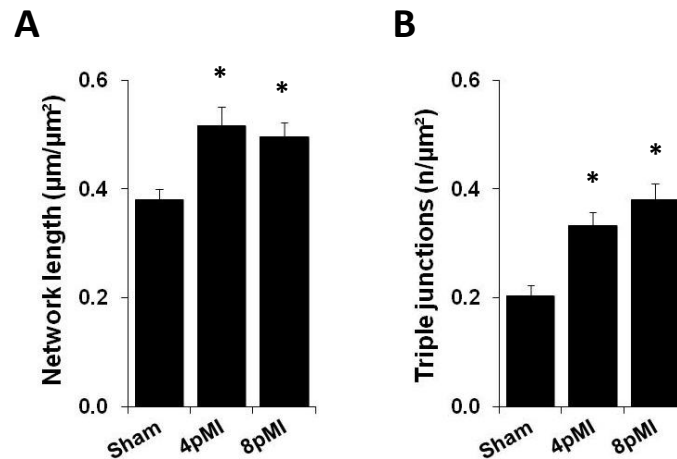
**Figure 3.16 TT network length and complexity increase after MI.** As a measure of TT network complexity the total network length per area and the number of triple junctions per area were calculated from skeletonized STED images of Sham, 4pMI and 8pMI cardiomyocytes. (**A**) Total network length per area. (**B**) Number of triple junctions per area. **\***: $p < 0.01$ vs. Sham. Data are presented as mean ± SEM from the following number of cells per treatment group: Sham 23, 4pMI 19, 8pMI 19.

Besides complexity, the composition of TT networks in the different treatment groups was analyzed. Therefore, the orientation of all elements in a TT network was determined. As already defined in 3.1, TT elements in parallel to the longitudinal cell axis are termed "longitudinal elements". TT elements perpendicular to the longitudinal cell axis are termed "transverse elements". In rotated images whose horizontal axis corresponds to the longitudinal cell axis, longitudinal elements have an orientation of 0°. Transverse TT elements have an orientation of 90°. Figure 3.17 A shows how TT elements in the different treatment groups were oriented. Orientations of all TT elements in images of one treatment group were summarized in histograms. The Sham histogram shows a distribution with two similar peaks at 0° (longitudinal elements) and at 90° (transverse elements). This confirms the observation that TT networks in healthy cardiomyocytes are mainly composed of regular longitudinal and transverse elements.

4pMI the longitudinal peak is clearly larger compared to the Sham group. This finding is consistent with the 4pMI example in Figure 3.14 which contains more longitudinal elements than the Sham example. The transverse peak in the 4pMI histogram decreases compared to Sham.

8pMI both the longitudinal and the transverse peak are decreased compared to Sham. But while the amplitude at 0° is smaller, the peak becomes wider, indicating an increase of oblique elements. This finding is also consistent with Figure 3.14, where the 8pMI example is mainly composed of TT elements which are neither exactly longitudinal nor transverse.

**A**
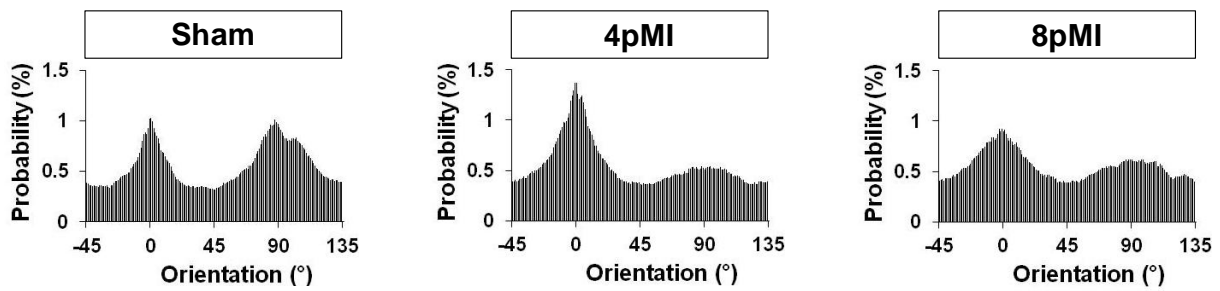


**B**
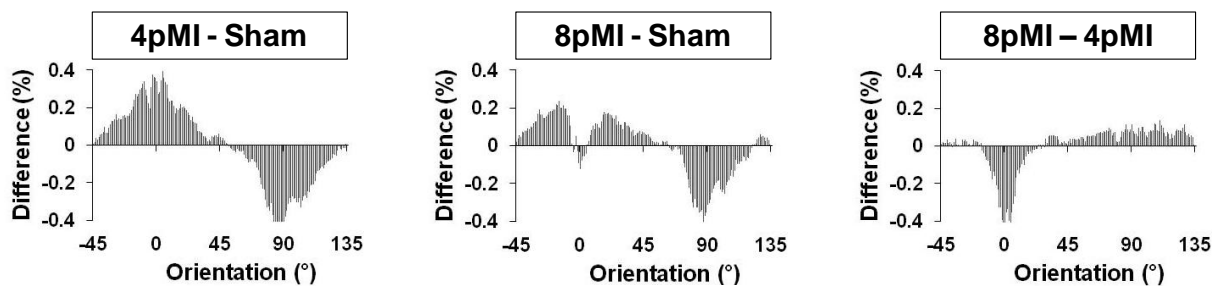


**Figure 3.17 Orientation of TT network elements changes differentially post-MI.** Histograms summarize orientations of all TT elements in images of one treatment group. 0° represent a longitudinal orientation of TT elements. 90° represent a transverse orientation. (**A**) Orientation histograms for the following number of cells per treatment group: Sham 23, 4pMI 19, 8pMI 19. (**B**) Differences between the distributions were calculated by subtraction of histograms from the indicated treatment groups.

Since a presentation of datasets as histograms only displays relative values and changes, orientations of TT network elements were additionally determined as absolute values. For this purpose the total network lengths per treatment group already described in Figure 3.16 (Sham: 0.38 µm/µm$^2$, 4pMI: 0.52 µm/µm$^2$, 8pMI: 0.50 µm/µm$^2$) were used as reference values (for detailed description see Methods 2.9.1). The absolute amount of longitudinal TT elements in one image was defined as the total network length in that image multiplied by the sum of histogram values for 0° ± 3° for the same image. For the absolute amount of transverse TT elements, the total network length was multiplied by the histogram values for 90° ± 3°. The sum of 45° ± 3° and -45° ± 3° was defined as the percentage of oblique elements, which are neither longitudinally not transversely oriented.

Figure 3.18 summarizes the absolute values of the different components of the TT network for each treatment group and the differential changes between groups. While the relative amount of transverse TT elements shown in Figure 3.17 clearly decreases post-MI, the absolute amount is only slightly decreased 4pMI but not 8pMI (Sham: 0.025 µm/µm$^2$, 4pMI: 0.018 µm/µm$^2$, 8pMI: 0.021 µm/µm$^2$).

The strong relative increase of longitudinal TT elements 4pMI is confirmed by the analysis of absolute values. Compared to Sham, 8pMI the absolute amount of longitudinal TT elements is only slightly increased (Sham: 0.025 µm/µm², 4pMI: 0.047 µm/µm², 8pMI: 0.032 µm/µm²).

While relative values suggested a stronger increase of oblique TT elements 8pMI than 4pMI, the analysis of absolute values showed an increase of oblique elements for both 4pMI and 8pMI to almost the same extend (Sham: 0.019 µm/µm², 4pMI: 0.029 µm/µm², 8pMI: 0.028 µm/µm²).
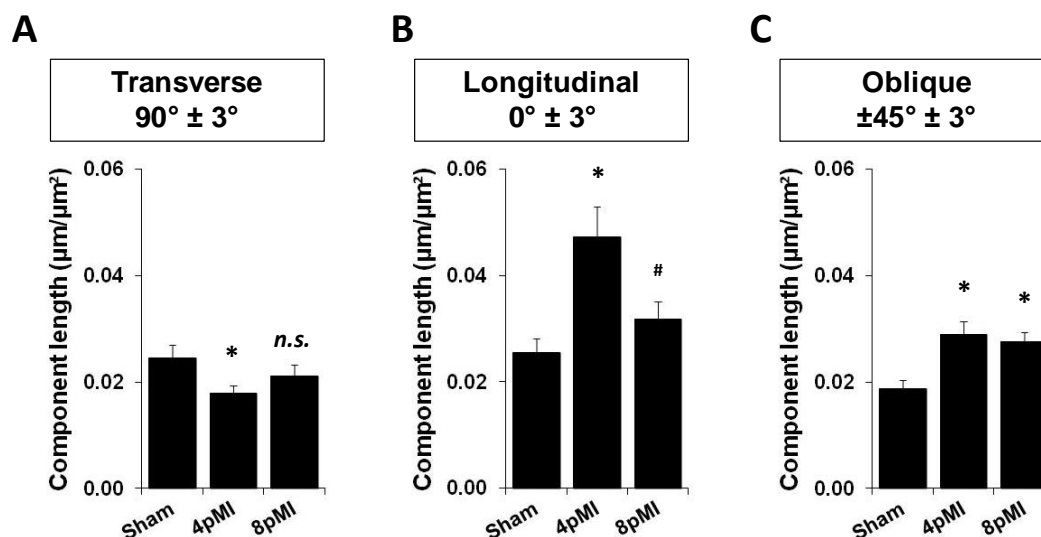


**Figure 3.18 Components of the TT network change differentially post-MI.** Absolute amount of TT network components per area in Sham, 4pMI and 8pMI cardiomyocytes. (**A**) 90° ± 3° are referred to as the transverse component. (**B**) 0° ± 3° are referred to as the longitudinal component. (**C**) ±45° ± 3° are defined as the oblique component. *n.s.*: not significant. **\***: p < 0.05 vs. Sham. **#**: p < 0.05 vs. 4pMI. Data are presented as mean ± SEM from the following number of cells per treatment group: Sham 23, 4pMI 19, 8pMI 19.

In summary, analysis of TT networks showed proliferative remodeling after MI characterized by a progressive increase of complexity and by the most pronounced increase of network length 4pMI. Regularity of TT alignment was lost post-MI as shown by a significant increase of oblique TT elements 4pMI and 8pMI. Most strikingly, the relative as well as the total amount of longitudinal TT elements was strongly increased 4pMI.

These results are contrary to the studies of Heinzel [88], Lyon [91] or Kemi [92] who observed a "loss of TTs" in failing cardiomyocytes from different species (Introduction 1.9.1). But these findings are in agreement with reports of TT disorganization [96, 97] (Introduction 1.9.2).

### 3.2.5 Remodeling of TT associated proteins

STED imaging of TTs in failing cardiomyocytes showed that TT remodeling after MI seems to be a proliferative mechanism. This finding gave rise to the hypothesis that proteins, which are thought to

play a role in the TT biogenesis like JPH2 and Cav3, might also be involved in TT remodeling during the development of HF (Introduction 1.7). In a rat model of increased pressure overload it has already been shown that JPH2 expression is reduced during the development of HF [97]. Increased Cav3 expression has been shown in a dog model of pacing-induced HF [125].

Expression levels of Cav3 and JPH2 in isolated Sham, 4pMI and 8pMI cardiomyocytes were determined by Western blot (Methods 2.10). Western blots were produced by Brigitte Korff (Dept. of Cardiology and Pulmonology, University Medical Center, Göttingen).
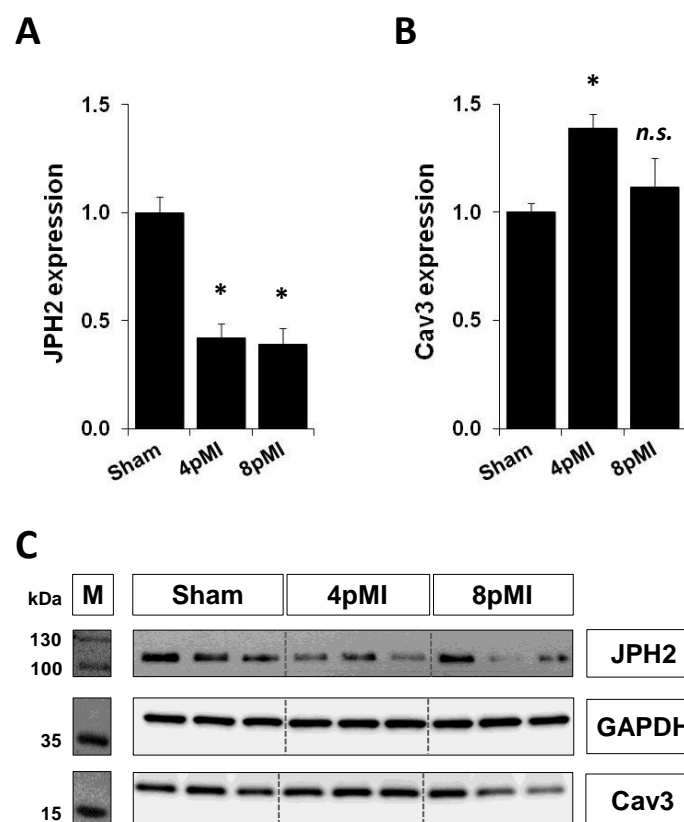


**Figure 3.19 Expression of JPH2 and Cav3 after MI.** Protein expression in cardiomyocytes was determined by Western blot. Values were normalized to the mean of Sham values. (**A**) Normalized JPH2 expression. (**B**) Normalized Cav3 expression. *n.s.*: not significant. **\***: $p < 0.001$ vs. Sham. Data are presented as mean ± SEM from 4 independent Western blots per protein with at least 3 samples per treatment group. (**C**) Exemplary Western blot images for JPH2, Cav3 and the reference protein GAPDH. Samples from 3 different mice per treatment group were applied. Boxes on the left side show the corresponding marker bands imaged by transmitted light. Sizes of the marker bands are given in kilodalton (kDa).

The results of Western blot analysis are shown in Figure 3.19. 4pMI the expression of Cav3 was increased 1.4-fold compared to Sham cardiomyocytes. 8pMI the Cav3 expression was almost unchanged compared to Sham. Analysis of the JPH2 Western blot data revealed a significant

decrease of protein expression 4pMI and 8pMI to approximately 40 % of the expression in Sham cardiomyocytes.

Besides expression levels, also the localization of Cav3 and JPH2 was analyzed and compared to the localization of RyR2. As part of the CRU, RyR2 is located in the SR membrane and shows a punctate pattern, regularly aligned along Z-lines. Figure 3.20 A compares the distribution of Cav3 and RyR2 signals in Sham and 4pMI cardiomyocytes. In the Sham example, Cav3 and RyR2 signals are regularly aligned along Z-lines. Both proteins show an alternating punctate pattern. In contrast, 4pMI numerous longitudinal Cav3 positive signals are visible.

A comparison of JPH2 and RyR2 signals in Sham and 8pMI cardiomyocytes is shown in Figure 3.20 B. In the Sham as well as in the 8pMI example, both proteins appear fully colocalized. While JPH2 and RyR2 show similar signal intensities in the Sham example indicated by yellow pixels, 8pMI the JPH2 signal decreases in relation to the RyR2 signal. Therefore, pixels appear greener 8pMI. This finding is consistent with the decreased expression of JPH2 8pMI as confirmed by Western blot (Figure 3.19). Furthermore 8pMI, RyR2 and JPH2 signals appear less regular than in Sham cardiomyocytes.

**A**
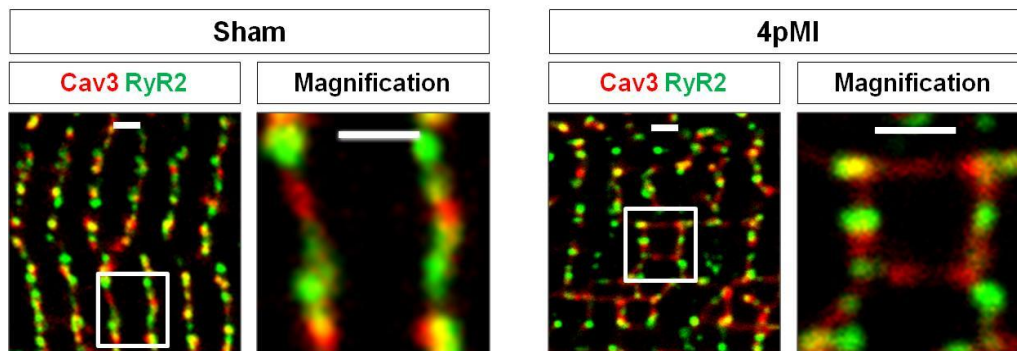


**B**
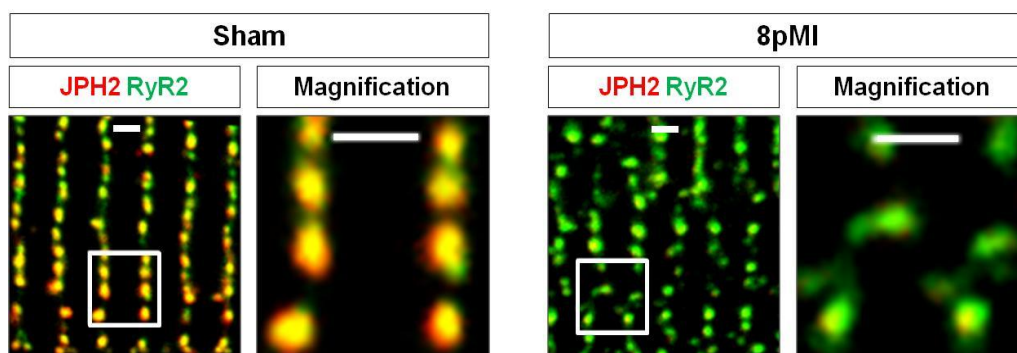


**Figure 3.20 Cav3, JPH2 and RyR2 immunostains in Sham and post-MI cardiomyocytes.** (*A*) Cav3 (red) and RyR2 (green) co-immunostains in Sham and 4pMI cardiomyocytes. (*B*) JPH2 (red) and RyR2 (green) co-immunostains in Sham and 8pMI cardiomyocytes. Scale bars (1 µm) represent the orientation of the longitudinal cell axis. White squares correspond to the magnifications. Overlapping red and green signals appear yellow.

Regularity of protein patterns was analyzed by Fourier transformation and analysis of the resulting power spectra (Methods 2.8.1). In the power spectrum analysis, the first periodic peak at ~0.5 µm$^{-1}$ corresponded to a spatial distance of 2 µm, the average Z-line spacing. So the regular distribution of one protein along Z-lines could be determined by measuring the amplitude of the first periodic peak. Figure 3.21 A summarizes the analysis of Cav3 power spectra in Sham and 4pMI cardiomyocytes. Compared to Sham, the Cav3 power spectrum is upward shifted 4pMI while the amplitude of the first peak is significantly decreased. These findings indicate increased heterogeneities between Z-lines – at frequencies different from 0.5 µm$^{-1}$ – and a decreased alignment of Cav3 at Z-lines. Decreased regularity 4pMI is also confirmed by a missing 2$^{nd}$ harmonic component, which is only present in the Sham power spectrum.

In Figure 3.21 B the same tendency is shown for the distribution of RyR2. The RyR2 power spectrum is also upward shifted 4pMI while the amplitude of the first peak is significantly decreased. This suggests a relative loss of RyR2 clusters at Z-lines accompanied by increased heterogeneities between Z-lines 4pMI.

JPH2 power spectra were analyzed for Sham and 8pMI cardiomyocytes. In contrast to Cav3 and RyR2, the JPH2 power spectrum is lower post-MI. Still the amplitude of the first peak is decreased 8pMI compared to Sham. As with Cav3 and RyR2, the 2nd harmonic component is only present in the Sham power spectrum.
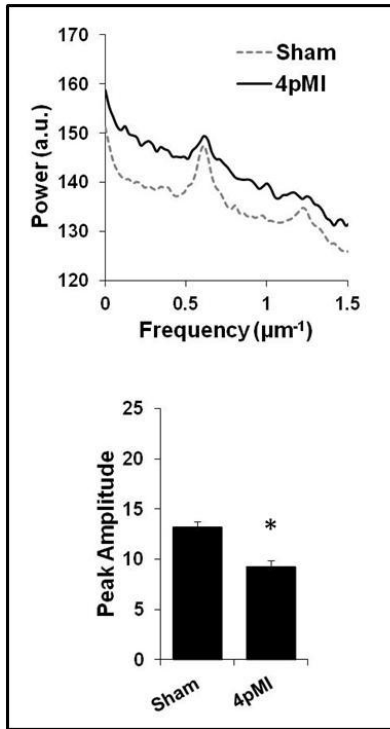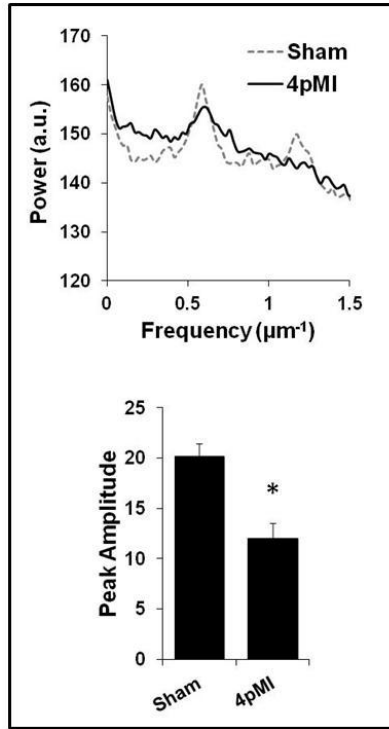
## A Cav3                          B RyR2                          C JPH2
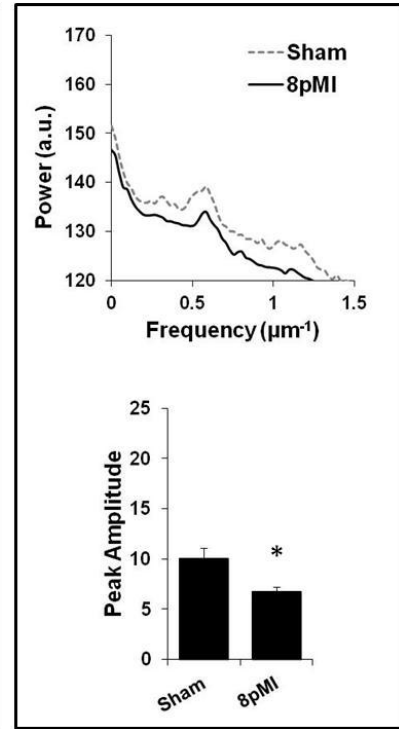


**Figure 3.21 Regularity of Cav3, RyR2 and JPH2 signals**. *Upper row:* Averaged profiles of power spectra as a function of the spatial frequency. The first peak at ~0.5 $\mu m^{-1}$ corresponds to the average Z-line spacing of 2 $\mu m$. The 2nd peak corresponds to the 2nd harmonic component. *Lower row:* Averaged amplitudes of the first peak at ~0.5 $\mu m^{-1}$. (*A*) Cav3 power spectra and peak amplitudes. (*B*) RyR2 power spectra and peak amplitudes. (*C*) JPH2 power spectra and peak amplitudes. **\***: $p < 0.05$ vs. Sham. Data are presented as mean $\pm$ SEM from the following number of images (cells): Cav3 Sham 9, Cav3 4pMI 6, RyR2 Sham 6, RyR2 4pMI 5, JPH2 Sham 9, JPH2 8pMI 11.

In summary, expression of JPH2 was significantly decreased 4pMI and 8pMI as confirmed by Western blot and immunofluorescence. While colocalization of JPH2 and RyR2 did not change post-MI, regularity in the alignment of both proteins along the Z-lines decreased. Expression of Cav3 was significantly increased 4pMI, but not 8pMI. Increased expression was accompanied by an increase of Cav3 positive longitudinal structures. The increased presence of Cav3 positive longitudinal structures 4pMI correlated with the already described strong increase of longitudinal TT elements 4pMI (3.2.4).

**3.2.6 Influence of longitudinal TT elements on Ca$^{2+}$ signaling**

To investigate the influence of different types of TT elements on Ca$^{2+}$ signaling, TT and Ca$^{2+}$ imaging were combined as previously described by Louch *et al.* [89]. Cardiomyocytes were stained with the membrane dye di-8-ANEPPS, loaded with the Ca$^{2+}$ indicator fluo-4/AM and imaged with a confocal microscope (Methods 2.3.2 and 2.6.3). Based on a two-dimensional di-8-ANEPPS image, either a transverse line or a longitudinal line was selected. Transverse lines (perpendicular to the major cell axis) cross longitudinal TT elements between Z-lines. Longitudinal lines (in parallel to the major cell axis) cross transverse TT elements at Z-lines. Cardiomyocytes were field-stimulated at 0.5 Hz and Ca$^{2+}$ transients were recorded along the selected scan lines.

Figure 3.22 shows examples of combined TT and Ca$^{2+}$ imaging in a Sham and a 4pMI cardiomyocyte. In Figure 3.22 A a transverse line scan was performed in a Sham cardiomyocyte with a regular TT network. This line crossed 4 independent longitudinal TT elements as illustrated by the di-8-ANEPPS line scan and its corresponding profile. The measured Ca$^{2+}$ transient along the same scan line showed an almost uniform onset which was confirmed by a low dyssynchrony index of 2.2 ms. The dyssynchrony index is determined as the standard deviation of the values for the earliest time at which $F_{50}$ was reached along the scan line. Less synchronous Ca$^{2+}$ transients would be expected to have a greater variation in time to reach $F_{50}$ (the half-maximal fluorescence of the entire spatially averaged line scan) at different points along the cell and would therefore yield a higher dyssynchrony index [89].

The 4pMI example in Figure 3.22 B exhibited a less regular TT network with more longitudinal TT elements than the Sham example. The selected scan line crossed at least 10 different longitudinal TT elements as illustrated by the di-8-ANEPPS line scan and its corresponding profile. At the same time a clearly dyssynchronous rise of local Ca$^{2+}$ along the scan line was observed. This missing synchrony is characterized by a high dyssynchrony index of 15.6 ms.

A direct correlation between a high number of longitudinal TT elements and a loss of synchrony in the onset of Ca$^{2+}$ transients was not proven. However, average dyssynchrony indices were largest in transverse line scans of 4pMI cardiomyocytes; the group with the highest proportion of longitudinal TT elements (as shown in 3.3.2). The average dyssynchrony index of 4pMI transverse line scans (crossing longitudinal TT elements) measured 6.7 ± 1.3 ms (n=11 cells) and was significantly larger (p < 0.01) than the average dyssynchrony index of Sham transverse line scans (2.5 ± 0.3 ms, n=4 cells). A reduced synchrony of Ca$^{2+}$ transients was also observed in longitudinal line scans (crossing transverse TT elements) of 4pMI cardiomyocytes. The average dyssynchrony index in longitudinal line scans measured 5.0 ± 1.5 ms (n=9 cells) in 4pMI and 2.2 ± 0.1 ms (n=4 cells) in Sham cardiomyocytes.

## A Sham
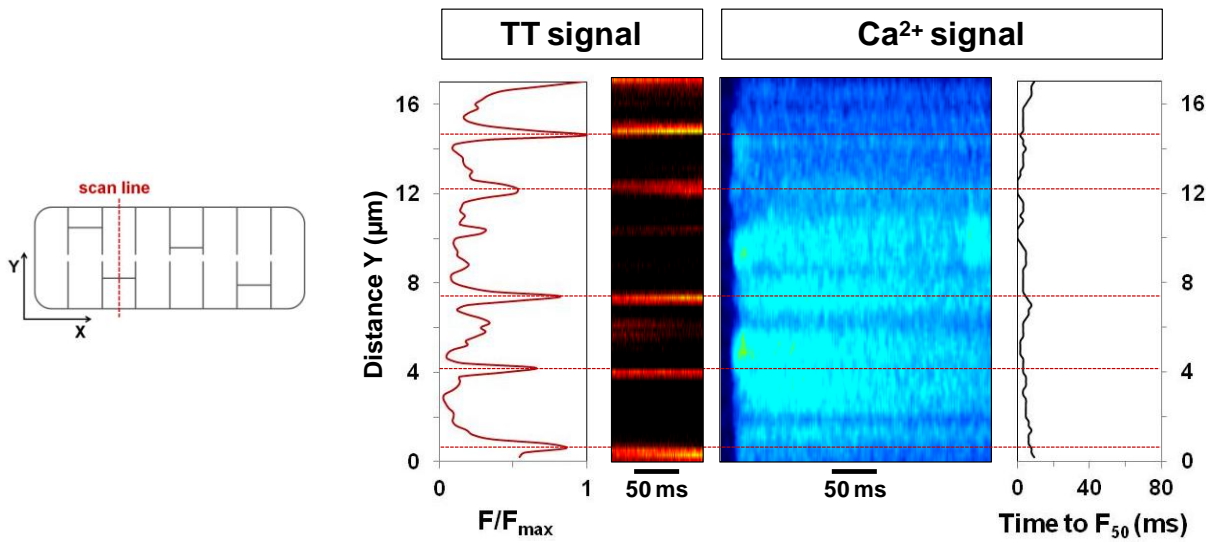


## B 4pMI
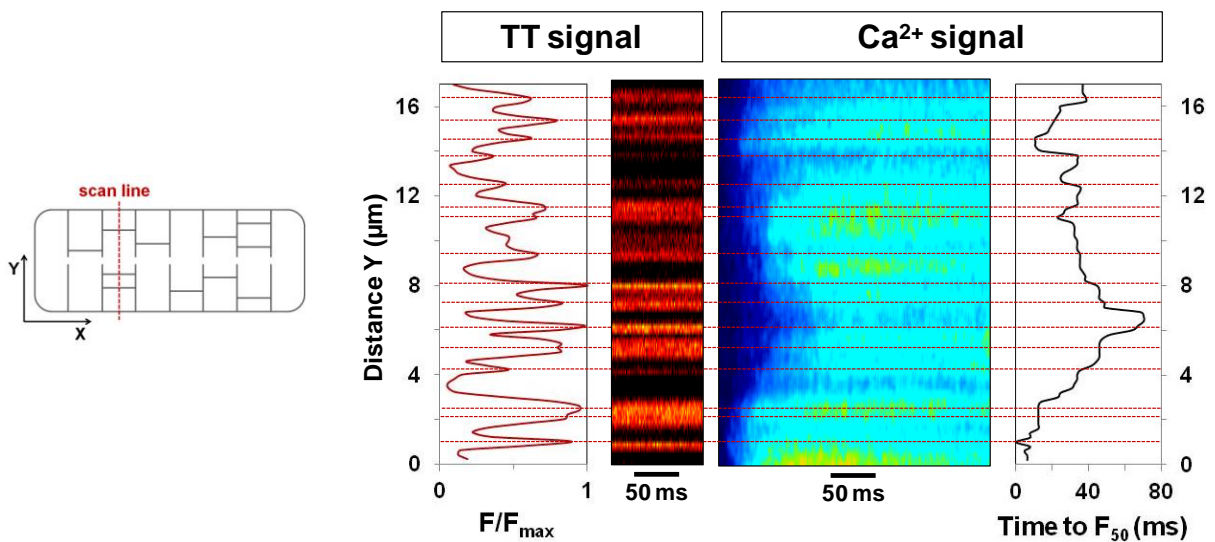


**Figure 2.22 Combined confocal TT and Ca$^{2+}$ imaging in Sham and 4pMI cardiomyocytes.** *Left*: Cartoon of a ventricular cardiomyocyte indicating the directions of the line scans on the right. *Right*: Normalized profile of the di-8-ANEPPS line scan image. Di-8-ANEPPS line scan. Fluo-4/AM line scan starting approximately 10 ms before one pacing pulse. Time to F$_{50}$ profile of the fluo-4/AM line scan image. (**A**) Transverse line scan in a Sham cardiomyocyte results in a low dyssynchrony index of 2.2 ms (**B**) Transverse line scan in a 4pMI cardiomyocyte results in a high dyssynchrony index of 15.6 ms.

**3.3 TT remodeling due to pressure overload**

**3.3.1 The TAC mouse model**

Transverse aortic constriction (TAC) is a commonly used experimental model to induce pressure overload (increased afterload) in mouse hearts. Initially, TAC leads to compensated hypertrophic remodeling of the heart. During later stages, maladaptative processes result in cardiac dilation and HF [116, 126, 127]. The TAC operations were performed by Julia H. Steinbrecher (Dept. of Cardiology and Pulmonology, University Medical Center, Göttingen). The pressure gradient at the site of the aortic constriction was determined by pulsed wave Doppler echocardiography three days after the intervention (for a detailed description please refer to 2.1.3, Methods). The average pressure gradient in TAC mice measured 85 ± 5 mmHg (mean ± SEM, n = 8 mice). As expected, in Sham mice the pressure gradient measured only 3 ± 0.2 mmHg (mean ± SEM, n = 8 mice). To investigate the influence of pressure overload on TTs, cardiomyocytes were isolated and analyzed either 4 weeks after TAC (4pTAC) or 8 weeks after TAC (8pTAC) and were compared to cardiomyocytes from Sham operated mice.

4pTAC and 8pTAC mice were characterized by echocardiography. Mouse echocardiography was performed by Kirsten Koschel (Dept. of Cardiology and Pulmonology, University Medical Center, Göttingen). LVID,d and EF determined by echocardiography are summarized in Figure 3.23 A and B. While diastolic LVID progressively increased after TAC, EF decreased indicating progressive cardiac dilation and loss of function after TAC.

HW/BW ratios determined directly before cardiomyocyte isolation progressively increased after TAC (Figure 3.23 C). An increased HW/BW ratio indicates hypertrophy. Hypertrophy was further examined by determining the sizes of isolated cardiomyocytes as described in Methods 2.6.2. Strongly increased cardiomyocyte cross-section areas particularly 8pTAC confirmed progressive hypertrophy after TAC (Figure 3.23 D).
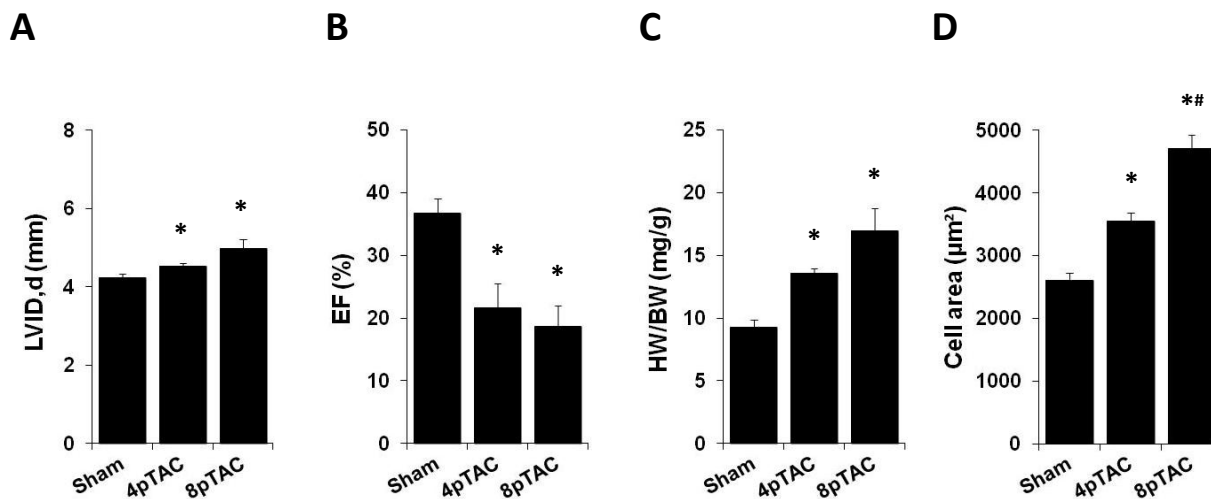
**Figure 3.23 Heart and cellular phenotype after TAC**. (*A*) Left ventricular inner diameter in diastole (LVID,d) determined by echocardiography. (*B*) Ejection fraction (EF) determined by echocardiography. (*C*) Heart weight to body weight ratio (HW/BW) determined directly before cardiomyocyte isolation. (*D*) Cardiomyocyte cross-section area. Data are presented as mean ± SEM from the following number of mice (cells): Sham 6 (45), 4pTAC 7 (45), 8pTAC 5 (45). *: $p < 0.05$ vs. Sham. #: $p < 0.05$ vs. 4pMI (unpaired T-test).

### 3.3.2 Remodeling of TT cross-sections after TAC

As already described for the analysis of TTs in healthy and post-MI cardiomyocytes, dimensions of TT cross-sections after TAC were determined by two different and independent methods. TT diameters and areas were determined by 2D Gauss fitting. TT circumferences were determined by contour analysis. Mean TT dimensions were determined separately in intracellular and submembrane images.

Table 3.4 summarizes the mean TT cross-section dimensions determined in intracellular images of Sham, 4pTAC and 8pTAC cardiomyocytes. While intracellular cross-section dimensions increased progressively after MI (+12 % 4pMI and +22 % 8pMI compared to Sham), TTs were enlarged 4pTAC but not 8pTAC. The intracellular TT cross-section area 4pTAC was enlarged by 17 %. 8pMI no changes were observed compared to Sham.

Dimensions of submembrane TT cross-sections are summarized in Table 3.5. Both 4pTAC and 8pTAC submembrane TT dimensions increased to the same extend. The mean TT cross-section area for example was almost 11 % larger in 4pTAC and 8pTAC submembrane images compared to Sham. Again, these findings differ from the observations made in the post-MI model where 4pMI TT dimensions were not changed in submembrane images. 8pMI submembrane TT cross-sections were enlarged by 15 %.

**Table 3.4 Intracellular TT cross-section dimensions are increased 4pTAC but not 8pTAC.** Dimensions of TT cross-sections were determined in intracellular STED images of Sham, 4pTAC and 8pTAC cardiomyocytes. Mean TT diameters and areas were determined by 2D Gauss fitting. Mean circumferences were determined by contour analysis. **\***: $p < 0.01$ vs. Sham. **#**: $p < 0.05$ vs. 4pTAC (unpaired T-test). Data are presented as mean ± SEM from the following numbers of TT cross-sections (cells) per treatment group: Sham 194 (43), 4pTAC 268 (51), 8pTAC 161 (41).

| Treatment group | Diameter X (nm) | Diameter Y (nm) | Area (nm$^2$) | Circumference (nm) |
| --- | --- | --- | --- | --- |
| Sham | 195.1 ± 3.0 | 185.5 ± 2.6 | 28,685.2 ± 682.1 | 653.2 ± 9.5 |
| 4pTAC | 208.3 ± 3.1 * | 202.2 ± 3.0 * | 33,648.8 ± 811.4 * | 721.4 ± 10.7 * |
| 8pTAC | 196.5 ± 3.7 # | 185.5 ± 3.2 # | 29,122.8 ± 870.4 # | 664.6 ± 12.0 # |

**Table 3.5 Submembrane TT cross-section dimensions are increased 4pTAC and 8pTAC.** Dimensions of TT cross-sections were determined in submembrane STED images of Sham, 4pTAC and 8pTAC cardiomyocytes. Mean TT diameters and areas were determined by 2D Gauss fitting. Mean circumferences were determined by contour analysis. **\***: $p < 0.01$ vs. Sham. *n.s.*: not significant. (unpaired T-test). Data are presented as mean ± SEM from the following numbers of TT cross-sections (cells) per treatment group: Sham 242 (52), 4pTAC 260 (56), 8pTAC 234 (50).

| Treatment group | Diameter X (nm) | Diameter Y (nm) | Area (nm$^2$) | Circumference (nm) |
| --- | --- | --- | --- | --- |
| Sham | 197.8 ± 2.5 | 183.9 ± 2.1 | 28,704.4 ± 515.3 | 651.0 ± 7.4 |
| 4pTAC | 199.0 ± 3.1 *n.s.* | 199.0 ± 3.0 * | 31,741.5 ± 830.2 * | 694.8 ± 10.5 * |
| 8pTAC | 199.5 ± 3.0 *n.s.* | 199.0 ± 3.4 * | 31,537.9 ± 817.2 * | 703.4 ± 11.8 * |

### 3.3.3 TT network remodeling after TAC

Like in post-MI cells, TT remodeling in cardiomyocytes from TAC mice was additionally investigated on the network level. As described before, skeletons were extracted from intracellular STED images of Sham, 4pTAC and 8pTAC TTs. The total TT network length and the number of triple junctions in a defined area were determined in order to quantify TT network complexity.

Figure 3.24 summarizes the changes observed in network length and complexity after TAC. While 8pTAC the parameters were almost comparable to the Sham group, 4pTAC both total network length and number of triple junctions were significantly increased. In contrast to these findings, in the post-MI model network complexity increased progressively.
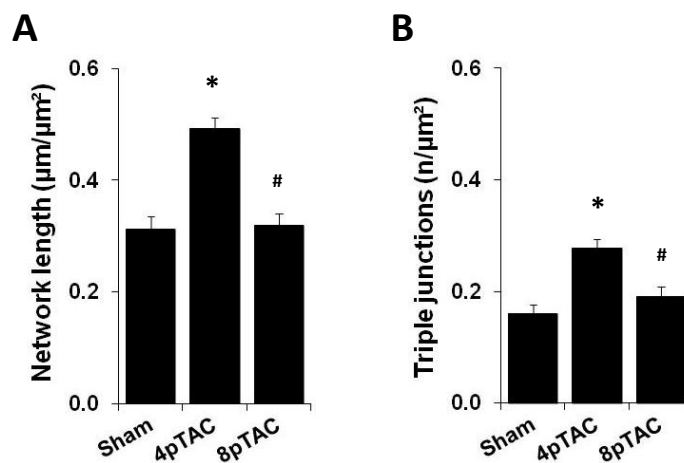
**Figure 3.24 TT network length and complexity increase 4pTAC.** The total network length per area and the number of triple junctions per area were determined in skeletonized STED images of Sham, 4pTAC and 8pTAC cardiomyocytes. (**A**) Total network length per area. (**B**) Number of triple junctions per area. **\***: p < 0.001 vs. Sham. **#**: p < 0.001 vs. 4pTAC Data are presented as mean ± SEM from the following number of cells per treatment group: Sham 36, 4pTAC 43, 8pTAC 43.

Finally, the amount of different TT components was analyzed in the TAC model. As described in 3.2.4, the total amount of transverse, longitudinal and oblique TT elements was determined in Sham, 4pTAC and 8pTAC cardiomyocytes. For that purpose, TT elements with an orientation of 90° ± 3° in relation to the longitudinal cell axis were defined as transverse. Elements with an orientation of 0° ± 3° were defined as longitudinal. And TT elements with an orientation of 45°± 3° or -45°± 3° were termed oblique.

Figure 3.25 A summarizes the total amount of different TT components for all treatment groups. As reference value for the calculations, the total network length described in Figure 3.24 was used. In Figure 3.25 B the relative proportion of each component is shown as percentage of the overall amount of TT elements. 4pTAC and 8pTAC, the relative amount of transverse TT elements decreased. The relative amount of longitudinal TTs increased 4pTAC while the relative amount of oblique TT elements remained almost unchanged after TAC. These observations were modified by calculating the total amount of the different TT components for each treatment group. Since the total TT network length which was highest 4pTAC was used as reference value for calculation, differential changes seen in total component length were different from the relative changes. Considering their total amount, transverse, longitudinal and oblique TT elements were increased 4pTAC but not 8pTAC. Nevertheless, the increase of longitudinal TT elements 4pTAC was the most prominent change.

**A**
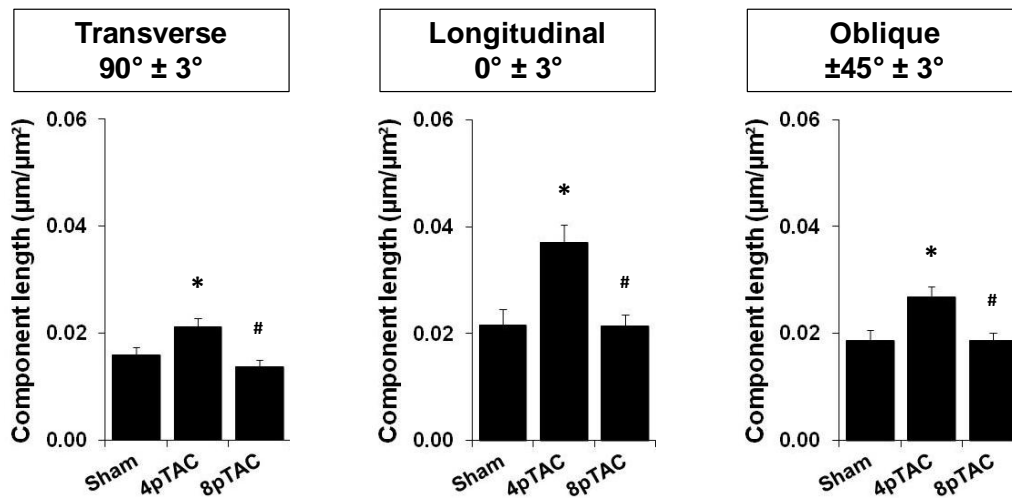


**B**
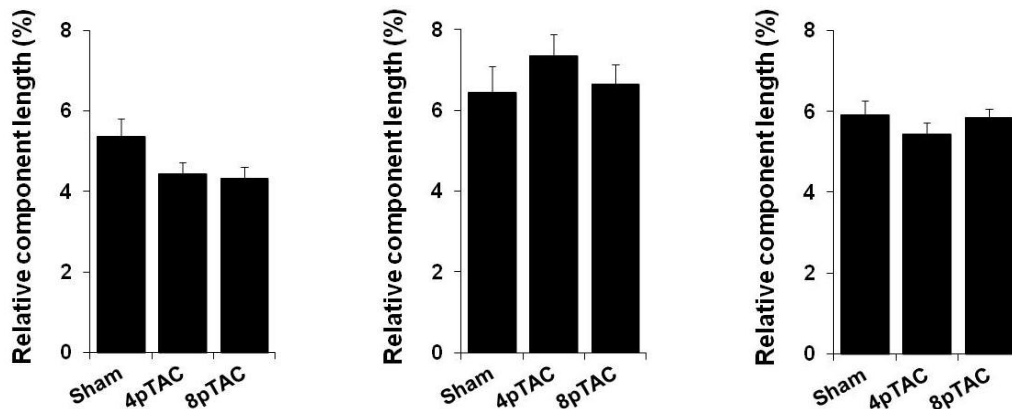


**Figure 3.25 Components of the TT network change differentially after TAC.** (**A**) Absolute amount of TT network components in Sham, 4pTAC and 8pTAC cardiomyocytes. **\***: $p < 0.05$ vs. Sham. **#**: $p < 0.05$ vs. 4pTAC. (**B**) Relative proportion of each component calculated as percentage of the overall amount of TT elements. None of the changes shown in (**B**) is statistically significant. Data are presented as mean ± SEM from the following number of cells per treatment group: Sham 36, 4pTAC 43, 8pTAC 43.

In summary, TT remodeling can also be observed during the development of HF after TAC. On the level of individual TT cross-sections as well as on the TT network level, remodeling seems to be more pronounced 4pTAC than 8pTAC. Dimensions of TT cross-sections are most strongly increased in intracellular images 4pTAC. This effect seems to be reversed during further progression of HF. Even the strong increase of TT network complexity and length observed 4pTAC is no longer apparent 8pTAC. These results differ from those observed in the post-MI model which showed progressive and proliferative TT remodeling.

**3.4 Three-dimensional STED imaging of TTs in healthy and post-MI cardiomyocytes**

As a further step towards understanding of the TT morphology in living healthy and diseased cardiomyocytes, STED imaging was performed 3-dimensionally (3D). For that purpose, the same ROI was imaged sequentially in different imaging depths. Using the "*3D Viewer*" plugin of the image processing program Fiji (*http://fiji.sc/*) [122], z-stacks were arranged with the appropriate z-distance and presented as 3D objects (Methods 2.9.3).

The reconstructed z-stack of one TT in a healthy cardiomyocyte in different views is shown in Figure 3.26. For that z-stack, the same ROI was imaged 19 times with a z-distance of 200 nm. The intracellular part of the reconstructed TT exhibited an evagination, which spanned several slices of the stack. In size and shape this evagination is reminiscent of a caveolus (for description of caveolae see Introduction 1.7).
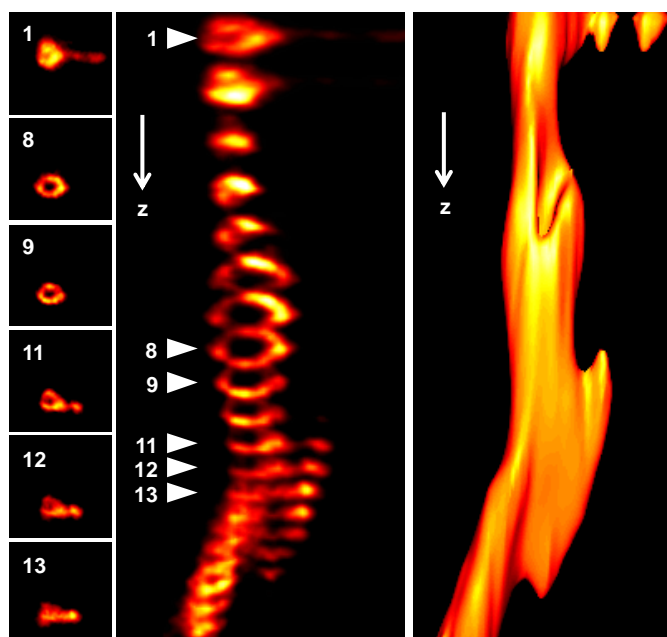


**Figure 3.26 Reconstructed z-stack of one TT in a healthy cardiomyocyte.** z-stack of 19 images with a z-distance of 200 nm. *Left*: Selected images of the same TT in different imaging depths. *Middle*: 3D "Volume" presentation of the reconstructed z-stack. Triangles mark the positions of the images on the left. *Right*: 3D "Surface" presentation of the reconstructed z-stack. Compared to the "Volume" presentation, this view has been slightly rotated. Arrows show from the cell surface towards the center.

TTs of post-MI cardiomyocytes were also 3D STED imaged. In Figure 3.27 3D surface reconstructions of Sham and 8pMI TTs are compared. Both examples show two neighboring TTs. The two TTs in the Sham example keep their distance of 2 μm, the regular Z-line spacing, along the entire z-stack. The

two TTs in the 8pMI example are not absolutely in parallel. They are connected through a continuous longitudinal TT element. TT junctions appear as strongly enlarged hollow structures.

**A**



**B**
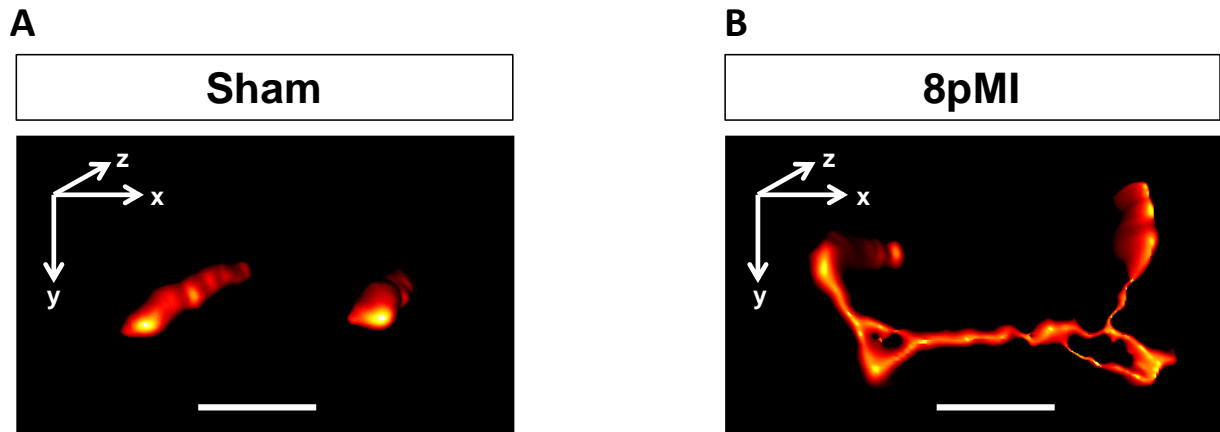


**Figure 3.27 3D reconstructions of TTs in Sham and 8pMI cardiomyocytes**. (**A**) "Surface" presentation of two parallel TTs in a Sham cardiomyocyte. TTs are 2 μm apart from each other, the regular Z-line spacing. (**B**) "Surface" presentation of two neighboring TTs in an 8pMI cardiomyocyte, connected through a longitudinal TT element. Junctions appear strongly enlarged. Both 3D reconstructions represent 7 images with a z-distance of 300 nm. Scale bars (1 μm) represent the orientation of the longitudinal cell axis.

In summary, 3D STED imaging provides further information on the morphology of TTs in healthy and diseased hearts. The same TT can be tracked over several micrometers inside the cell, substructures like potential caveolae can be observed in successive slices and TT elements can be spatially assigned to the junctions they lead to.

## 4 Discussion

### 4.1 Brief summary of the results

In this thesis, STED microscopy was used for the non-invasive super-resolution imaging of intact TT membranes deep inside living cardiomyocytes. Novel quantitative image analysis strategies were developed to investigate the TT morphology in healthy and diseased cardiomyocytes. Two different mouse disease models (MI and TAC) were employed to examine the intervention-dependent TT remodeling over time during the development of HF.

The major TT changes detected in the post-MI model were (1) a progressive and heterogeneous enlargement of intracellular and submembrane TT cross-sections and (2) proliferative TT network remodeling, particularly characterized by a significant increase of longitudinal TT elements 4pMI. These changes were accompanied by a progressive decrease in JPH2 expression and an increased expression of Cav3 4pMI. Additionally, the increased number of longitudinal TT elements 4pMI seemed to influence $Ca^{2+}$ transients. In the TAC model, intracellular TT cross-sections were selectively enlarged four but not eight weeks after the intervention, whereas submembrane cross-section dimensions were increased 4pTAC and 8pTAC. TT network length and complexity were only increased 4pTAC. The major quantitative findings concerning TT remodeling after MI and TAC are summarized in Table 4.1 below.

**Table 4.1 Quantitative changes of TT properties after MI and TAC.** Data are presented as mean values (the complete datasets and numbers of analyzed TT cross-sections and networks are given in Tables 3.2 – 3.5 and Figures 3.16 and 3.24 in the Results section). **\***: $p < 0.05$ versus the corresponding Sham group. *n.s.*: not significantly changed compared to the corresponding Sham group.

| MI model | | 4pMI | 8pMI |
|---|---|---|---|
| **TT cross-section area** | intracellular | 34,354 nm$^2$ **\*** | 37,292 nm$^2$ **\*** |
| | submembrane | 29,853 nm$^2$ *n.s.* | 35,099 nm$^2$ **\*** |
| **TT network length** | | 0.52 µm/µm$^2$ **\*** | 0.50 µm/µm$^2$ **\*** |
| **Triple junctions** | | 0.33 /µm$^2$ **\*** | 0.38 /µm$^2$ **\*** |

| TAC model | | 4pTAC | 8pTAC |
|---|---|---|---|
| **TT cross-section area** | intracellular | 33,649 nm$^2$ **\*** | 29,123 nm$^2$ *n.s.* |
| | submembrane | 31,742 nm$^2$ **\*** | 31,538 nm$^2$ **\*** |
| **TT network length** | | 0.49 µm/µm$^2$ **\*** | 0.32 µm/µm$^2$ *n.s.* |
| **Triple junctions** | | 0.28 /µm$^2$ **\*** | 0.19 /µm$^2$ *n.s.* |

**4.2 STED microscopy for the investigation of TT membranes in living cardiomyocytes**

Previous studies provided important insight about the structure of the TT system in different species (e.g [1]). Nevertheless, due to methodological limitations, individual TT elements have so far not been resolved in living cardiomyocytes, particularly not in species with small TT diameters like mouse. For rabbit TTs, Savio-Galimberti *et al.* estimated an average diameter of 448 ± 172 nm based on diffraction limited confocal images [128]. Still, no individual tubular structures were resolved. Particularly with regard to the investigation of transgenic mouse models, the analysis of murine TTs becomes increasingly important. Since it is assumed that mouse TT diameters are much smaller than those in rabbits, super-resolution techniques are needed to resolve their dimensions and nanostructure [129].

Microscopy techniques that overcome the resolution limit of conventional light microscopy by at least a factor of two are considered as super-resolution techniques [130]. As already mentioned in the introduction, EM is not applicable to living samples and is usually restricted to one imaging plane. Furthermore, it has been shown that different methods of sample preparation for EM can lead to variable results concerning dimensions of TTs (e.g. a fourfold difference in TT volume fraction [8]). Therefore, super-resolution light microscopy techniques offer significant advantages for the investigation of TT membranes in living cardiomyocytes. Besides STED microscopy, other super-resolution techniques were considered, for example *stochastic optical reconstruction microscopy* (STORM [131]), *photoactivated localization microscopy* (PALM [132]) or *fluorescence photoactivation localization microscopy* (FPALM [133]). STORM, PALM and FPALM use a stochastic readout instead of the targeted readout that is known from STED microscopy [109]. For the stochastic readout, fluorescent molecules are switched on and off randomly in space by photomodulation and are localized individually. After repeated signal detection from different random subsets of individual fluorophores, individual fluorophore positions are determined. The coordinates of all localized fluorophores are used to mathematically reconstruct an image. The main weaknesses of these methods are the relatively slow image acquisition and the required extensive data postprocessing [134].

Using STED microscopy, long image acquisition times and extensive image processing could be avoided. Short image acquisition times are particularly advantageous for delicate living samples. Furthermore, after careful selection and testing, di-8-ANEPPS, an established dye for imaging of membranes in living cardiomyocytes [24, 88, 89, 96, 135] could be used for STED microscopy. It is conceivable that a diffusible membrane dye like di-8-ANEPPS might encounter limitations for a stochastic readout imaging approach. As a major advantage, STED images can be directly compared to confocal images of the same ROI and differences can be quantified. A direct quantitative

comparison of STED and confocal images helps to explain possible differences between the newly obtained results from STED images and previously published data obtained from confocal images of TTs stained with the same dye (see next chapter).

### 4.2.1 Exploiting the properties of di-8-ANEPPS for STED imaging of TT membranes

ANEP (aminonaphtylethenylpyridinium) dyes have originally been developed by Leslie Loew and colleagues. Among those, di-8-ANEPPS belongs to the structural class of styryl dyes [136, 137]. These are amphiphilic membrane dyes containing both a lipophilic part acting as membrane anchor and a hydrophilic part which aligns the chromophore perpendicular to the membrane bilayer [124, 138]. In the case of di-8-ANEPPS a pair of octyl hydrocarbon chains (8 carbons) anchors the dye in the outer leaflet of the membrane bilayer [139, 140]. The alkyl chains are attached to the amino group of the ANEP chromophore. A propylsulfonate (PS) head group assures the orientation perpendicular to the membrane [138, 141]. The structure of di-8-ANEPPS and its alignment with the membrane bilayer are illustrated in Figure 4.1.



**A**

$^-O_3S(CH_2)_3{}^+N$ ⟷ $CH = CH$ ⟷ $N[(CH_2)_7CH_3]_2$

**Hydrophilic Group**
*propylsulfonate* (*PS*)
→ alignment perpendicular
to the membrane

**Chromophore**
*aminonaphthylethenylpyridinium*
(*ANEP*)

**2 Alkyl Chains**
(*8 carbons*)
→ membrane anchors

**B**

outer leaflet    inner leaflet

cellular    extra    intracellular
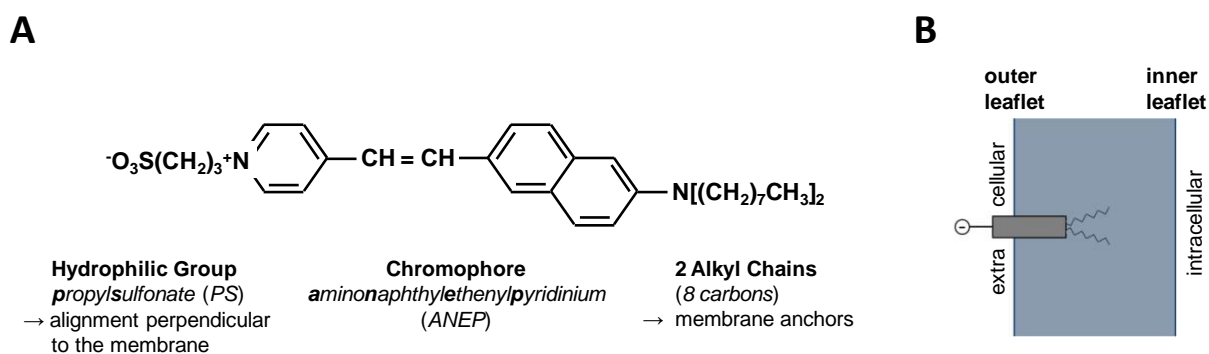
**Figure 4.1 Structure and membrane alignment of di-8-ANEPPS.** (*A*) Structure of the amphiphilic di-8-ANEPPS molecule. (*B*) Cartoon indicating the membrane alignment of di-8-ANEPPS. If the dye solution is applied extracellularly, the octyl hydrocarbon chains anchor di-8-ANEPPS in the outer leaflet of the membrane bilayer.

In the context of STED imaging, the membrane visualization is expected to benefit from the perpendicular orientation of di-8-ANEPPS relative to the membrane. Volker Westphal (Dept. of NanoBiophotonics, MPI for Biophysical Chemistry, Göttingen) kindly supported mathematical modeling of the influence of dye orientation on the probability to resolve a TT which is in parallel to the imaging plane (e.g. the exemplary TT element shown in Figure 4.2 B). The model used a virtual regular cylindrical TT with variable radii. Fluorescence intensity was calculated along a simulated scan line through the center of this TT, considering the known PSFs for excitation and STED laser beams

(radius excitation PSF: 130 nm, radius STED PSF: 300 nm, dimensions of both PSFs in z: 350 nm). A threefold increase of resolution was assumed for STED imaging compared to regular confocal imaging ($\sqrt{(\frac{ISTED}{Isat})}$ = 3).

The interaction between a light wave with a circular polarization and the molecular dipole of a fluorophore goes with $\cos^2(\alpha)$, with $\alpha$ being the angle between polarization and the molecular dipole of the fluorophore. The same relation holds for the detection probability, therefore the total brightness of a molecule with circular excitation and unpolarized detection depends on $\cos^4(\alpha)$. This means that maximal fluorescence occurs when molecular dipole and polarization are in parallel to each other ($\cos^4(0°)$ = 1, dye molecule exactly perpendicular to the optical axis). No fluorescence occurs, if they are perpendicular to each other ($\cos^4(90°)$ = 0, dye molecule in parallel to the optical axis). Similar to above, the interaction between the STED light and the dipole (and hence the STED efficiency) depends on the orientation of the dye molecule by $\cos^2(\alpha)$ [142, 143].

The mathematical modeling performed here included (1) the calculation of fluorescence intensity along the virtual scan line considering dye orientation, thus including the factors $\cos^4(\alpha)$ for fluorescence intensity and $\cos^2(\alpha)$ for STED efficiency (solid lines in Figure 4.2 D – F) and (2) the same calculations only without consideration of the dye orientation and thus without inclusion of the angle-dependent factors (dashed lines in Figure 4.2 D – F).

Figure 4.2 summarizes exemplary calculations performed for virtual TTs with different radii (50 nm, 100 nm, 200 nm). Furthermore, in Figure 4.2 D it was assumed that all dye molecules are invariably aligned perpendicular to the TT membrane (solid lines). In Figure 4.2 E it was calculated, how a variability of 25° in this perpendicular alignment would influence resolution of the hollow TT structure. In Figure 4.2 F a variability of 50° in the perpendicular alignment was assumed. All virtual line scans that considered dye orientation were compared to those, which did not consider dye orientation (dashed lines).

**Figure 4.2 Influence of dye orientation on the STED image of a transverse TT element.** (**A**) Simulated TT element with a variable radius. STED imaging was simulated along the x–axis through the center of the TT. (**B**) STED image of a TT element in the imaging plane and the measured line profile along the x-axis. White line marks the position of the line profile. (**C**) Exemplary simulated line profile through a virtual TT. This example illustrates how contrast is defined (**D**) – (**F**): Simulated line profiles representing fluorescence intensity in an optical section of a virtual TT element with different radii and graph showing the dependence of the contrast on the TT radius. The contrast was calculated as the normalized difference between the signal in the center (x = 0 nm) and the maximal intensity. Simulations were performed by Volker Westphal (Dept. of NanoBiophotonics, MPI for Biophysical Chemistry, Göttingen).

**A**

TT
model

**B**

TT in the
imaging plane

y

x

measured
line profile

**C**

simulated
line profile

contrast
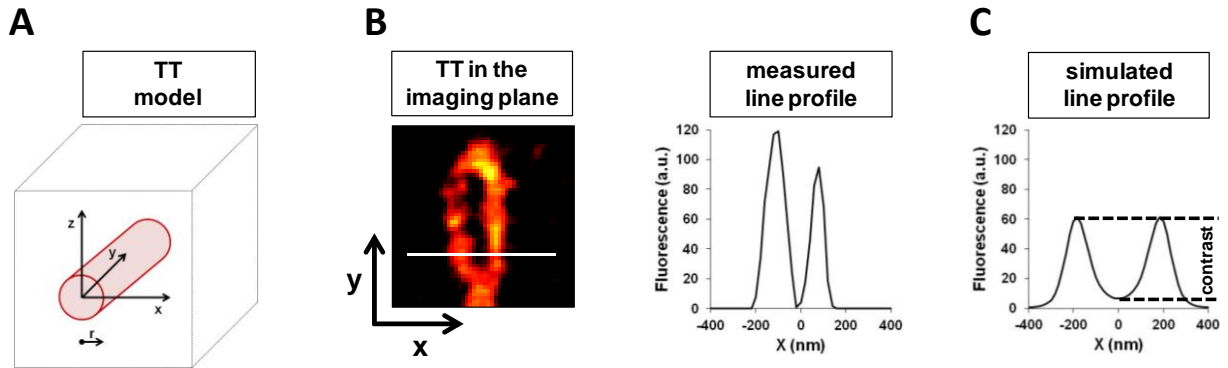
dye molecules perpendicular to the
TT membrane with a variability of
(*D*) 0°, (*E*) 25° or (*F*) 50°

- - - - - dye orientation
not considered

**D** dye molecules perpendicular to the TT membrane (no variability)

TT radius 50 nm

TT radius 100 nm

TT radius 200 nm

Contrast

**E** dye molecules perpendicular to the TT membrane with a variability of 25°

TT radius 50 nm

TT radius 100 nm

TT radius 200 nm

Contrast

**F** dye molecules perpendicular to the TT membrane with a variability of 50°

TT radius 50 nm

TT radius 100 nm

TT radius 200 nm

Contrast

Figure 4.2 shows that TTs with a radius of 50 nm or 100 nm which are in parallel to the imaging plane cannot be resolved as hollow structures if the dye is not oriented perpendicular to the membrane (gray dashed lines in (D) – (F)). For TTs with a radius of 200 nm, the underlying hollow structure becomes apparent as shown by two visible peaks and the calculated contrast of 0.35 between the fluorescence in the center of the TT (x = 0 nm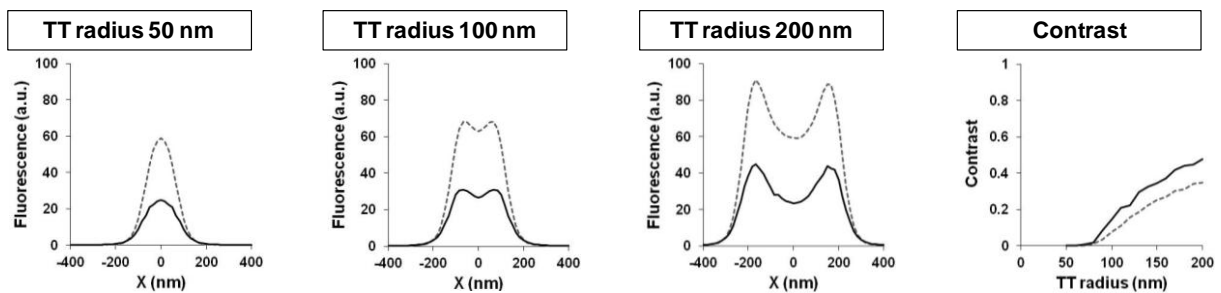) and the maximal fluorescence intensity on the scan line (1 represents a maximal contrast, 0 represents no contrast and thereby no resolution of the hollow structure).

In case all dye molecules are invariably aligned perpendicular to the TT membrane, TTs with a radius of 100 nm can be resolved (contrast 0.55, Figure 4.2 D). TTs with a radius of only 50 nm cannot be resolved, even with ideally aligned dye molecules under the assumed conditions with a threefold resolution improvement compared to confocal imaging ($\sqrt{(\frac{ISTED}{Isat})} = 3$). The contrast between TT membrane and TT center becomes worse with increasing variability of the dye orientation. A variability of 25° (Figure 4.2 E) still allows seeing the tubular structure of a TT with a radius of 100 nm (contrast 0.42). With a variability of 50° (Figure 4.2 F) only larger TTs can be resolved as hollow structures (contrast for a TT with a radius of 200 nm: 0.48).

This mathematical simulation shows that the properties of di-8-ANEPPS optimally contribute to the ability to resolve individual TTs structures using STED microscopy. Besides that beneficial effect, staining of cardiomyocytes with di-8-ANEPPS did not result in formation of membrane blebs, aberrant contractions, cell death or detectable dye internalization as it was clearly the case for the other tested dyes (Chapter 3.1, Results).

In summary, it was shown that STED super-resolution imaging of intact TTs in living cardiomyocytes is not necessarily limited by imaging depth. Even 3D STED imaging of TTs was realized in healthy and diseased cardiomyocytes. Under the given conditions, a resolution of 50 – 60 nm could be obtained. Furthermore, resolution was sufficient to determine the dimensions of individual TT elements with an average diameter of ~200 nm. TT substructures with dimensions smaller than 100 nm, particularly caveolae, could not be resolved in detail. However, the presence of TT membrane evaginations which might represent caveolae could be visualized (Figure 3.26, Results). The approximately 3.5-fold resolution improvement we obtained relative to confocal imaging enabled the detection of subtle changes in the TT architecture that would otherwise have remained unrecognized.

**4.3 MI and TAC as models for progressive cardiac remodeling**

MI due to ligation of the LAD coronary artery and increased afterload due to TAC are the most widely studied rodent models of HF development [144]. An important advantage is that these models are reproducible and that HF development is therefore to some degree predictable.

LAD coronary artery ligation has first been described in rat (1960, [145]). With the advent of transgenic mouse models, the MI surgery technique was successfully conducted in mice (1978, [146]). LAD ligation leads to necrosis of the myocardium which is usually perfused by the LAD due to the acute loss of metabolic supply. After the initial necrosis and healing processes, the infarct degrades into scar tissue over weeks. As a compensatory response, the surviving myocardium undergoes hypertrophic adaptation and ultimately the left ventricle dilates. Over a period of weeks to months and dependent on the infarct size, the heart function becomes progressively impaired as the acute compensatory response (e.g. hormonal stimulation) cannot overcome the loss of cardiac tissue [147]. Alterations in cardiac structure and function after coronary ligation in mice resemble important pathophysiologic milestones in human ischemic heart disease [148]. In humans, acute MI and the consequent loss of contractile myocardium are a very frequent cause of chronic HF [147].

The second model, constriction of the transverse aorta in mice to induce cardiac hypertrophy, has first been described in 1991 [126]. Left ventricular hypertrophy develops rapidly after TAC and the initially impaired left ventricular function is compensated over the first two weeks, indicating a powerful compensatory response to pressure overload [149, 150]. However, over time this response becomes maladaptive, ultimately resulting in a phenotype of left ventricular dilation and HF [116, 151]. While constriction of the aorta somewhat resembles an aortic stenosis in humans, it is important to state that the acute onset of a severe pressure overload (~80 mmHg) lacks direct clinical relevance [152].

Mirotsou *et al*. conducted one of the very rare studies which directly compared the MI and the TAC model [153]. They compared gene expression profiles of mice one week after MI or TAC and hypothesized that several genes would exhibit differential expression patterns in both models, which might play a causal role in the hypertrophic response. Indeed, in both models they identified gene expression changes that have previously been reported to be associated with hypertrophic remodeling, like atrial natriuretic peptide (ANP), brain natriuretic peptide (BNP), actin and collagen [153].

For this study, it has to be considered that the MI model might reflect a phenotype that is more closely related to human ischemic heart disease, whereas the artificial TAC model allows the investigation of changes due to a rapid onset of maladaptive hypertrophic remodeling. It is possible

that intervention-induced TT changes might occur earlier during HF development in the TAC than in the MI model.

## 4.4 A comparison of the present results with previous studies

As already outlined in the introduction, previous results concerning remodeling of TT structures in HF are variable and sometimes even contradictory. Only few studies investigated early TT changes in mice after MI and super-resolution imaging of TTs has so far only been performed by EM of extensively treated, fixed samples. Furthermore, TT studies in human samples have been limited to singular examples or samples from explanted hearts representing end-stage HF [91, 154-156].

In 1975, Maron *et al.* imaged left ventricular biopsies from human patients with different cardiac pathologies by EM [157]. This study differentiated between mildly altered cells which showed proliferation of TTs and moderately and severely degenerated cells which showed a loss of TTs. The cellular phenotype appeared dependent on the severity of the disease [157]. Furthermore, Wei *et al.* showed a significant correlation between a decreasing TT power (a measure for regular alignment with Z-line striations based on Fourier transformation) and left ventricular function in a rat TAC model [97].

Based on the newly obtained results and with regard to previous studies, I suggest a model which includes the different aspects of TT remodeling during development of HF as summarized in Figure 4.3. The early phase includes an increase of intracellular TT dimensions along with an increase of TT network length and complexity. This early phase of intracellular remodeling is followed by an increase of submembrane TT dimensions. The initial remodeling processes might represent a compensatory mechanism in order to preserve the surface to volume ratio in hypertrophied cardiomyocytes. During later stages of HF, this compensatory mechanism appears to fail, as evidenced by a relative reduction of the TT system compared to an increased cell size.

As described in the previous chapter, intervention-induced TT changes are likely to occur earlier in the TAC than in the MI model. This idea is supported by the findings in this thesis. In the MI model, a progressive increase of intracellular TT dimensions as well as of TT network length and complexity were observed in the first eight weeks after the intervention. An increase of submembrane TT dimensions was not observed until 8pMI. In the TAC model, an increase of intracellular TT dimensions, network length and complexity were only observed within the initial four weeks after the intervention. 8pTAC no significant increase of intracellular TT dimensions, TT network length and complexity were detectable. Instead, increased submembrane TT dimensions were observed 4pTAC

and 8pTAC. The quantitative changes of TT properties after MI and TAC mentioned here are summarized in Table 4.1 (Chapter 4.1).

To sum up, the present results suggest that the different stages of TT remodeling are reached earlier after the TAC intervention than after MI. In order to confirm differences in the time-dependent reorganization of TT elements after the different interventions, it would be necessary to investigate an even earlier time-point after the TAC intervention (e.g. 1pTAC) and a later time-point after MI (e.g. 12pMI).
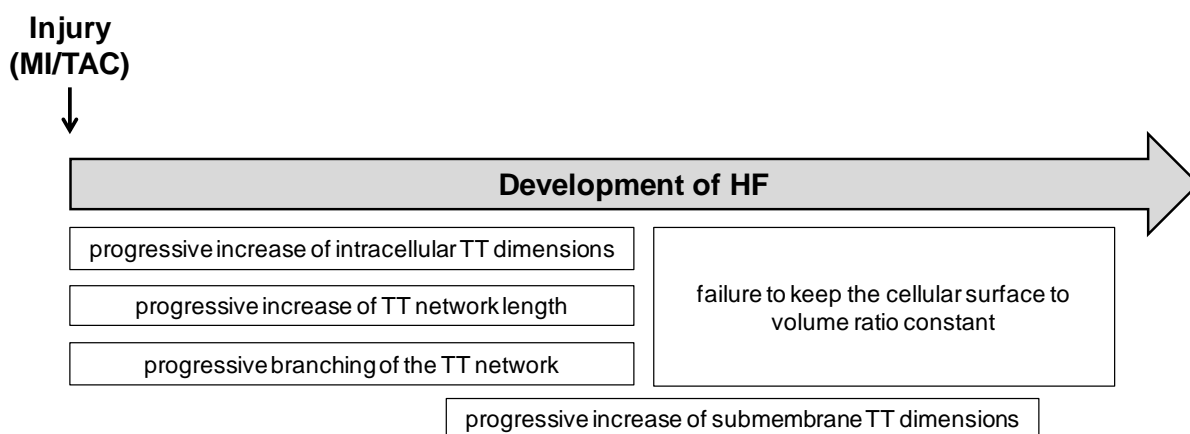


**Figure 4.3 Suggested time course of TT remodeling during the development of HF.** Initially, remodeling of intracellular TTs occurs. Dimensions of individual TTs as well as TT network length and complexity increase. Later during the development of HF, also the dimensions of submembrane TTs increase. Finally, these membrane-additive mechanisms are stopped or even reversed.

Louch *et al.* conducted a TT study on isolated mouse cardiomyocytes after MI applying confocal microscopy [89]. They imaged TTs in living di-8-ANEPPS stained cells and reported a progressive TT disorganization in the first three weeks after the intervention. This observation fits into the suggested time course of TT remodeling during the development of HF. Nevertheless, the study by Louch *et al.* was limited by the use of a conventional confocal microscope (LSM510, Carl Zeiss with a 40x objective) that did not allow a detailed description of TT changes. Furthermore, image analysis was restricted to a categorization of TT structures by eye as "organized, somewhat disorganized and markedly disorganized" [89].

Lyon *et al.* reported a "loss of TTs" in isolated rat cardiomyocytes 16 weeks after MI and in end-stage failing human cardiomyocytes [91]. Since these observations correspond to late time-points during HF development, they are not immediately relevant to the earlier observations reported here.

In summary, the TT remodeling processes observed in this study applying STED microscopy in cardiomyocytes from two different disease models significantly extend already existing studies.

Furthermore, for the first time significant disease-related changes at the nanometric scale are quantified in living cardiomyocytes. These observations justify a reinterpretation of earlier TT studies in different disease models which did not identify proliferative or differential changes.

## 4.5 Potential consequences of proliferative membrane remodeling

In 1973, Page and McCallister hypothesized that an addition of TT membranes may compensate for a decrease in the surface to volume ratio of enlarged cells during hypertrophy. They speculated that an extreme degree of myocardial hypertrophy might lead to a failure to maintain the total surface to volume ratio of the cell. Furthermore, essential metabolic functions which depend on the plasma membrane might break down and contribute to the critical transition from myocardial hypertrophy to HF [40].

Both the documented proliferative (additive) TT network remodeling and increased TT dimensions indicate mechanisms which may contribute to an increased cardiomyocyte surface. On the one hand, a constant surface to volume ratio might sustain nutrient supply to a large hypertrophied cell. On the other hand, additional TT membranes might propagate APs throughout the hypertrophied cell and ensure a spatially and temporally synchronous $Ca^{2+}$ release.

### 4.5.1 Increased dimensions of individual TTs

Increased TT sizes in HF have been occasionally described as accidental findings. In an EM image of a fixed explanted heart sample from a patient with end-stage dilated cardiomyopathy, enlarged TTs were observed [158]. With the same method, Maron *et al.* reported irregularly shaped and occasionally enlarged TTs in human hypertrophied cardiomyocytes [157]. Also using EM for the investigation of cardiomyocytes from end-stage HF patients, Crossman *et al.* described enlarged peripheral TTs [155]. However, the potential consequences of TT enlargement were not considered. Furthermore, data from human samples were typically derived from explanted hearts of end-stage HF patients. Therefore, these samples were additionally exposed to invasive protocols of surgical organ handling, prior to preparation of EM slices and histochemical fixation.

Savio-Galimberti *et al.* discussed the physiological meaning of the TT diameter in healthy cardiomyocytes. They speculated that variations in TT diameter might contribute to the supply of nutrients and $Ca^{2+}$ ions for cell signaling. Furthermore, they assumed that during cardiomyocyte

contraction and relaxation the TT might be squeezed and the compartmentalized extracellular fluid would be pumped in and out of the TT system to accelerate and augment diffusional transport [128].

Shorten *et al*. constructed a mathematical model of insulin transport within the TT network of frog skeletal muscle fibers [159]. With a diameter of ~18 nm, frog skeletal TTs are much smaller than TTs in murine cardiomyocytes [160, 161]. Shorten *et al.* calculated that the small diameter has a significant effect on insulin diffusion within the TTs. In addition, they suggested that insulin diffusion is faster in muscle fibers whose TT system is less tortuous. Considering additional factors like insulin binding to insulin receptors, interstitial fluid viscosity and hydrodynamic wall effects, the model predicted that, depending on the fiber type, there is a 2 to 15 min delay in the arrival time after insulin injection between the surface sarcolemma and inner TTs (located 20 µm from the surface sarcolemma). Therefore, Shorten *et al*. stated that the dense TT network with small diameters in frog skeletal muscle impedes insulin transport into the TTs and consequently delays the glucose uptake by the muscle cells [159]. These findings confirm the relevance of the TT network properties with regard to glucose uptake and nutrient supply in general.

Whether in turn the increased TT dimensions observed in this study improve and accelerate the cellular nutrient supply, needs to be further investigated. Computational modeling of TTs with varying diameters might support the understanding of a potential influence of TT dimensions on nutrient exchange.

## 4.5.2 Increased amount of longitudinal TTs 4pMI

Several studies have shown that regions devoid of TTs may exhibit irregular $Ca^{2+}$ transients [88-90]. However, it is unclear if the amount of TT membranes correlates with $Ca^{2+}$ release synchrony. In healthy rat cardiomyocytes, Asghari *et al.* showed that longitudinal ("axial") TTs form junctions with the SR. RyR2 channels on axial junctions colocalized with $Ca_V1.2$, suggesting that these junctions play a functional role in E-C coupling [162].

Strikingly, in this study the number of longitudinal TT elements was significantly increased 4pMI suggesting a potential functional role. To investigate the potential influence of the increased number of longitudinal TTs on $Ca^{2+}$ signaling, TT and $Ca^{2+}$ imaging were combined (for the detailed protocol please refer to 2.6.3, Methods). Indeed, the increased number of longitudinal TT elements 4pMI correlated with a significant decrease of $Ca^{2+}$ release synchrony (Figure 2.22, Results). In contrast, healthy cardiomyocytes showed fewer longitudinal TT elements which did not seem to influence $Ca^{2+}$ release synchrony. Despite the heterogeneous onset of $Ca^{2+}$ release in 4pMI cardiomyocytes, not

every longitudinal TT element appeared to colocalize with a region of delayed $Ca^{2+}$ release. Therefore, I conclude that the approximately twofold increase of longitudinal TT elements 4pMI might represent a partial attempt to ensure $Ca^{2+}$ release synchrony. However, the profound TT reorganization may lead to a disruption of functional CRUs. A dysfunction of individual CRUs can be further explained by a significant reduction of JPH2 (as discussed in 4.5.3 and 4.6), which would cause a loss of spatial proximity between RyR2 and $Ca_v1.2$ in diseased cardiomyocytes.

**4.5.3 Reorganization of the regular TT system**

TT network analysis in this thesis showed a progressive loss of TT regularity in both investigated disease models. Additionally, the regular alignment of RyR2 channels along the Z-line striations decreased significantly after MI. These findings are consistent with the previously hypothesized "orphaning" of RyR2s in spontaneously hypertensive rats (SHRs) with advanced HF [96]. Song *et al*. concluded that the increased spatial dispersion of TTs and orphaned RyR2s lead to a loss of local $Ca^{2+}$ release control and $Ca^{2+}$ release instability in HF. Both the decreased JPH2 expression after MI described here and the reorganized JPH2 and RyR2 localizations suggest alterations of the molecular CRU organization.

To assess the impact of an increased CRU spacing due to the heterogeneous remodeling of the TT system in HF, our collaboration partners from the University of Maryland, Baltimore, USA and the George Mason University, Manassas, USA (W.J. Lederer, B. Hagen, G.S.B. Williams, H.-T. M. Tuan and M.S. Jafri) applied a mathematical model of 20,000 individual CRUs [163], a realistic estimate for ventricular cardiomyocytes. HF was modeled by implementation of previously observed changes in ion transport proteins: reduction in fast and slow $K^{+}$ currents, increased NCX expression, decreased Serca2a expression and increased RyR2 sensitivity. [163]. An increased spacing between TTs and RyR2s (30-fold increase in subspace volume, equivalent to a RyR2-TT distance of 300 nm) was implemented at only 25 % of the considered CRUs to simulate heterogeneous spatial changes.

Under steady-state conditions, the model revealed that spatial reorganization of TTs and RyR2s aggravates delays and dyssynchrony of SR $Ca^{2+}$ release in HF and thereby leads to further AP prolongation. This promotes severe $Ca^{2+}$ leak in diastole, which may contribute to afterdepolarizations and $Ca^{2+}$-triggered arrhythmias in HF [164].

Taken together, advanced computational modeling showed that relatively small changes in the CRU nanostructure can have severe consequences for E-C coupling, leading to contractile dysfunction.

**4.6 Consideration of TT biogenesis with regard to TT remodeling**

During the early development of HF TT membranes were significantly added and the dimensions of individual TTs increased. These findings are consistent with membrane-additive mechanisms, which might be related to mechanisms of TT biogenesis. It has been shown that certain molecules and mechanisms that regulate growth of the embryonic heart are reactivated in the adult heart in response to stress signals that provoke cardiac enlargement and HF [165].

One mechanism that has been suggested for TT biogenesis is the repetitive generation and fusion of caveolae [8, 166]. It has been shown that the expression of Cav3, an essential protein of caveolae, is induced during differentiation of rat cardiomyocyte [72]. Cav3 associates with developing TTs in skeletal muscle [75] and Cav3 knockout mice exhibit TT abnormalities in skeletal muscle [76]. Furthermore, overexpression of Cav3 in skeletal muscle leads to a dramatic increase in sarcolemmal caveolae [167]. All these findings correlate well with the observation that Cav3 expression is significantly increased 4pMI, the specific time-point where a strong increase of longitudinal TT elements was observed (Figures 3.18 and 3.19, Results). Through immunostaining it could further be shown that the additional longitudinal TTs 4pMI are positive for Cav3. These findings are in agreement with the known role of Cav3 during TT biogenesis and further suggest that Cav3 may directly contribute to the formation of additional TT elements during the early development of HF.

Most studies on TT biogenesis have been conducted in skeletal muscle. In the literature it seems well accepted for skeletal muscle that TT formation occurs by two complementary mechanisms: (1) through invagination and tubulation of the surface sarcolemma and (2) through intracellular addition of membranes by fusion with preformed vesicles [65, 168]. It has been described that during skeletal muscle development TTs are predominantly longitudinal [169, 170]. According to few observational studies on TT biogenesis in cardiomyocytes, in the heart other mechanisms may be involved. The studies by Ziman *et al*. and Sedarat *et al.* did not find the initial longitudinal orientation of developing TTs, but rather structures at the cell periphery which moved into the cell during development [64, 79]. Therefore, follow-up studies of TT biogenesis in cardiomyocytes may consider the critical question what differences occur between the development in cardiac and skeletal muscle.

Besides Cav3, the expression of JPH2 has been analyzed in this thesis. JPH2 promotes the formation of junctions between TTs and the SR and seems to be involved in the functional maturation of couplons [64, 78]. JPH2 expression is up-regulated during heart development and down-regulated in hypertrophic or dilated cardiomyopathy mouse models [171]. Wei *et al.* also described a decrease of JPH2 expression in different stages of HF in rat after TAC [97]. These findings correlate closely with the observed decrease of JPH2 expression after MI in this study. It would be interesting to see if at an

earlier time-point after MI or TAC, JPH2 expression was sufficient to enable the formation of functional couplons. This would support the hypothesis that in the early compensatory hypertrophic phase additional TTs might sustain a synchronous $Ca^{2+}$ release throughout the cardiomyocyte.

In summary, the differential expression of Cav3 and JPH2 during early development of HF suggests similarities between the biogenesis of the TT system after birth and the observed proliferative TT remodeling during the onset of HF.

## 4.7 Summary and outlook

In summary, this thesis demonstrated that STED microscopy provides significantly new insight into the TT morphology in living cardiomyocytes which was previously unattainable due to methodological limitations. Novel quantitative image analysis strategies allowed the characterization of individual TTs and of TT network properties in healthy and diseased cardiomyocytes. Applying STED microscopy, a mechanism of proliferative TT remodeling was uncovered during the early development of HF. This study further considered a potential role of Cav3 in the observed additive membrane remodeling. In addition, decreased JPH2 expression, TT disorganization and RyR2 rearrangement during HF development indicated an increased CRU spacing in failing cardiomyocytes which might impair E-C coupling and lead to contractile dysfunction.

Recent experimental studies showed a restoration of the pathologically remodeled TT system. These very different attempts included cardiac resynchronization therapy in a canine model of pacing-induced HF [172], AAV9.SERCA2a gene therapy in failing rat cardiomyocytes [173], interval training in a mouse model of diabetic cardiomyopathy [174] or mechanical unloading in a rat model of HF following MI [175]. However, before therapeutic interference to inhibit TT remodeling can become a therapeutic strategy for patients with HF, the mechanisms underlying TT remodeling have to be better understood. For that purpose, an extension of this study may involve the investigation of additional time-points, particularly during the early development of HF. Especially the identification of stages where remodeling is still compensatory might be important to delineate potential therapeutic interventions. Furthermore, TT biogenesis could be investigated with the developed imaging and analysis strategies and with regard to proteins that might be implicated in TT formation. Genomewide expression and transcriptome analyses in developing as well as in failing cardiomyocytes might identify further proteins that could play a role in the developmental, the compensatory or the maladaptive TT formation.

In the future, STED microscopy and other super-resolution strategies might be used for functional measurements in living cardiomyocytes, e.g. for nanometric imaging of $Ca^{2+}$ release events in combination with structural stainings. Such studies might be extended to the behavior of TTs or other structures during stretch. Ultimately, interventions that may prevent TT remodeling can be tested with high sensitivity using super-resolution techniques. Furthermore, the analysis of human cardiomyocytes from patients with different types of heart disease will become an important area of investigation.

**5 References**

1.		Soeller, C. and M.B. Cannell, *Examination of the transverse tubular system in living cardiac rat myocytes by 2-photon microscopy and digital image-processing techniques.* Circ Res, 1999. **84**(3): p. 266-75.

2.		Huxley, A.F. and R.E. Taylor, *Local activation of striated muscle fibres.* J Physiol, 1958. **144**(3): p. 426-41.

3.		Huxley, A.F. and R. Niedergerke, *Measurement of the striations of isolated muscle fibres with the interference microscope.* J Physiol, 1958. **144**(3): p. 403-25.

4.		Bennett, H.S. and K.R. Porter, *An electron microscope study of sectioned breast muscle of the domestic fowl.* Am J Anat, 1953. **93**(1): p. 61-105.

5.		Karrer, H.E., *The striated musculature of blood vessels. I. General cell morphology.* J Biophys Biochem Cytol, 1959. **6**: p. 383-92.

6.		Lindner, E., *Die submikroskopische Morphologie des Herzmuskels.* Zeitschrift für Zellforschung, 1957. **45**: p. 702-746.

7.		Fawcett, D.W. and N.S. McNutt, *The ultrastructure of the cat myocardium. I. Ventricular papillary muscle.* J Cell Biol, 1969. **42**(1): p. 1-45.

8.		Forbes, M.S., L.A. Hawkey, and N. Sperelakis, *The transverse-axial tubular system (TATS) of mouse myocardium: its morphology in the developing and adult animal.* Am J Anat, 1984. **170**(2): p. 143-62.

9.		Huxley, H.E., *Evidence for Continuity between the Central Elements of the Triads and Extracellular Space in Frog Sartorius Muscle.* Nature, 1964. **202**: p. 1067-71.

10.		Franzini-Armstrong, C., R.A. Venosa, and P. Horowicz, *Morphology and accessibility of the 'transverse' tubular system in frog sartorius muscle after glycerol treatment.* J Membr Biol, 1973. **14**(3): p. 197-212.

11.		Franzini-Armstrong, C. and K.R. Porter, *Sarcolemmal Invaginations Constituting the T System in Fish Muscle Fibers.* J Cell Biol, 1964. **22**: p. 675-96.

12.		Franzini-Armstrong, C., L. Landmesser, and G. Pilar, *Size and shape of transverse tubule openings in frog twitch muscle fibers.* J Cell Biol, 1975. **64**(2): p. 493-7.

13.		Franzini-Armstrong, C., et al., *T-tubule swelling in hypertonic solutions: a freeze substitution study.* J Physiol, 1978. **283**: p. 133-40.

14.		Franzini-Armstrong, C., A.B. Eastwood, and L.D. Peachey, *Shape and disposition of clefts, tubules, and sarcoplasmic reticulum in long and short sarcomere fibers of crab and crayfish.* Cell Tissue Res, 1986. **244**(1): p. 9-19.

15.		Franzini-Armstrong, C., *STUDIES OF THE TRIAD : I. Structure of the Junction in Frog Twitch Fibers.* J Cell Biol, 1970. **47**(2): p. 488-99.

16.		Hayashi, T., et al., *Three-dimensional electron microscopy reveals new details of membrane systems for Ca2+ signaling in the heart.* J Cell Sci, 2009. **122**(Pt 7): p. 1005-13.

17.		Brette, F. and C. Orchard, *Resurgence of cardiac t-tubule research.* Physiology (Bethesda), 2007. **22**: p. 167-73.

18.     Bu, G., et al., *Uniform action potential repolarization within the sarcolemma of in situ ventricular cardiomyocytes.* Biophys J, 2009. **96**(6): p. 2532-46.

19.     Song, L.S., et al., *Calcium biology of the transverse tubules in heart.* Ann N Y Acad Sci, 2005. **1047**: p. 99-111.

20.     Brette, F. and C. Orchard, *T-tubule function in mammalian cardiac myocytes.* Circ Res, 2003. **92**(11): p. 1182-92.

21.     Gu, Y., et al., *High-resolution scanning patch-clamp: new insights into cell function.* FASEB J, 2002. **16**(7): p. 748-50.

22.     Despa, S., et al., *Na/Ca exchange and Na/K-ATPase function are equally concentrated in transverse tubules of rat ventricular myocytes.* Biophys J, 2003. **85**(5): p. 3388-96.

23.     Page, E., *Quantitative ultrastructural analysis in cardiac membrane physiology.* Am J Physiol, 1978. **235**(5): p. C147-58.

24.     Smyrnias, I., et al., *Comparison of the T-tubule system in adult rat ventricular and atrial myocytes, and its role in excitation-contraction coupling and inotropic stimulation.* Cell Calcium, 2010. **47**(3): p. 210-23.

25.     Sandow, A., *Excitation-contraction coupling in muscular response.* Yale J Biol Med, 1952. **25**(3): p. 176-201.

26.     Scriven, D.R., P. Dan, and E.D. Moore, *Distribution of proteins implicated in excitation-contraction coupling in rat ventricular myocytes.* Biophys J, 2000. **79**(5): p. 2682-91.

27.     Carl, S.L., et al., *Immunolocalization of sarcolemmal dihydropyridine receptor and sarcoplasmic reticular triadin and ryanodine receptor in rabbit ventricle and atrium.* J Cell Biol, 1995. **129**(3): p. 673-82.

28.     Fabiato, A., *Calcium-induced release of calcium from the cardiac sarcoplasmic reticulum.* Am J Physiol, 1983. **245**(1): p. C1-14.

29.     Fabiato, A. and F. Fabiato, *Contractions induced by a calcium-triggered release of calcium from the sarcoplasmic reticulum of single skinned cardiac cells.* J Physiol, 1975. **249**(3): p. 469-95.

30.     Orchard, C. and F. Brette, *t-Tubules and sarcoplasmic reticulum function in cardiac ventricular myocytes.* Cardiovasc Res, 2008. **77**(2): p. 237-44.

31.     Parvatiyar, M.S., et al., *Cardiac troponin mutations and restrictive cardiomyopathy.* J Biomed Biotechnol, 2010. **2010**: p. 350706.

32.     Gordon, A.M., E. Homsher, and M. Regnier, *Regulation of contraction in striated muscle.* Physiol Rev, 2000. **80**(2): p. 853-924.

33.     Yang, Z., et al., *Na+-Ca2+ exchange activity is localized in the T-tubules of rat ventricular myocytes.* Circ Res, 2002. **91**(4): p. 315-22.

34.     Stern, M.D., G. Pizarro, and E. Rios, *Local control model of excitation-contraction coupling in skeletal muscle.* J Gen Physiol, 1997. **110**(4): p. 415-40.

35.     Bers, D.M. and V.M. Stiffel, *Ratio of ryanodine to dihydropyridine receptors in cardiac and skeletal muscle and implications for E-C coupling.* Am J Physiol, 1993. **264**(6 Pt 1): p. C1587-93.

36. Franzini-Armstrong, C., F. Protasi, and V. Ramesh, *Shape, size, and distribution of Ca(2+) release units and couplons in skeletal and cardiac muscles.* Biophys J, 1999. **77**(3): p. 1528-39.

37. Winslow, R.L. and J.L. Greenstein, *Cardiac myocytes and local signaling in nano-domains.* Prog Biophys Mol Biol, 2011. **107**(1): p. 48-59.

38. Eggermann, E., et al., *Nanodomain coupling between Ca(2)(+) channels and sensors of exocytosis at fast mammalian synapses.* Nat Rev Neurosci, 2012. **13**(1): p. 7-21.

39. Cheng, H. and W.J. Lederer, *Calcium sparks.* Physiol Rev, 2008. **88**(4): p. 1491-545.

40. Page, E. and L.P. McCallister, *Quantitative electron microscopic description of heart muscle cells. Application to normal, hypertrophied and thyroxin-stimulated hearts.* Am J Cardiol, 1973. **31**(2): p. 172-81.

41. Cheng, H., W.J. Lederer, and M.B. Cannell, *Calcium sparks: elementary events underlying excitation-contraction coupling in heart muscle.* Science, 1993. **262**(5134): p. 740-4.

42. Tsien, R.Y., *Monitoring Cell Calcium, ed. by E. Carafoli and C. Klee. New York: Oxford University Press.* Calcium as a Cellular Regulator, 1999: p. 28-54.

43. Lukyanenko, V., et al., *Functional groups of ryanodine receptors in rat ventricular cells.* J Physiol, 2007. **583**(Pt 1): p. 251-69.

44. Cannell, M.B. and C.H. Kong, *Local control in cardiac E-C coupling.* J Mol Cell Cardiol, 2012. **52**(2): p. 298-303.

45. Cannell, M.B., H. Cheng, and W.J. Lederer, *The control of calcium release in heart muscle.* Science, 1995. **268**(5213): p. 1045-9.

46. Gomez, A.M., et al., *Heart failure after myocardial infarction: altered excitation-contraction coupling.* Circulation, 2001. **104**(6): p. 688-93.

47. Lipp, P., et al., *Subcellular properties of triggered Ca2+ waves in isolated citrate-loaded guinea-pig atrial myocytes characterized by ratiometric confocal microscopy.* J Physiol, 1996. **497 ( Pt 3)**: p. 599-610.

48. Huser, J., S.L. Lipsius, and L.A. Blatter, *Calcium gradients during excitation-contraction coupling in cat atrial myocytes.* J Physiol, 1996. **494 ( Pt 3)**: p. 641-51.

49. Mackenzie, L., et al., *Predetermined recruitment of calcium release sites underlies excitation-contraction coupling in rat atrial myocytes.* J Physiol, 2001. **530**(Pt 3): p. 417-29.

50. Berlin, J.R., *Spatiotemporal changes of Ca2+ during electrically evoked contractions in atrial and ventricular cells.* Am J Physiol, 1995. **269**(3 Pt 2): p. H1165-70.

51. Li, Q., et al., *Mechanisms by which cytoplasmic calcium wave propagation and alternans are generated in cardiac atrial myocytes lacking T-tubules-insights from a simulation study.* Biophys J, 2012. **102**(7): p. 1471-82.

52. Kirk, M.M., et al., *Role of the transverse-axial tubule system in generating calcium sparks and calcium transients in rat atrial myocytes.* J Physiol, 2003. **547**(Pt 2): p. 441-51.

53. Leeson, T.S., *T-tubules, couplings and myofibrillar arrangements in rat atrial myocardium.* Acta Anat (Basel), 1980. **108**(3): p. 374-88.

54.     Bossen, E.H., J.R. Sommer, and R.A. Waugh, *Comparative stereology of the mouse and finch left ventricle.* Tissue Cell, 1978. **10**(4): p. 773-84.

55.     Bossen, E.H. and J.R. Sommer, *Comparative stereology of the lizard and frog myocardium.* Tissue Cell, 1984. **16**(2): p. 173-8.

56.     Breisch, E.A., et al., *Ultrastructural morphometry of the myocardium of Thunnus alalunga.* Cell Tissue Res, 1983. **233**(2): p. 427-38.

57.     Myklebust, R. and H. Kryvi, *Ultrastructure of the heart of the sturgeon Acipenser stellatus (Chondrostei).* Cell Tissue Res, 1979. **202**(3): p. 431-8.

58.     Berge, P.I., *The cardiac ultrastructure of Chimaera monstrosa L. (Elasmobranchii: Holocephali).* Cell Tissue Res, 1979. **201**(2): p. 181-95.

59.     Ibrahim, M., et al., *The structure and function of cardiac t-tubules in health and disease.* Proc Biol Sci, 2011. **278**(1719): p. 2714-23.

60.     Heinzel, F.R., et al., *Spatial and temporal inhomogeneities during Ca2+ release from the sarcoplasmic reticulum in pig ventricular myocytes.* Circ Res, 2002. **91**(11): p. 1023-30.

61.     Perni, S., V.R. Iyer, and C. Franzini-Armstrong, *Ultrastructure of cardiac muscle in reptiles and birds: optimizing and/or reducing the probability of transmission between calcium release units.* J Muscle Res Cell Motil, 2012. **33**(2): p. 145-52.

62.     Stern, M.D., *Theory of excitation-contraction coupling in cardiac muscle.* Biophys J, 1992. **63**(2): p. 497-517.

63.     Smolich, J.J., *Ultrastructural and functional features of the developing mammalian heart: a brief overview.* Reprod Fertil Dev, 1995. **7**(3): p. 451-61.

64.     Ziman, A.P., et al., *Excitation-contraction coupling changes during postnatal cardiac development.* J Mol Cell Cardiol, 2010. **48**(2): p. 379-86.

65.     Di Maio, A., et al., *T-tubule formation in cardiacmyocytes: two possible mechanisms?* J Muscle Res Cell Motil, 2007. **28**(4-5): p. 231-41.

66.     Lee, E., et al., *Amphiphysin 2 (Bin1) and T-tubule biogenesis in muscle.* Science, 2002. **297**(5584): p. 1193-6.

67.     Butler, M.H., et al., *Amphiphysin II (SH3P9; BIN1), a member of the amphiphysin/Rvs family, is concentrated in the cortical cytomatrix of axon initial segments and nodes of ranvier in brain and around T tubules in skeletal muscle.* J Cell Biol, 1997. **137**(6): p. 1355-67.

68.     Razzaq, A., et al., *Amphiphysin is necessary for organization of the excitation-contraction coupling machinery of muscles, but not for synaptic vesicle endocytosis in Drosophila.* Genes Dev, 2001. **15**(22): p. 2967-79.

69.     Fugier, C., et al., *Misregulated alternative splicing of BIN1 is associated with T tubule alterations and muscle weakness in myotonic dystrophy.* Nat Med, 2011. **17**(6): p. 720-5.

70.     Muller, A.J., et al., *Targeted disruption of the murine Bin1/Amphiphysin II gene does not disable endocytosis but results in embryonic cardiomyopathy with aberrant myofibril formation.* Mol Cell Biol, 2003. **23**(12): p. 4295-306.

71.     Ishikawa, H., *Formation of elaborate networks of T-system tubules in cultured skeletal muscle with special reference to the T-system formation.* J Cell Biol, 1968. **38**(1): p. 51-66.

72.    Rybin, V.O., et al., *Caveolae-associated proteins in cardiomyocytes: caveolin-2 expression and interactions with caveolin-3.* Am J Physiol Heart Circ Physiol, 2003. **285**(1): p. H325-32.

73.    Cohen, A.W., et al., *Role of caveolae and caveolins in health and disease.* Physiol Rev, 2004. **84**(4): p. 1341-79.

74.    Tang, Z., et al., *Molecular cloning of caveolin-3, a novel member of the caveolin gene family expressed predominantly in muscle.* J Biol Chem, 1996. **271**(4): p. 2255-61.

75.    Parton, R.G., et al., *Caveolin-3 associates with developing T-tubules during muscle differentiation.* J Cell Biol, 1997. **136**(1): p. 137-54.

76.    Galbiati, F., et al., *Caveolin-3 null mice show a loss of caveolae, changes in the microdomain distribution of the dystrophin-glycoprotein complex, and t-tubule abnormalities.* J Biol Chem, 2001. **276**(24): p. 21425-33.

77.    Garbino, A. and X.H. Wehrens, *Emerging role of junctophilin-2 as a regulator of calcium handling in the heart.* Acta Pharmacol Sin, 2010. **31**(9): p. 1019-21.

78.    Takeshima, H., et al., *Junctophilins: a novel family of junctional membrane complex proteins.* Mol Cell, 2000. **6**(1): p. 11-22.

79.    Sedarat, F., et al., *Colocalization of dihydropyridine and ryanodine receptors in neonate rabbit heart using confocal microscopy.* Am J Physiol Heart Circ Physiol, 2000. **279**(1): p. H202-9.

80.    van Oort, R.J., et al., *Disrupted junctional membrane complexes and hyperactive ryanodine receptors after acute junctophilin knockdown in mice.* Circulation, 2011. **123**(9): p. 979-88.

81.    Louch, W.E., O.M. Sejersted, and F. Swift, *There goes the neighborhood: pathological alterations in T-tubule morphology and consequences for cardiomyocyte Ca2+ handling.* J Biomed Biotechnol, 2010. **2010**: p. 503906.

82.    Levy, D., et al., *The progression from hypertension to congestive heart failure.* JAMA, 1996. **275**(20): p. 1557-62.

83.    Bers, D.M., *Altered cardiac myocyte Ca regulation in heart failure.* Physiology (Bethesda), 2006. **21**: p. 380-7.

84.    Pieske, B., et al., *Ca2+ handling and sarcoplasmic reticulum Ca2+ content in isolated failing and nonfailing human myocardium.* Circ Res, 1999. **85**(1): p. 38-46.

85.    Gomez, A.M., et al., *Defective excitation-contraction coupling in experimental cardiac hypertrophy and heart failure.* Science, 1997. **276**(5313): p. 800-6.

86.    He, J., et al., *Reduction in density of transverse tubules and L-type Ca(2+) channels in canine tachycardia-induced heart failure.* Cardiovasc Res, 2001. **49**(2): p. 298-307.

87.    Balijepalli, R.C., et al., *Depletion of T-tubules and specific subcellular changes in sarcolemmal proteins in tachycardia-induced heart failure.* Cardiovasc Res, 2003. **59**(1): p. 67-77.

88.    Heinzel, F.R., et al., *Remodeling of T-tubules and reduced synchrony of Ca2+ release in myocytes from chronically ischemic myocardium.* Circ Res, 2008. **102**(3): p. 338-46.

89.    Louch, W.E., et al., *T-tubule disorganization and reduced synchrony of Ca2+ release in murine cardiomyocytes following myocardial infarction.* J Physiol, 2006. **574**(Pt 2): p. 519-33.

90. Louch, W.E., et al., *Reduced synchrony of Ca2+ release with loss of T-tubules-a comparison to Ca2+ release in human failing cardiomyocytes.* Cardiovasc Res, 2004. **62**(1): p. 63-73.

91. Lyon, A.R., et al., *Loss of T-tubules and other changes to surface topography in ventricular myocytes from failing human and rat heart.* Proc Natl Acad Sci U S A, 2009. **106**(16): p. 6854-9.

92. Kemi, O.J., et al., *The effect of exercise training on transverse tubules in normal, remodeled, and reverse remodeled hearts.* J Cell Physiol, 2011. **226**(9): p. 2235-43.

93. Lipp, P., et al., *Spatially non-uniform Ca2+ signals induced by the reduction of transverse tubules in citrate-loaded guinea-pig ventricular myocytes in culture.* J Physiol, 1996. **497 ( Pt 3)**: p. 589-97.

94. Brette, F., et al., *Spatiotemporal characteristics of SR Ca(2+) uptake and release in detubulated rat ventricular myocytes.* J Mol Cell Cardiol, 2005. **39**(5): p. 804-12.

95. Cannell, M.B., D.J. Crossman, and C. Soeller, *Effect of changes in action potential spike configuration, junctional sarcoplasmic reticulum micro-architecture and altered t-tubule structure in human heart failure.* J Muscle Res Cell Motil, 2006. **27**(5-7): p. 297-306.

96. Song, L.S., et al., *Orphaned ryanodine receptors in the failing heart.* Proc Natl Acad Sci U S A, 2006. **103**(11): p. 4305-10.

97. Wei, S., et al., *T-tubule remodeling during transition from hypertrophy to heart failure.* Circ Res, 2010. **107**(4): p. 520-31.

98. Franzini-Armstrong, C., F. Protasi, and P. Tijskens, *The assembly of calcium release units in cardiac muscle.* Ann N Y Acad Sci, 2005. **1047**: p. 76-85.

99. Moradi, I. and M. Behjati, *Six common errors cause dangerous mistakes in interpretation of electron micrographs.* Microsc Res Tech, 2012. **75**(5): p. 677-82.

100. Shevchuk, A.I., et al., *Simultaneous measurement of Ca2+ and cellular dynamics: combined scanning ion conductance and optical microscopy to study contracting cardiac myocytes.* Biophys J, 2001. **81**(3): p. 1759-64.

101. Abbe, E., *Beiträge zur Theorie des Mikroskops und der mikroskopischen Wahrnehmung.* Arch f Mikroskop Anat, 1873. **9**: p. 413-420.

102. Hell, S.W., et al., *Nanoscale Resolution with Focused Light: Stimulated Emission Depletion and Other Reversible Saturable Optical Fluorescence Transitions Microscopy Concepts.* Handbook of Biological Confocal Microscopy, 3rd edition, 2006: p. 571-579.

103. Born, M. and E. Wolf, *Principles of optics - Electromagnetic theory of propagation, interference and diffraction of light.* Principles of Optics 7th edition, 2002.

104. Hofmann, M., et al., *Breaking the diffraction barrier in fluorescence microscopy at low light intensities by using reversibly photoswitchable proteins.* Proc Natl Acad Sci U S A, 2005. **102**(49): p. 17565-9.

105. Hell, S.W. and J. Wichmann, *Breaking the diffraction resolution limit by stimulated emission: stimulated-emission-depletion fluorescence microscopy.* Opt Lett, 1994. **19**(11): p. 780-2.

106. Klar, T.A., et al., *Fluorescence microscopy with diffraction resolution barrier broken by stimulated emission.* Proc Natl Acad Sci U S A, 2000. **97**(15): p. 8206-10.

107.    Einstein, A., *Zur Quantentheorie der Strahlung.* Physik Zeitschr, 1917. **18**: p. 121-128.

108.    Hell, S.W., *Far-field optical nanoscopy.* Science, 2007. **316**(5828): p. 1153-8.

109.    Hell, S.W., *Microscopy and its focal switch.* Nat Methods, 2009. **6**(1): p. 24-32.

110.    Lauterbach, M.A., et al., *Comparing video-rate STED nanoscopy and confocal microscopy of living neurons.* J Biophotonics, 2010. **3**(7): p. 417-24.

111.    Westphal, V., et al., *Video-rate far-field optical nanoscopy dissects synaptic vesicle movement.* Science, 2008. **320**(5873): p. 246-9.

112.    Lauterbach, M., *Fast STED Microscopy.* Dissertation, 2009.

113.    Harke, B., et al., *Resolution scaling in STED microscopy.* Opt Express, 2008. **16**(6): p. 4154-62.

114.    Lehnart, S.E., et al., *Phosphodiesterase 4D deficiency in the ryanodine-receptor complex promotes heart failure and arrhythmias.* Cell, 2005. **123**(1): p. 25-35.

115.    Wehrens, X.H., et al., *Enhancing calstabin binding to ryanodine receptors improves cardiac and skeletal muscle function in heart failure.* Proc Natl Acad Sci U S A, 2005. **102**(27): p. 9607-12.

116.    Toischer, K., et al., *Differential cardiac remodeling in preload versus afterload.* Circulation, 2010. **122**(10): p. 993-1003.

117.    Heys, J.J., et al., *Revisiting the simplified bernoulli equation.* Open Biomed Eng J, 2010. **4**: p. 123-8.

118.    Quinones, M.A., et al., *Recommendations for quantification of Doppler echocardiography: a report from the Doppler Quantification Task Force of the Nomenclature and Standards Committee of the American Society of Echocardiography.* J Am Soc Echocardiogr, 2002. **15**(2): p. 167-84.

119.    O'Connell, T.D., M.C. Rodrigo, and P.C. Simpson, *Isolation and culture of adult mouse cardiac myocytes.* Methods Mol Biol, 2007. **357**: p. 271-96.

120.    Janssen, P.M., et al., *The trabecula culture system: a novel technique to study contractile parameters over a multiday time period.* Am J Physiol, 1998. **274**(5 Pt 2): p. H1481-8.

121.    Lauterbach, M.A., et al., *Dynamic imaging of colloidal-crystal nanostructures at 200 frames per second.* Langmuir, 2010. **26**(18): p. 14400-4.

122.    Schindelin, J., et al., *Fiji: an open-source platform for biological-image analysis.* Nat Methods, 2012. **9**(7): p. 676-82.

123.    Eggeling, C., et al., *Direct observation of the nanoscale dynamics of membrane lipids in a living cell.* Nature, 2009. **457**(7233): p. 1159-62.

124.    Loew, L.M., *Potentiometric dyes: Imaging electrical activity of cell membranes.* Pure and Appl Chem, 1996. **68**(7): p. 1405-1409.

125.    Hare, J.M., et al., *Contribution of caveolin protein abundance to augmented nitric oxide signaling in conscious dogs with pacing-induced heart failure.* Circ Res, 2000. **86**(10): p. 1085-92.

126. Rockman, H.A., et al., *Segregation of atrial-specific and inducible expression of an atrial natriuretic factor transgene in an in vivo murine model of cardiac hypertrophy.* Proc Natl Acad Sci U S A, 1991. **88**(18): p. 8277-81.

127. deAlmeida, A.C., R.J. van Oort, and X.H. Wehrens, *Transverse aortic constriction in mice.* J Vis Exp, 2010(38).

128. Savio-Galimberti, E., et al., *Novel features of the rabbit transverse tubular system revealed by quantitative analysis of three-dimensional reconstructions from confocal images.* Biophys J, 2008. **95**(4): p. 2053-62.

129. Tidball, J.G., J.E. Cederdahl, and D.M. Bers, *Quantitative analysis of regional variability in the distribution of transverse tubules in rabbit myocardium.* Cell Tissue Res, 1991. **264**(2): p. 293-8.

130. Galbraith, C.G. and J.A. Galbraith, *Super-resolution microscopy at a glance.* J Cell Sci, 2011. **124**(Pt 10): p. 1607-11.

131. Rust, M.J., M. Bates, and X. Zhuang, *Sub-diffraction-limit imaging by stochastic optical reconstruction microscopy (STORM).* Nat Methods, 2006. **3**(10): p. 793-5.

132. Betzig, E., et al., *Imaging intracellular fluorescent proteins at nanometer resolution.* Science, 2006. **313**(5793): p. 1642-5.

133. Hess, S.T., T.P. Girirajan, and M.D. Mason, *Ultra-high resolution imaging by fluorescence photoactivation localization microscopy.* Biophys J, 2006. **91**(11): p. 4258-72.

134. Toomre, D. and J. Bewersdorf, *A new wave of cellular imaging.* Annu Rev Cell Dev Biol, 2010. **26**: p. 285-314.

135. Brette, F., K. Komukai, and C.H. Orchard, *Validation of formamide as a detubulation agent in isolated rat cardiac cells.* Am J Physiol Heart Circ Physiol, 2002. **283**(4): p. H1720-8.

136. Fluhler, E., V.G. Burnham, and L.M. Loew, *Spectra, membrane binding, and potentiometric responses of new charge shift probes.* Biochemistry, 1985. **24**(21): p. 5749-55.

137. Loew, L.M. and L.L. Simpson, *Charge-shift probes of membrane potential: a probable electrochromic mechanism for p-aminostyrylpyridinium probes on a hemispherical lipid bilayer.* Biophys J, 1981. **34**(3): p. 353-65.

138. Loew, L.M., *Design and Use of Organic Voltage Sensitive Dyes.* Membrane Potential Imaging in the Nervous System: Methods and Applications, 2010: p. 13-23.

139. Bedlack, R.S., Jr., et al., *Distinct electric potentials in soma and neurite membranes.* Neuron, 1994. **13**(5): p. 1187-93.

140. Erlichman, J.S., et al., *Chemosensory responses to CO2 in multiple brain stem nuclei determined using a voltage-sensitive dye in brain slices from rats.* J Neurophysiol, 2009. **102**(3): p. 1577-90.

141. Wuskell, J.P., et al., *Synthesis, spectra, delivery and potentiometric responses of new styryl dyes with extended spectral ranges.* J Neurosci Methods, 2006. **151**(2): p. 200-15.

142. Dedecker, P., et al., *Orientational effects in the excitation and de-excitation of single molecules interacting with donut-mode laser beams.* Opt Express, 2007. **15**(6): p. 3372-83.

143.    Ha, T., et al., *Polarization Spectroscopy of Single Fluorescent Molecules.* J Phys Chem B, 1999. **103**(33): p. 6839-50.

144.    Lygate, C., *Surgical models of hypertrophy and heart failure: Myocardial infarction and transverse aortic constriction.* Drug Discovery Today: Disease Models, 2006. **3**(3): p. 283-290.

145.    Selye, H., et al., *Simple techniques for the surgical occlusion of coronary vessels in the rat.* Angiology, 1960. **11**: p. 398-407.

146.    Zolotareva, A.G. and M.E. Kogan, *Production of experimental occlusive myocardial infarction in mice.* Cor Vasa, 1978. **20**(4): p. 308-14.

147.    Ertl, G. and S. Frantz, *Healing after myocardial infarction.* Cardiovasc Res, 2005. **66**(1): p. 22-32.

148.    Kanno, S., et al., *Echocardiographic evaluation of ventricular remodeling in a mouse model of myocardial infarction.* J Am Soc Echocardiogr, 2002. **15**(6): p. 601-9.

149.    Takaoka, H., et al., *Heart size-independent analysis of myocardial function in murine pressure overload hypertrophy.* Am J Physiol Heart Circ Physiol, 2002. **282**(6): p. H2190-7.

150.    Nakamura, A., et al., *LV systolic performance improves with development of hypertrophy after transverse aortic constriction in mice.* Am J Physiol Heart Circ Physiol, 2001. **281**(3): p. H1104-12.

151.    Liao, Y., et al., *Echocardiographic assessment of LV hypertrophy and function in aortic-banded mice: necropsy validation.* Am J Physiol Heart Circ Physiol, 2002. **282**(5): p. H1703-8.

152.    Patten, R.D. and M.R. Hall-Porter, *Small animal models of heart failure: development of novel therapies, past and present.* Circ Heart Fail, 2009. **2**(2): p. 138-44.

153.    Mirotsou, M., et al., *Elucidating the molecular mechanism of cardiac remodeling using a comparative genomic approach.* Physiol Genomics, 2003. **15**(2): p. 115-26.

154.    Ohler, A., et al., *Two-photon laser scanning microscopy of the transverse-axial tubule system in ventricular cardiomyocytes from failing and non-failing human hearts.* Cardiol Res Pract, 2009. **2009**: p. 802373.

155.    Crossman, D.J., et al., *Changes in the organization of excitation-contraction coupling structures in failing human heart.* PLoS One, 2011. **6**(3): p. e17901.

156.    Kaprielian, R.R., et al., *Distinct patterns of dystrophin organization in myocyte sarcolemma and transverse tubules of normal and diseased human myocardium.* Circulation, 2000. **101**(22): p. 2586-94.

157.    Maron, B.J., V.J. Ferrans, and W.C. Roberts, *Ultrastructural features of degenerated cardiac muscle cells in patients with cardiac hypertrophy.* Am J Pathol, 1975. **79**(3): p. 387-434.

158.    Schaper, J., et al., *Impairment of the myocardial ultrastructure and changes of the cytoskeleton in dilated cardiomyopathy.* Circulation, 1991. **83**(2): p. 504-14.

159.    Shorten, P.R., C.D. McMahon, and T.K. Soboleva, *Insulin transport within skeletal muscle transverse tubule networks.* Biophys J, 2007. **93**(9): p. 3001-7.

160.    Ploug, T., et al., *Analysis of GLUT4 distribution in whole skeletal muscle fibers: identification of distinct storage compartments that are recruited by insulin and muscle contractions.* J Cell Biol, 1998. **142**(6): p. 1429-46.

161. Peachey, L.D. and B.R. Eisenberg, *Helicoids in the T system and striations of frog skeletal muscle fibers seen by high voltage electron microscopy.* Biophys J, 1978. **22**(2): p. 145-54.

162. Asghari, P., et al., *Axial tubules of rat ventricular myocytes form multiple junctions with the sarcoplasmic reticulum.* Biophys J, 2009. **96**(11): p. 4651-60.

163. Williams, G.S., et al., *Dynamics of calcium sparks and calcium leak in the heart.* Biophys J, 2011. **101**(6): p. 1287-96.

164. Wagner, E., et al., *Stimulated emission depletion live-cell super-resolution imaging shows proliferative remodeling of T-tubule membrane structures after myocardial infarction.* Circ Res, 2012. **111**(4): p. 402-14.

165. Olson, E.N. and M.D. Schneider, *Sizing up the heart: development redux in disease.* Genes Dev, 2003. **17**(16): p. 1937-56.

166. Carozzi, A.J., et al., *Role of cholesterol in developing T-tubules: analogous mechanisms for T-tubule and caveolae biogenesis.* Traffic, 2000. **1**(4): p. 326-41.

167. Galbiati, F., et al., *Transgenic overexpression of caveolin-3 in skeletal muscle fibers induces a Duchenne-like muscular dystrophy phenotype.* Proc Natl Acad Sci U S A, 2000. **97**(17): p. 9689-94.

168. Al-Qusairi, L. and J. Laporte, *T-tubule biogenesis and triad formation in skeletal muscle and implication in human diseases.* Skelet Muscle, 2011. **1**(1): p. 26.

169. Franzini-Armstrong, C., *Simultaneous maturation of transverse tubules and sarcoplasmic reticulum during muscle differentiation in the mouse.* Dev Biol, 1991. **146**(2): p. 353-63.

170. Takekura, H., B.E. Flucher, and C. Franzini-Armstrong, *Sequential docking, molecular differentiation, and positioning of T-Tubule/SR junctions in developing mouse skeletal muscle.* Dev Biol, 2001. **239**(2): p. 204-14.

171. Minamisawa, S., et al., *Junctophilin type 2 is associated with caveolin-3 and is down-regulated in the hypertrophic and dilated cardiomyopathies.* Biochem Biophys Res Commun, 2004. **325**(3): p. 852-6.

172. Sachse, F.B., et al., *Subcellular structures and function of myocytes impaired during heart failure are restored by cardiac resynchronization therapy.* Circ Res, 2012. **110**(4): p. 588-97.

173. Lyon, A.R., et al., *Plasticity of surface structures and beta(2)-adrenergic receptor localization in failing ventricular cardiomyocytes during recovery from heart failure.* Circ Heart Fail, 2012. **5**(3): p. 357-65.

174. Stolen, T.O., et al., *Interval training normalizes cardiomyocyte function, diastolic Ca2+ control, and SR Ca2+ release synchronicity in a mouse model of diabetic cardiomyopathy.* Circ Res, 2009. **105**(6): p. 527-36.

175. Ibrahim, M., et al., *Mechanical unloading reverses transverse tubule remodelling and normalizes local Ca(2+)-induced Ca(2+)release in a rodent model of heart failure.* Eur J Heart Fail, 2012. **14**(6): p. 571-80.

## 6 Supplement

### 6.1 Supplementary figures
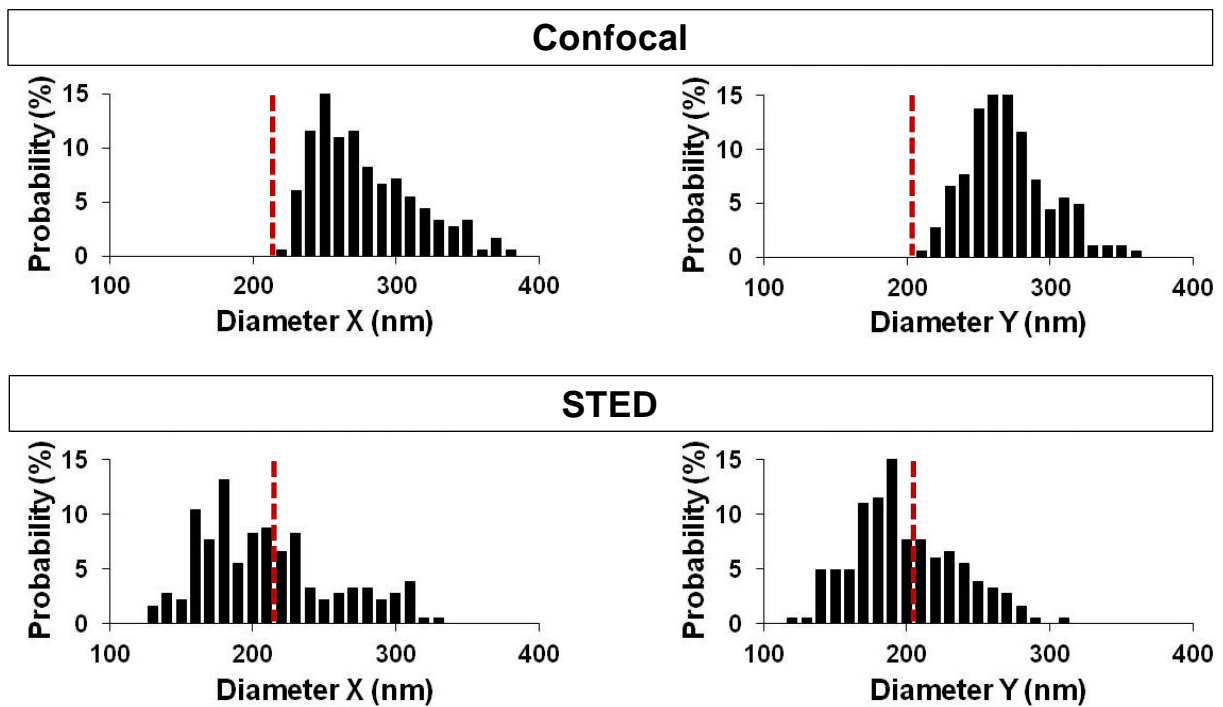


**Figure 6.1 Distribution of submembrane TT diameters determined by 2D Gauss fitting.** Histograms for diameters of 182 TT cross-sections (55 cells, 3 mice) determined in submembrane images. The same set of TT cross-sections was analyzed in STED and confocal images. Diameters were determined as FWHM by 2D Gauss fitting in parallel to the longitudinal cell axis (X) and perpendicular to the longitudinal cell axis (Y). Red dashed lines mark the confocal resolution limit.
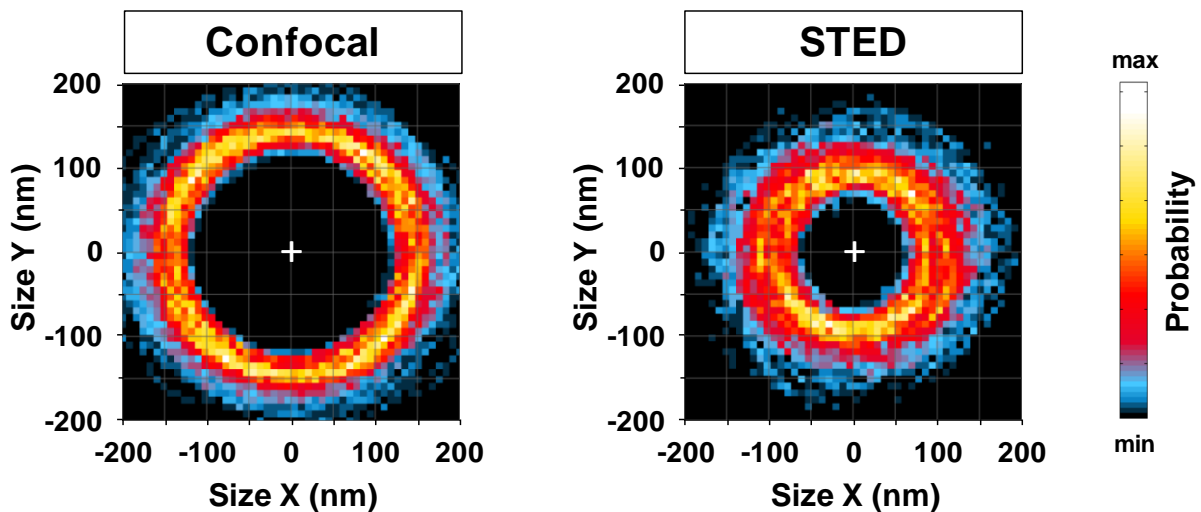


**Figure 6.2 2D contour histograms of submembrane TT cross-sections.** 2D histograms for 182 TT contours extracted from submembrane STED and confocal images. + indicates the point where contours were superimposed (their center of mass). X corresponds to the orientation of the longitudinal cell axis. Color bar on the right illustrates the probability that a contour hits a pixel: black (min) = low probability, white (max) = high probability.
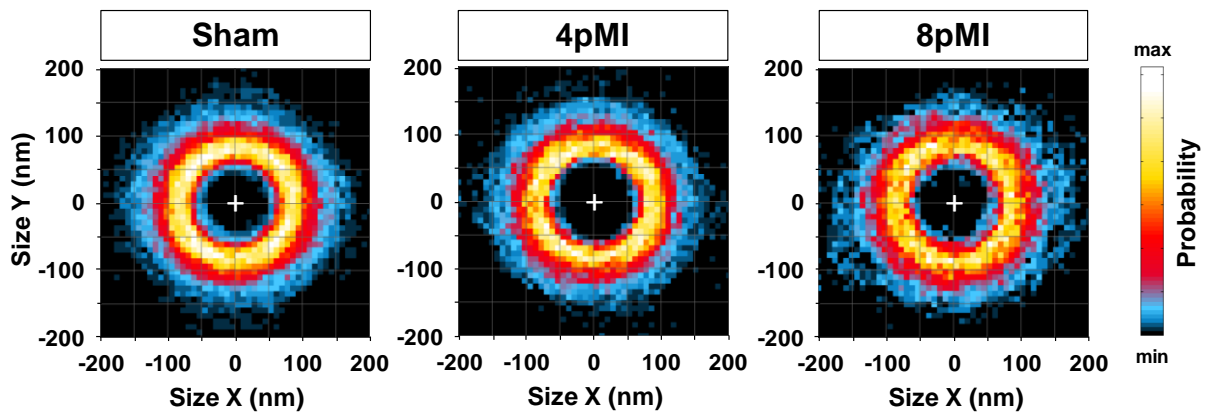
**Figure 6.3 2D contour histograms of submembrane TT cross-sections.** 2D histograms for the following number of TT contours (cells) extracted from submembrane images: Sham 683 (92), 4pMI 343 (61), 8pMI 253 (48). + indicates the point where contours were superimposed (their center of mass). The x-axis corresponds to the orientation of the longitudinal cell axis. Color bar on the right illustrates the probability that a contour hits a pixel: black (min) = low probability, white (max) = high probability.
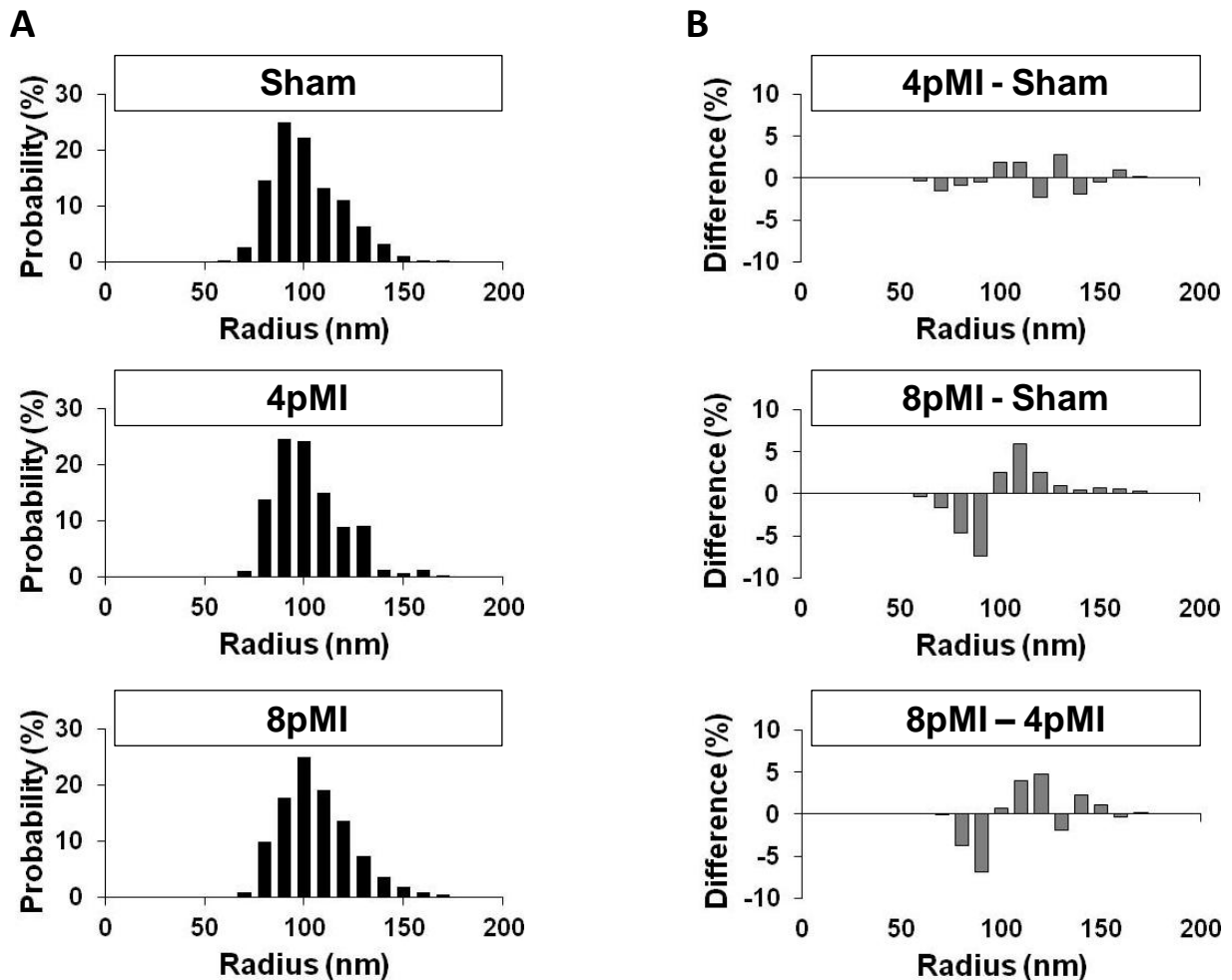


**Figure 6.4 Distributions of radii determined by contour analysis in submembrane images.** Radii were determined as the mean of 120 radii in one contour line. (**A**) Histograms for the following number of TT cross-sections (cells) extracted from submembrane images: Sham 683 (92), 4pMI 343 (61), 8pMI 253 (48). (**B**) Differences between the radius distributions were calculated by subtraction of histograms from the indicated treatment groups.

**6.2 Chemicals**

| Chemical | Company | Order no. |
|---|---|---|
| 2,3-Butanedione monoxime | Sigma-Aldrich, Munich, Germany | B0753 |
| Bovine calf serum | HyClone via | SH30073 |
|  | Thermo Scientific, Schwerte, Germany |  |
| $CaCl_2$ | Sigma-Aldrich, Munich, Germany | C2661 |
| Collagenase type II | Worthington via | on request |
|  | Cell Systems, Troisdorf, Germany |  |
| cOmplete (protease inhibitor cocktail) | Roche, Grenzach , Germany | 11836170001 |
| EGTA | Sigma-Aldrich, Munich, Germany | E3889 |
| Glucose | Carl Roth, Karlsruhe, Germany | HN06.1 |
| Glycine | Carl Roth, Karlsruhe, Germany | 3908.3 |
| HEPES | Carl Roth, Karlsruhe, Germany | 9105.4 |
| KCl | Carl Roth, Karlsruhe, Germany | 6781.3 |
| $KH_2PO_4$ | Carl Roth, Karlsruhe, Germany | 3904.2 |
| Laminin (2 mg/ml) | BD Biosciences, Heidelberg, Germany | 354232 |
| Methanol | Carl Roth, Karlsruhe, Germany | 8388.6 |
| $MgCl_2 \cdot 6\ H_2O$ | Carl Roth, Karlsruhe, Germany | 2189.2 |
| $MgSO_4 \cdot 7\ H_2O$ | Carl Roth, Karlsruhe, Germany | 8283.2 |
| Milk powder | Carl Roth, Karlsruhe, Germany | T145.2 |
| $Na_2HPO_4 \cdot 2\ H_2O$ | Carl Roth, Karlsruhe, Germany | 4984.2 |
| NaCl | Carl Roth, Karlsruhe, Germany | HN00.2 |
| NaCl | Carl Roth, Karlsruhe, Germany | HN00.2 |
| $NaHCO_3$ | Carl Roth, Karlsruhe, Germany | HN01.1 |
| Paraformaldehyde | Sigma-Aldrich, Munich, Germany | 158127 |
| Phosphate buffered saline | Gibco® via | 10010 |
| (pH 7.4, w/o $Ca^{2+}$ and $Mg^{2+}$) | Life Technologies, Darmstadt, Germany |  |
| PhosSTOP | Roche, Grenzach , Germany | 4906837001 |
| (phosphatase inhibitor cocktail) |  |  |
| Sucrose | Sigma-Aldrich, Munich, Germany | S0389 |
| Taurin | Carl Roth, Karlsruhe, Germany | 4721.2 |
| Tris | Carl Roth, Karlsruhe, Germany | 4855.2 |
| Triton X-100 | Sigma-Aldrich, Munich, Germany | T9284 |
| Tween 20 | Sigma-Aldrich, Munich, Germany | P1379 |

**6.3 Drugs**

| Agent | Name | Company |
|-------|------|---------|
| Buprenorphin | Temgesic® | Reckitt Benckiser Healthcare, Slough, UK |
| Isoflurane | Forene® | Abbott, Libertyville, IL, USA |
| Metamizol | Novaminsulfon 500 mg Lichtenstein | Zentiva, Paris, France |

**6.4 Dyes and mounting medium**

| Product | Company | Order no. |
|---------|---------|-----------|
| di-8-ANEPPS | Molecular Probes®, Life Technologies, Darmstadt, Germany | D-3167 |
| di-4-ANEPPS | Molecular Probes®, Life Technologies, Darmstadt, Germany | D-1199 |
| fluo-4/AM | Molecular Probes®, Life Technologies, Darmstadt, Germany | F-14201 |
| ProLong® Gold antifade reagent | Molecular Probes®, Life Technologies, Darmstadt, Germany | P36934 |

**6.5 Consumables**

| Consumable | Company |
|------------|---------|
| 5-0 suture (Polyviolene) | Angiotech, Vancouver, Canada |
| 6-0 suture (Prolene) | Ethicon |
| | part of Johnson & Johnson, Norderstedt, Germany |
| 9-0 (Ethilon) | Ethicon |
| | part of Johnson & Johnson, Norderstedt, Germany |
| BCA protein assay kit | Thermo Scientific, Schwerte, Germany |
| filter paper (, #FP598) | Hahnemühle, Dassel, Germany |
| glass cover slips (Ø 18 mm) | Thermo Scientific, Schwerte, Germany |
| glass cover slips (Ø 42 mm) | Thermo Scientific, Schwerte, Germany |
| Immobilon™ Western horse raddish peroxidase substrate | Merck Millipore, Darmstadt, Germany |
| NuPAGE® MOPS SDS Running Buffer, Novex® | Life Technologies, Darmstadt, Germany |
| NuPAGE® Novex® 4 - 12 % Bis-Tris Gels | Life Technologies, Darmstadt, Germany |
| peqGOLD Protein-Marker V | Peqlab, Erlangen, Germany |
| Protran™ nitrocellulose membrane | Whatman |
| | part of GE Healthcare, Buckinghamshire, UK |

**6.6 General equipment**

| | |
|---|---|
| field stimulator (MyoPacer EP) | IonOptix, Milton, MA, USA |
| Image Station 4000R PRO | Carestream Health Inc., Rochester, NY, USA |
| imaging chamber (POC-R2 chamber system) | PeCon, Erbach, Germany |
| LSM710 | Carl Zeiss, Jena, Germany |
| micropestle | Carl Roth, Karlsruhe, Germany |
| mouse respirator | Hugo Sachs Electronics, Hugstetten, Germany |
| Vevo 2100 | VisualSonics Inc., Toronto, Canada |
| wet blotting apparatus | Life Technologies, Darmstadt, Germany |

**6.7 Parts of the STED setup**

| | |
|---|---|
| 100x 1.4 NA oil objective | Leica, Wetzlar, Germany |
| 675 ± 30 nm bandpass | AHF Analysentechnik, Tübingen, Germany |
| avalanche photodiode (APD) | Perkin Elmer, Waltham, MA, USA |
| piezo stage scanner | Physik Instrumente GmbH, Karlsruhe, Germany |
| pulsed diode laser | Toptica, Munich, Germany |
| resonant mirror scanner | Electro-Optical Products Corp., Glendale, NY, USA |
| single-mode fibers (SMF) | Schäfter + Kirchhoff GmbH, Hamburg, Germany |
| Ti:Sapphire laser (MaiTai) | Spectra-Physics, Darmstadt, Germany |
| vortex phase plate | RPC Photonics, Rochester, NY, USA |

**6.8 Antibodies**

**6.8.1 Primary antibodies**

| Antibody | Company | Order no. | Application | Dilution |
|---|---|---|---|---|
| Mouse anti-GAPDH | Biotrend, Cologne, Germany | 5G4MAB6C5 | Western blot | 1:80,000 |
| Mouse anti-RyR2 | Pierce antibodies via Thermo Scientific, Schwerte, Germany | MA3-916 | immunostain | 1:500 |
| Rabbit anti-JPH2 | Life Technologies, Darmstadt, Germany | 40-5300 | immunostain | 1:500 |
| | | | Western blot | 1:500 |
| Rabbit anti-Cav3 | Abcam, Cambridge, UK | ab2912 | immunostain | 1:500 |
| | | | Western blot | 1:500 |

**6.8.2 Secondary antibodies**

| Antibody | Company | Order no. | Application | Dilution |
|----------|---------|-----------|-------------|----------|
| AlexaFluor®514 goat anti-mouse | Molecular Probes®, Life Technologies, Darmstadt, Germany | A31555 | immunostain | 1:1000 |
| AlexaFluor®633 goat anti-rabbit | Molecular Probes®, Life Technologies, Darmstadt, Germany | A21071 | immunostain | 1:1000 |
| ECL™-HRP-linked sheep anti-mouse | GE Healthcare, Munich, Germany | NA9310 | Western blot | 1:10,000 |
| ECL™-HRP-linked donkey anti-rabbit | GE Healthcare, Munich, Germany | NA9340 | Western blot | 1:10,000 |

With ECL-HRP = enhanced chemiluminescence horse raddish peroxidase.

**6.9 Software**

| Program | Application | Provider |
|---------|-------------|----------|
| Endnote X3 | Reference management | Adept Scientific GmbH, Frankfurt, Germany |
| Fiji | Image analysis and processing | *http://fiji.sc/* |
| ImageJ | Image analysis and processing | *http://imagej.nih.gov/* |
| Imspector | STED microscopy | MPI bpc, Göttingen, Germany http://www.imspector.de/ |
| MATLAB R2009b | Image analysis and processing | MathWorks, Natick, MA, USA |
| MATLAB R2011b | Image analysis and processing | MathWorks, Natick, MA, USA |
| Molecular Imaging Software | Western Blot Analysis (Image Station 4000R PRO) | Carestream Health, Rochester, NY, USA |
| Office2007 | Text and data processing | Microsoft Inc., Redmont, WA, USA |
| ZEN 2009 | Confocal microscopy (LSM710) | Carl Zeiss, Jena, Germany |

## Acknowledgments

**Jon Lederer** für das stetige Interesse an meiner Arbeit, die enge Zusammenarbeit mit unserer Arbeitsgruppe, erste Versuche, T-Tubuli mit dem STED Mikroskop zu sehen und die Beiträge, die zur erfolgreichen Publikation unserer Daten geführt haben.

**Die beste Arbeitsgruppe der Welt**. Ohne euch wären die letzten Jahre ganz schön trostlos gewesen. Ihr seid nicht nur Kollegen, sondern mit der Zeit auch Freunde geworden. Ein besseres Arbeitsumfeld hätte ich mir nicht wünschen können. Ich danke euch für eure Unterstützung sowohl beruflich als auch privat. Es ist schön, Mitglied unserer „Herde" zu sein!

Ganz besonders danke ich

**Julia Steinbrecher** für die Durchführung der Mausoperationen, der Echokardiographie, für die kritische Durchsicht aller Echokardiographie-Daten und für viele wertvolle Ratschläge zum Umgang mit Mäusen.

**Kirsten Koschel** für die Durchführung der Echokardiographie und unzählige Stunden der Auswertung.

**Brigitte Korff** für die Durchführung der Western Blots.

**Tobias Kohl** für die Unterstützung bei der Datenauswertung, für zahlreiche neue Ideen zur Datenanalyse und eine hervorragende Einarbeitung in den Umgang mit ImageJ.

**Patricia Mannheim** für ausgezeichnete technische Unterstützung, für das In-Schuss-halten unseres Labors, viele, viele Zellisolationen, Testfärbungen und die perfekte Dokumentation aller Experimente.

**Karen Presting** für die Unterstützung in allen organisatorischen Fragen, für das Abstimmen von Terminen und geballtes Wissen über die Abläufe im Klinikum. Danke, dass du immer da bist, wenn man dich braucht!

**Meine Eltern**. Ich bin so froh, dass es euch gibt! Danke für alles!

**Curriculum Vitae**

| **Persönliche Daten** |
|---|

Name                Eva Wagner
Geburtsdatum        24.07.1983
Geburtsort          Eschwege

| **Berufserfahrung** |
|---|

seit 2008           Wissenschaftliche Mitarbeiterin,
                    Abteilung für Kardiologie und Pneumologie,
                    Universitätsmedizin Göttingen

| **Universitäre Ausbildung** |
|---|

2009 – 2012         Doktorandin,
                    Abteilung für Kardiologie und Pneumologie,
                    Universitätsmedizin Göttingen

2008                Abschluss als Diplom-Biologin (Note *sehr gut*),
                    Georg-August-Universität, Göttingen

2007 – 2008         Diplomarbeit mit dem Titel „Identifizierung von Interaktionspartnern
                    glykolytischer Enzyme aus *Bacillus subtilis* mit Hilfe der SPINE-Technologie",
                    Institut für Mikrobiologie und Genetik,
                    Georg-August-Universität, Göttingen

2002 – 2008         Biologiestudium,
                    Georg-August-Universität, Göttingen

| **Schulische Ausbildung** |
|---|

2002                Abitur (Note 1,5),
                    Adam-von-Trott Schule, Sontra

2000 – 2002         Gymnasiale Oberstufe,
                    Adam-von-Trott Schule, Sontra

1993 – 2000         Förderstufe und gymnasialer Zweig,
                    Adam-von-Trott Schule, Sontra

1998 – 1993         Grundschule Sontra

---

**Publikationen**

---

**E. Wagner**, M.A. Lauterbach, T. Kohl, V. Westphal, G.S.B. Williams, J.H. Steinbrecher, J.-H. Streich, B. Korff, H.-T.M. Tuan, B. Hagen, S. Luther, G. Hasenfuss, U. Parlitz, M.S. Jafri, S.W. Hell, W.J. Lederer, S.E. Lehnart. *STED Live Cell Super-Resolution Imaging Shows Proliferative Remodeling of T-Tubule Membrane Structures After Myocardial Infarction.* Circ Res. 2012 Aug 3; 111(4): 402-14.

F.M. Commichau, F.M. Rothe, C. Herzberg, **E. Wagner**, D. Hellwig, M. Lehnik-Habrink, E. Hammer, U. Völker, J. Stülke. *Novel activities of glycolytic enzymes in Bacillus subtilis: interactions with essential proteins involved in mRNA processing*. Mol Cell Proteomics. 2009 Jun; 8(6):1350-60.

---

**Beiträge auf Fachtagungen**

---

76. Jahrestagung der Deutschen Gesellschaft für Kardiologie in Mannheim, 2010.
Abstract number 1063.
**E. Wagner**, M.A. Lauterbach, V. Westphal, B. Hagen, G. Hasenfuß, W.J. Lederer, S.W. Hell, S.E. Lehnart. *Live imaging of transverse tubules in ventricular myocytes by STED based super-resolution microscopy.*

Biophysical Journal (2010) Volume 98 (3), pp 5a.
**E. Wagner**, M.A. Lauterbach, V. Westphal, B. Hagen, W.J. Lederer, S.W. Hell, S.E. Lehnart. *STED-Based Super-Resolution Imaging of Transverse Tubules in Ventricular Myocytes.*

Heart Failure Association Winter Research Meeting in Les Diablerets, Switzerland, 2012.
Abstract number 30055.
**E. Wagner**, M.A. Lauterbach, T. Kohl, V. Westphal, S. Luther, G. Hasenfuß, U. Parlitz, S.W. Hell, W.J. Lederer, S.E. Lehnart. *STED live cell imaging shows early membrane remodeling of transverse tubules after myocardial infarction*.
→ Finalist für den "Young Investigators Poster Award"

Biophysical Journal (2012) Volume 102 (3), pp 223a – 224a.
**E. Wagner**, M.A. Lauterbach, T. Kohl, V. Westphal, G.S.B Williams, J.H. Steinbrecher, J.-H. Streich, H.-T.M. Tuan, B. Hagen, S. Luther, U. Parlitz, M.S. Jafri, S.W. Hell, W.J. Lederer, S.E. Lehnart. *Live Cell Super-Resolution Imaging of Transverse Membrane Tubules in Heart Failure*.

78. Jahrestagung der Deutschen Gesellschaft für Kardiologie in Mannheim, 2012.
Abstract number 701.
**E. Wagner**, M.A. Lauterbach, T. Kohl, V. Westphal, J.H. Steinbrecher, J.-H. Streich, U. Parlitz, S. Luther, G. Hasenfuß, S.W. Hell, W.J. Lederer, S.E. Lehnart. *STED super-resolution microscopy reveals progressive T-tubule remodeling during onset of heart failure*.
→ Prämiertes Poster im Bereich "Post-Infarkt Remodeling experimentell"